UNIVERSIDADE FEDERAL DE SÃO CARLOS
DEPARTAMENTO DE FÍSICA

Pablo Gabriel Santos Dias

Experimental evidences of modifications of light scattering in dense atomic clouds

São Carlos

2025

ABSTRACT

DIAS, P. **Experimental evidences of modifications of light scattering in dense atomic clouds**. 2025. 95 p. Thesis (Doctor) - DF-UFSCar, Universidade Federal de São Carlos, São Carlos, 2025.

In this thesis we proposed, build, e characterize an atomic physics experiment capable of producing dense atomic clouds and detecting light transmission down to the pW intensity level. The versatility of the system allows the production of atomic cloud with variable spatial density, up to 20 $\rho\lambda^3$ atoms. The system also have a repetition execution time of around 2-3 s, meaning a new measure can be done at this rate.

In the dense regime, we measure the light-transmission and observe a transition from single-atom effects to collective effects and multiple scattering. Transmission measurements resolved in polarization show deviations from the Beer-Lambert law at higher optical depths, indicating the presence of density effects and multiple scattering phenomena. Additionally, we explore the transmission for different saturation parameters.

Our study provides valuable insights into the complex interactions between light and dense atomic clouds, highlighting the importance of considering both individual and collective atomic behaviors. These findings have significant implications for future experiments and applications involving dense atomic ensembles, such as quantum optics and precision measurements.

Keywords: Atomic cloud. Dense phenomena. Multiple scattering.

CONTENTS

1 INTRODUCTION

Although the basic equations ruling the interaction between light and matter have been known for decades, their consequences are still object of intense study, due to the diversity of physical systems and the consequences of this interaction.

Some technological achievements of the last century helped to extend the realm of the physical systems accessible to the experimentalist, with strong consequences to this active field. Starting at the 1960s, the invention of the laser brought to the laboratory a source of spatially and spectrally coherent light not previously available. The light produced by laser sources is of easy mathematical description, especially when compared to the thermal light of the Sun and filament lamps or to the fluorescence of atomic gases. This property is due to its small entropy, or to its coherence: the high concentration of power in a single coherent mode of light. This powerful tool quickly opened unprecedented possibilities for matter manipulation, and for the investigation of the simplest and most fundamental consequences of the light-matter interaction.

Such low-entropy light does not remain fully coherent when it impinges on matter. The interaction between light and a material medium entails the elastic scattering of light to different directions, the inelastic scattering to different spectral modes, and also the eventual absorption of light by matter, diminishing the energy stored in the incoming light mode. The light scattering is responsible for the color, brightness and opacity of all objects around us. It can be deleterious when the objective is to gain information conveyed by light from a source that lays behind a scattering medium, such is often the case in astronomy (Kolokolova; Kimura, 2010) (astronomical objects can be found behind extended clouds of hydrogen or cosmic dust) or the biological imaging of tissues (Andersson-Engels *et al.*, 1997).

1.1 Wave scattering

Several models coexist for calculating the observables related to the light scattering and light transport by material media. They rely on different assumptions and different approximations, and their domain of validity can partially or fully superpose.

Maybe the most obvious model for the light scattering is one that treats it classically, i.e. as an electromagnetic wave, and the material medium as continuous and homogeneous. This model was first proposed in the context of light propagation in astrophysical media. The evolution of the light intensity $I(\mathbf{r}, t)$ in matter follows the basic equation (Rossum; Nieuwenhuizen, 1999)

$$\frac{\partial I(\mathbf{r},t)}{\partial t} = D\left(\boldsymbol{\nabla}^2 I(\mathbf{r},t) - \kappa^2 I(\mathbf{r},t)\right) + S(\mathbf{r},t)\ . \tag{1.1}$$

Here, the basic ingredients are the diffusion, described by the diffusion coefficient D; the absorption of light, of typical extinction length $L_{ex} = 1/\kappa$; and a source term $S(\mathbf{r},t)$. In this model, a lot of physics is hidden behind the diffusion constant D, related to the density of the medium, to the scattering cross-section of the individual scatterers, and the angular profile of the individual scattering. There must exist, then, a subjacent model to describe the interaction of light with individual scatterers, that will give a value to this diffusion constant. We conclude from this that the wave diffusion equation works like a framework, or like an emerging model, to appear in different possible descriptions of the light propagation.

Another important aspect of the wave diffusion equation is that it neglects the *granularity* of the material medium, in supposing an average, homogeneous medium. At best, such a model can work for obtaining the mean value of the observables, such as the scattered intensity in specific directions; but the actual values for a specific realization of the material medium can be far from this average value. A simple example of phenomenon not captured by this model is the light speckle caused by interference of the light scattered by a large amount of individual scatterers, as shown in figure 1. The intensity fluctuations on a speckle pattern are equal to the average value of the intensity, and this fluctuation is caused by constructive and destructive interference which is washed out on the averaging process that gives rise to the equation 1.1. In this way, the wave diffusion equation washes out coherence effects of the light scattering; this is why the intensity, and not the electric field, is the object of the model.

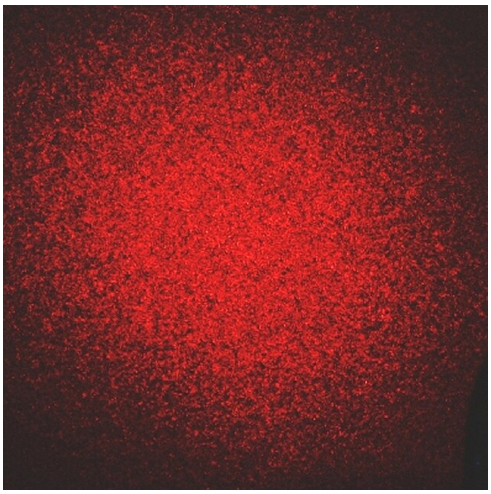

Figure 1 – Speckle formed by laser scattering on a white wall. Source: https://en.m.wikipedia.org/wiki/Speckle_(interference).

Other interference phenomena, such as the Anderson localization of waves (Segev;

Silberberg; Christodoulides, 2013), can be in certain limits described by an average diffusion equation of light. In this case, we must have a theoretical model that accounts for the collective modification of the diffusion constant due to interference of reciprocal scattering paths, as described by the Anderson localization. When averaging the emission profile over multiple realizations of an atomic medium, we can find an equation similar to equation 1.1, with a modified diffusion constant.

1.2 A random walk of photons

The diffusion model discussed above treats light as an electromagnetic wave. In a quantum treatment of light, the wave aspects of light are contained on the *modes* of electromagnetic radiation, while those modes are occupied by a discrete amount of quanta that can be thought of as particles of light. This so-called wave-particle duality manifests itself not only in the mathematical aspects of the theory but also in the implementation of numerical simulations of the light behavior and in the interpretation of its results.

The scattering of light by matter can, in many ways, resemble a random walk (RW) of photons within the material medium, just as the RW of diffusing particles in a solution (Gandjbakhche; Weiss, 1995). Indeed, one can model the diffusion from this point of view, by simulating individual photonic trajectories and then obtaining different observables, such as the angular scattered light distribution or the distribution of arrival time of photons, by averaging out the results of the individual trajectories.

For that, defining some quantities related to the scattering properties is important. One of those quantities is the scattering cross-section. For individual atoms, the cross-section is given by the simple expression

$$\sigma_0(\Delta) = \frac{3\lambda^2}{2\pi} f(\Delta), \tag{1.2}$$

where $\Delta = \omega - \omega_0$ is the photon detuning from the atomic resonance, λ is the wavelength, and the function $f(\Delta)$ describes the variation of atomic resonance with the photon wavelength.

If the scattering is isotropic, one can obtain from the scattering cross-section and the density ρ of the sample the mean free path for the photons inside the material sample, $l_{sc}(\mathbf{r}) = (\sigma_0 \rho(\mathbf{r}))^{-1}$. This parameter is used in a RW calculation to obtain the probability distribution for the path length of individual photons, and one can then sort out the trajectories and perform statistics on their distribution. This method can be understood as a Monte Carlo simulation of the wave diffusion equation, where one obtains its outcome after individual probabilistic realizations of the particle counterpart of the electromagnetic wave. What's interesting about the RW of photons is that one can assign a specific number of scattering events to each photonic path within the sample, and even obtain a probability

distribution of the number of scattering events that a photon undergoes, or the relative amount of single scattering and multiple scattering. This observable is not reachable through the wave diffusion equation.

Just as for the diffusion wave equation, any interference effect is washed out by this simulation, since no wave aspect is retained. It is thus clear by now that the speckle pattern will not be recovered here. But, what about the temporal aspects of the light scattering, such as the arrival time of photons?

Some temporal aspects of the light diffusion are captured by this model, such as the phenomenon of radiation trapping (Fioretti *et al.*, 1998). Radiation trapping describes the trapping of light due to its multiple scattering within the sample. The transit time of the light will strongly depend on the extension of the sample, more than linearly. The radiation trapping was first described by the Holstein equation (Holstein, 1947), but in the context of cold atoms, the width of the atomic resonances and the spectral purity of the incoming light causes divergences from this behavior (Weiss *et al.*, 2018). In particular, the distribution of path lengths for the photons satisfies statistical Lévy distributions long tails and ill-defined standard deviation, the so-called Lévy flights (Barthelemy; Bertolotti; Wiersma, 2008; Mercadier *et al.*, 2009).

On the other hand, some temporal aspects of the light scattering in dense atomic clouds are not captured by the aforementioned models; two examples are the subradiance (Pavolini *et al.*, 1985) and superradiance (Gross; Haroche, 1982) of light. They are not captured precisely because they depend on the coherent interference of the light scattered by all elements of the sample. In the temporal domain, the constructive (destructive) interference will give rise to an acceleration (deceleration) of the light emission rate, modifying the escape time of light.

1.3 Light emission by coupled dipoles

It becomes clear from the previous discussion that some aspects of the light-matter interaction need to restore the granularity of matter, and the coherence of light, to be fully described. This is achieved by the coupled dipoles (CD) simulation (Lehmberg, 1970; Courteille *et al.*, 2010), in which one calculates the total electric field at a certain direction as the sum of the electric field scattered by each one of the scatterers of the sample. Numerically costly, due to the necessity of computing the electric field of each scatterer, this calculation can reproduce several effects that rely on the interference of light, such as superradiance (Scully, 2009; Oliveira *et al.*, 2014; Araújo *et al.*, 2016), subradiance (Guerin; Araújo; Kaiser, 2016) and Anderson localization of light (Skipetrov; Sokolov, 2014; Skipetrov; Sokolov, 2018).

The coupled-dipole model establishes that each dipole from the sample is subject to

the incoming light, and the light is remitted by all other dipoles. In this way, single scattering and multiple scattering should be fully accounted for. Figure 2 shows a comparison of the angular profile of the steady-state light emission from an assembly of scatterers, computed from a RW simulation, and from a CD model simulation, extracted from (Chabé *et al.*, 2014), which shows that in most directions, both simulations agree. In the forward direction, there's a very intense peak, not captured by the RW: this corresponds to the forward transmitted light, which is the result of the incoming beam, plus the emission of light with opposite phase by each atom of the sample (giving rise to the light absorption). In the backward direction, the CD model shows a peak that has twice the intensity of the RW model. This is the phenomenon of coherent backscattering of light (Wolf; Maret, 1985; Labeyrie *et al.*, 1999). It relies on the constructive interference of reciprocal scattering paths. Thus, we understand that interference is the main ingredient missing in the RW model.

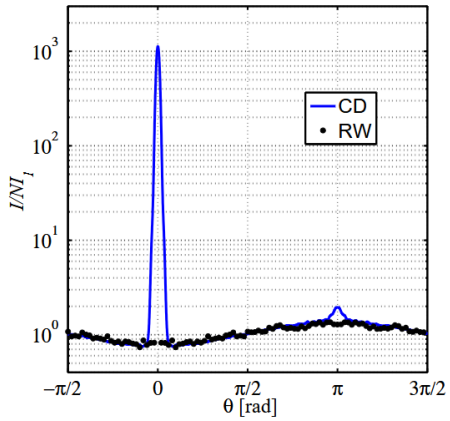

Figure 2 – Comparison between the angular distribution of the light scattered by an optical trap, computed by a random walk model (RW) or a coupled dipoles (CD) model. Extracted from (Chabé *et al.*, 2014).

From a temporal point of view, the interference gives rise to superradiance and subradiance, and the coupled dipoles model susccesfully described experimental observations of superradiance and subradiance in the past (Oliveira *et al.*, 2014; Araújo *et al.*, 2016; Guerin; Araújo; Kaiser, 2016).

1.4 Light scattering by dense samples

It seems from the previous discussion that interference effects are the only additional contribution from the coupled dipoles model. But there's at least another interesting aspect described by it: the changes in the light scattering due to the presence of near-field terms on the field scattered by the atoms. Indeed, in a RW model, there's a subjacent hypothesis that the photon is propagating from one atom to the other, as the far-field emission of an

electric dipole. But when the density of the cloud increases, the atoms can have several neighboring atoms at distances closer than the wavelength of the scattered light. In this regime, the neighbor atoms feel mostly the near-field, nonradiant terms of the electric field. The light diffusion is expected to change in this regime, with corrections to the cross-section (Javanainen *et al.*, 2017), to the diffusion constant, and to the subradiant emission of the cloud (Cipris *et al.*, 2021a).

Several recent experimental results on the light transport by dense atomic samples do not agree with results from the coupled dipole model, or other similar models (Jenkins *et al.*, 2016). The choice of the atomic species, possible effects of a stronger collective saturation of the transition (Mahmoodian *et al.*, 2018; Cipris *et al.*, 2021b), or even other effects, such as quantum molecular interaction potentials when atoms become too close, could be at play to explain the differences between the coupled dipole model and the experimental results. All in all, the light scattering by dense atomic samples is a many-body problem that is still far from being completely understood.

1.5 This work

In this thesis, I present the building of an experimental system to produce dense atomic clouds of cold Strontium atoms, for the study of the light transport properties when the density of the cloud induces strong collective modifications of the light diffusion caused by the near-field terms of the dipolar emission of the atoms. Although this thesis is mostly experimental, I dedicate a chapter to develop some theoretical concepts that are be useful in understanding the physics discussed here. Then, I present the experimental machine, that I (re)built almost entirely, which consumed, as usual, most of my time. I finish with experimental results on the resonant transmission of the atomic cloud, the main scientific result of this work.

2 THEORETICAL DESCRIPTION

2.1 Collective modifications of the light transmission by a cold atomic cloud

2.1.1 A single atom interacting with light

The theory of an atom interacting with an incoming coherent light field and with the vacuum modes of electromagnetic radiation is a seminal problem in quantum electrodynamics, extensively treated in several textbooks (Grynberg; Aspect; Fabre, 2010). We will here present some important results and consequences of this interaction, at the basis of the complex, many-body physics we want to approach.

We describe here the internal structure of an atom as composed of a fundamental and an excited level, separated in energy by $\hbar\omega_0$, where we call ω_0 the natural frequency of the transition: this simplified picture is justified in case of interaction with quasi-resonant light of angular frequency ω very close to ω_0, $|\omega - \omega_0| \ll \omega, \omega_0$, and far from resonance with any other atomic transition. We also suppose that this transition is electric dipole-allowed; this means that the electric dipole operator $\hat{\boldsymbol{d}}$ presents non-zero matrix elements between the fundamental and excited level.

Either the fundamental and the excited level of this electronic transition can be degenerate, as most atomic electronic levels are, due to the different sublevels of electronic levels with total angular momentum different than zero. The simplest possible case of a electric dipole-allowed transition is given by a $J = 0 \rightarrow J' = 1$ transition from a nondegenerate fundamental level $|g\rangle$ with zero angular momentum, to an excited level with total angular momentum $J = 1$, composed of three sublevels, with angular moment in the $+z$ direction equal to -1, 0 and 1, given respectively by $|e_{-1}\rangle$, $|e_0\rangle$ and $|e_1\rangle$. The atomic species chosen to perform the experiments described in this manuscript, ^{88}Sr, has its dipolar-allowed transitions from the fundamental level with this simplest structure. Another possible basis for the 3-dimensional space of the excited state is given by the upper states of the electric dipole operator in each cartesian direction of space, x, y and z, $|e_x\rangle$, $|e_y\rangle$ and $|e_z\rangle$, such as in this basis

$$\hat{\mathbf{d}} = \sum_{\alpha=x,y,z} \mathrm{d}\left(|e_\alpha\rangle\langle g| + |g\rangle\langle e_\alpha|\right) = \sum_{\alpha=x,y,z} \mathrm{d}\left(\hat{\sigma}_\alpha^{(+)} + \hat{\sigma}_\alpha^{(-)}\right) \ . \tag{2.1}$$

In the expression above, $\mathrm{d} \in \mathbb{R}$ is the matrix element of the electric dipole moment between the fundamental and excited states, and $\hat{\sigma}_\alpha^{(+)} = |e_\alpha\rangle\langle g|$ (resp. $\hat{\sigma}_\alpha^{(-)} = |g\rangle\langle e_\alpha|$) is the raising (resp. lowering) operator of the dipolar transition in direction α. When coherent, classical light of electric field $\mathbf{E}_L(\mathbf{r}, t)$ impinges on the atom, it couples to its internal structure via the dipolar Hamiltonian

$$\hat{H}_{\mathrm{d},1} = -\hat{\mathbf{d}} \cdot \mathbf{E}_L(\mathbf{r}, t) \ , \tag{2.2}$$

where we suppose that the position of the atomic center of mass $\mathbf{r}$ is treated classically. We suppose that the incoming laser field is monochromatic of frequency ω_L, i.e. $\mathbf{E}_L(\mathbf{r}, t) = \mathrm{Re}\left[\mathbf{E}_0(\mathbf{r})\, \mathrm{e}^{-i\omega_L t}\right]$. The expression above shows that the light polarization (the direction of $\mathbf{E}_L$) determines which excited sublevel the fundamental level will be coupled to. The Hamiltonian for the free atom is given by

$$\hat{H}_a = \sum_{\alpha=x,y,z} \hbar\omega_0 \, |e_\alpha\rangle\langle e_\alpha| \ . \tag{2.3}$$

For a complete model, we must also describe the coupling of the atom to the vacuum modes of the electromagnetic radiation. This coupling is a source of dissipation, since it allows for the atomic excitation to be lost as a photon to one of the infinite vacuum modes, that in turn leaves the region where it interacts with the atom. The Hamiltonian term to describe this coupling is given by

$$\hat{H}_{\mathrm{d},1,EM} = -\hat{\mathbf{d}} \cdot \hat{\mathbf{E}}_{EM}(\mathbf{r}, t) \ , \tag{2.4}$$

with

$$\hat{\mathbf{E}}_{EM}(\mathbf{r}, t) = \mathcal{E}_{\mathbf{k}} \sum_{\mathbf{k},\boldsymbol{\epsilon}} \left[\mathrm{e}^{i(\mathbf{k}\cdot\mathbf{r}-\omega t)} \, \hat{a}_{\mathbf{k},\boldsymbol{\epsilon}} \, \boldsymbol{\epsilon} + \mathrm{e}^{-i(\mathbf{k}\cdot\mathbf{r}-\omega t)} \, \hat{a}^\dagger_{\mathbf{k},\boldsymbol{\epsilon}} \, \boldsymbol{\epsilon}^* \right] \tag{2.5}$$

the electric field operator of the quantized modes of the radiation, summed over all modes determined by the wavevector $\mathbf{k}$ and polarization direction $\boldsymbol{\epsilon}$; $\omega = |\mathbf{k}|\, c$ is the frequency of the mode, and $\hat{a}_{\mathbf{k},\boldsymbol{\epsilon}}$ (resp. $\hat{a}^\dagger_{\mathbf{k},\boldsymbol{\epsilon}}$) is the annihilation (resp. creation) operator for a photon at the mode $(\mathbf{k}, \boldsymbol{\epsilon})$. The quantity $\mathcal{E}_{\mathbf{k}} = \sqrt{\frac{\hbar\omega_k}{2\varepsilon_0 V}}$ is the typical electric field of a single photon in a quantization volume V. We must also include in the total Hamiltonian the free evolution of the modes of electromagnetic radiation,

$$\hat{H}_{EM} = \sum_{\mathbf{k},\boldsymbol{\epsilon}} \hbar\omega \left[\hat{a}^\dagger_{\mathbf{k},\boldsymbol{\epsilon}} \, \hat{a}_{\mathbf{k},\boldsymbol{\epsilon}} + \frac{1}{2} \right] \ , \tag{2.6}$$

such as the total Hamiltonian for the single-atom $\hat{H}_1$ is given by $\hat{H}_1 = \hat{H}_a + \hat{H}_{EM} + \hat{H}_{\mathrm{d},1} + \hat{H}_{\mathrm{d},1,EM}$. From the Hamiltonian above, we can obtain the equations of motion for the total state of the system, considered to be the state of the atom plus the state of the quantized modes of radiation. Now, for an atom in free space, the photons lost to the vacuum of the electromagnetic field do not come back, and the vacuum states can be considered as a thermal bath (of zero temperature in the optical domain) with no memory (what is known in the literature as the Markov approximation (Lehmberg, 1970)) that induces dissipation

and entropy to the atomic state. The atomic state is described by the coherence operators $\hat{\sigma}_\alpha^{(\pm)}$ and their products, such as the atomic population $\hat{\sigma}_\alpha^{(+)}\hat{\sigma}_\alpha^{(-)}$ in each excited state $|e,\alpha\rangle$. In the case $|\Delta| \ll \omega_0, \omega_L$, with $\Delta = \omega_L - \omega_0$ the light detuning with respect to the atomic natural frequency ω_0, we place ourselves in the rotating frame with the light frequency ω_L, defining new coherence operators $\hat{\beta}_\alpha^{(\pm)} = \mathrm{e}^{\mp i\omega_L t}\,\hat{\sigma}_\alpha^{(\pm)}$. Those operators will evolve much slower than the fast evolution given by ω_0, ω_L. Within the Markov approximation, the effective non-Hermitian Hamiltonian that govern their evolution is given by (Courteille *et al.*, 2010)

$$\hat{H}_{1,\text{eff}} = -\hbar\left(\Delta + i\frac{\Gamma}{2}\right)\sum_{\alpha=x,y,z}\hat{\beta}_\alpha^{(+)}\hat{\beta}_\alpha^{(-)} + \frac{\hbar}{2}\sum_{\alpha=x,y,z}\left(\Omega_\alpha\hat{\beta}_\alpha^{(+)} + \Omega_\alpha^*\hat{\beta}_\alpha^{(-)}\right) . \tag{2.7}$$

To obtain the Hamiltonian of Eq. (2.7), we performed also the rotating wave approximation (Courteille *et al.*, 2010), which consists in eliminating nonresonant terms that evolves with frequency $\omega_0 + \omega_L$. The coupling to the incoming light field in each direction of space is determined by the Rabi frequencies $\Omega_\alpha = \mathrm{d}\left(\mathbf{E}_0(\mathbf{r})\right)_\alpha/\hbar$, where $\left(\mathbf{E}_0(\mathbf{r})\right)_\alpha$ is the component of the electric field in direction α. The non-Hermitian term of the Hamiltonian above is proportional to the free-space decay rate Γ of the atomic population,

$$\Gamma = \frac{\mathrm{d}^2\omega_0^3}{3\pi\varepsilon_0\hbar c^3} . \tag{2.8}$$

This non-Hermitian Hamiltonian governs the evolution of the atomic density matrix. Calling x the incoming light electric field direction and $\Omega_x \equiv \Omega$ the only non-zero Rabi frequency, we only care about the excitation of the level $|e,x\rangle \equiv |e\rangle$ and the coherences $\hat{\beta}_x^{(\pm)} \equiv \hat{\beta}^{(\pm)}$, such as the relevant density matrix is given by

$$\hat{\rho} = \begin{bmatrix}\rho_{gg} & \rho_{ge}\\ \rho_{eg} & \rho_{ee}\end{bmatrix} = \begin{bmatrix}\left\langle\hat{\beta}^{(-)}\hat{\beta}^{(+)}\right\rangle & \left\langle\hat{\beta}^{(-)}\right\rangle\\ \left\langle\hat{\beta}^{(+)}\right\rangle & \left\langle\hat{\beta}^{(+)}\hat{\beta}^{(-)}\right\rangle\end{bmatrix} . \tag{2.9}$$

We care about the temporal evolution of the coherence ρ_{ge} and the population ρ_{ee}; the two other matrix elements are a function of those via the properties of the density matrix, $\rho_{eg} = \rho_{ge}^*$ and $\rho_{gg} + \rho_{ee} = 1$. The evolution of the density matrix subjected to the non-Hermitian Hamiltonian is governed by the equation (Ohlsson; Zhou, 2021)

$$\frac{\mathrm{d}\hat{\rho}}{\mathrm{d}t} = \frac{-i}{\hbar}\left[\hat{H}_{1,\text{eff}}\,\hat{\rho} - \hat{\rho}\,\hat{H}_{1,\text{eff}}^\dagger\right] , \tag{2.10}$$

and we obtain for the coherence and the population the following equations of evolution, called the Bloch equations:

$$\frac{\partial \rho_{\mathrm{ge}}}{\partial t} = \frac{\Omega}{2i}\left(\rho_{\mathrm{ee}} - \rho_{\mathrm{gg}}\right) + \left(i\Delta - \frac{\Gamma}{2}\right)\rho_{\mathrm{ge}} \tag{2.11a}$$

$$\frac{\partial \rho_{\mathrm{ee}}}{\partial t} = \frac{\Omega}{2i}\left(\rho_{\mathrm{ge}} - \rho_{\mathrm{eg}}\right) - \Gamma\,\rho_{\mathrm{ee}} \tag{2.11b}$$

The steady-state solution of those equations are found by setting the temporal derivatives to zero, yielding

$$\rho_{\mathrm{ee,st}} = \frac{\Omega^2}{\Gamma^2 + 2\Omega^2 + 4\Delta^2} = \frac{1}{2}\,\frac{s}{1+s}\ , \tag{2.12}$$

$$\rho_{\mathrm{ge,st}} = \frac{\Omega}{2\Delta - i\Gamma}\,\frac{\Gamma^2}{\Gamma^2 + 2\Omega^2} = \frac{\Omega}{2\Delta - i\Gamma}\,\frac{1}{1+s}\ . \tag{2.13}$$

In the expressions above, s is the saturation parameter, given by

$$s = \frac{2\Omega^2}{\Gamma^2 + 4\Delta^2}\ . \tag{2.14}$$

The saturation parameter at resonance, s_0, is given by

$$s_0 = \frac{2\Omega^2}{\Gamma^2}\ , \tag{2.15}$$

such as

$$s = \frac{s_0}{1 + 4\frac{\Delta^2}{\Gamma^2}}\ . \tag{2.16}$$

In view of the relation between the electric field of light $\mathbf{E}_0(\mathbf{r})$ and its intensity $\mathrm{I}(\mathbf{r})$, given by the modulus of the Poynting vector

$$\mathrm{I}(\mathbf{r}) = \frac{\left|\mathbf{E}_0(\mathbf{r})\right|^2}{2\mu_0 c}\ , \tag{2.17}$$

we can rewrite s_0 as

$$s_0 = \frac{\mathrm{I}}{\mathrm{I}_{\mathrm{sat}}}\ , \tag{2.18}$$

with the saturation intensity $\mathrm{I}_{\mathrm{sat}}$ given by

$$\mathrm{I}_{\mathrm{sat}} = \frac{\hbar^2\Gamma^2}{4\mu_0\, c\, d^2} = \frac{\hbar\Gamma{\omega_0}^3}{12\pi c^2}\ . \tag{2.19}$$

2.1.1.1 Light scattering by a single atom

Since the excited population of the atom is different than zero, the atom subjected to the incoming intensity will continuously scatter light in random directions, removing energy from the incoming beam. The positive frequencies' component of the electric field operator of the light scattered by the atom, $\hat{\mathbf{E}}_1^{(+)}$, is a function of the coherences of the atom (Cohen-Tannoudji; Dupont-Roc; Grynberg, 1998; Jackson, 2021):

$$\hat{\mathbf{E}}_1^{(+)} = \frac{\mathrm{d}\, k_L^3}{4\pi\epsilon_0}\, \mathrm{e}^{ik_L r} \left[\frac{\left(\mathbf{e}_r \times \hat{\boldsymbol{\sigma}}^{(-)}\right) \times \mathbf{e}_r}{k_L r} + \left[3\left(\mathbf{e}_r \cdot \hat{\boldsymbol{\sigma}}^{(-)}\right)\mathbf{e}_r - \hat{\boldsymbol{\sigma}}^{(-)}\right] \left(\frac{1}{(k_L r)^3} - \frac{i}{(k_L r)^2} \right) \right] , \tag{2.20}$$

such as the Hermitian electric field operator is $\hat{\mathbf{E}}_1 = \hat{\mathbf{E}}_1^{(+)} + \left(\hat{\mathbf{E}}_1^{(+)}\right)^\dagger$. We have used in the expression above the unitary vector $\mathbf{e}_r = \mathbf{r}/r$ at the direction of the position $\mathbf{r} = (x, y, z)$ with respect to the atom center of mass, and $r = |\mathbf{r}|$; as well as the wavenumber of the incoming light, $k_L = \omega_L/c$. We have also used the vectorial notation

$$\hat{\boldsymbol{\sigma}}^{(-)} = (\hat{\sigma}_x^{(-)}, \hat{\sigma}_y^{(-)}, \hat{\sigma}_z^{(-)}) \ . \tag{2.21}$$

We can write explicity the temporal dependence of the atomic coherences via

$$\hat{\boldsymbol{\sigma}}^{(-)} = \hat{\boldsymbol{\beta}}^{(-)}\, \mathrm{e}^{-i\omega_L t} \tag{2.22}$$

with the vectorial notation $\hat{\boldsymbol{\beta}}^{(-)} = (\hat{\beta}_x^{(-)}, \hat{\beta}_y^{(-)}, \hat{\beta}_z^{(-)})$. The electric field expression contains 2 terms: The first one, proportional to $1/(k_L r)$, is the term that survives in the far field and gives rise to a spherical wave emanating from the atomic position. The other terms, proportional to $1/(k_L r)^2$ and $1/(k_L r)^3$, are near-field terms that produce no light intensity in the far field. We will see, nevertheless, that those terms are important for the light propagation within dense atomic samples, as far as other atoms are close enough (at distances $r \lesssim 1/k_L$) such as to feel the near-field terms of the light emitted by other atoms.

In the steady state, and supposing the incoming light field in the x direction (such as to use the results for the steady-state atomic coherences deduced before), the mean value of the electric field is calculated via

$$\left\langle \hat{\mathbf{E}}_1 \right\rangle = \frac{\mathrm{d}\, \rho_{\mathrm{ge,st}}\, k_L^3}{4\pi\epsilon_0}\, \mathrm{e}^{ik_L r - i\omega_L t} \left[\frac{(\mathbf{e}_r \times \mathbf{e}_x) \times \mathbf{e}_r}{k_L r} + \left[3\left(\mathbf{e}_r \cdot \mathbf{e}_x\right)\mathbf{e}_r - \mathbf{e}_x\right] \left(\frac{1}{(k_L r)^3} - \frac{i}{(k_L r)^2} \right) \right] + \text{c.c.} \tag{2.23}$$

We see from the expression above that the average value of the scattered electric field is equal to the electric field emitted by a classical dipole of amplitude $\mathbf{d} = \mathrm{d}\rho_{\mathrm{ge,st}} \mathrm{e}^{-i\omega_L t} \mathbf{e}_x +$

c.c.. But the fluctuations of the electric field can be important in certain regimes, determined by the saturation parameter of the excitation. In the limit $s \ll 1$, the light-matter interaction is said to occur in the linear regime. In this regime, the excited population depends linearly on the incoming intensity, $\rho_{\mathrm{ee,st}} \simeq \frac{s}{2} = \frac{1}{2}\frac{I}{I_{\mathrm{sat}}}$, and the quantum fluctuations of the atomic coherence operator are small, such as we can write $\hat{\boldsymbol{\sigma}}^{(-)} \simeq \left\langle \hat{\boldsymbol{\sigma}}^{(-)} \right\rangle$. In this case, the light scattering is said to be elastic, because the spectral properties of the scattered light are equal to the properties of the classical incoming light field. We can write in this case $\hat{\mathbf{E}}_1 \simeq \left\langle \hat{\mathbf{E}}_1 \right\rangle$.

The positive frequencies' component of the electric field in the far field (the radiating part of the electric field) is given by

$$\hat{\mathbf{E}}^{(+)}_{1,\mathrm{ff}} = \frac{\mathrm{d}\, k_L^2}{4\pi\epsilon_0}\, \mathrm{e}^{ik_L r - i\omega_L t} \left[\frac{\left(\mathbf{e}_r \times \hat{\boldsymbol{\beta}}^{(-)} \right) \times \mathbf{e}_r}{r} \right] , \tag{2.24}$$

and the average intensity emitted by this dipole, calculated from the electric field and the Poynting vector, is calculated from the operator above as (Cohen-Tannoudji; Dupont-Roc; Grynberg, 1998)

$$\mathrm{I}_1(\mathbf{r}) = \frac{2\left\langle \left(\hat{\mathbf{E}}^{(+)}_{1,\mathrm{ff}} \right)^{\dagger} \cdot \hat{\mathbf{E}}^{(+)}_{1,\mathrm{ff}} \right\rangle}{\mu_0 c} = \frac{\mathrm{d}^2 \left\langle \hat{\boldsymbol{\beta}}^{(+)} \cdot \hat{\boldsymbol{\beta}}^{(-)} \right\rangle c\, k_L^4}{8\pi^2\epsilon_0 r^2} \sin^2(\theta_p) = \frac{\mathrm{d}^2\, \rho_{\mathrm{ee,st}}\, c\, k_L^4}{8\pi^2\epsilon_0 r^2} \sin^2(\theta_p) \ . \tag{2.25}$$

The angle θ_p is determined by the direction of the atomic dipole with respect to the observation direction: $\cos(\theta_p) = \mathbf{e}_x \cdot \mathbf{e}_r$. The total power emitted by the atom, i.e. the intensity integrated over a sphere centered at the atom position, is

$$\mathrm{P}_1 = \frac{\mathrm{d}^2\, \rho_{\mathrm{ee,st}}\, c\, k_L^4}{3\pi\epsilon_0} = \rho_{\mathrm{ee,st}} \Gamma \hbar \omega_L \ , \tag{2.26}$$

where we have used the Eq. (2.8) and $\omega_L \simeq \omega_0$ for near-resonant light. The interpretation of the equation above is clear: The total power scattered by the atom is equal to the photon scattering rate, $\rho_{\mathrm{ee,st}}\Gamma$ (the excited state population times the natural decay rate), times the energy of one photon, $\hbar\omega_L$. By using also Eqs. (2.12) and (2.19), and $\omega_L \simeq \omega_0$, we obtain the relation

$$\mathrm{P}_1 = \frac{1}{2}\frac{s}{1+s}\Gamma\hbar\omega_0 = \frac{3\lambda_0^2}{2\pi}\frac{1}{1+s_0+4\frac{\Delta^2}{\Gamma^2}} I \ . \tag{2.27}$$

The proportionality factor between P_1 and the incoming intensity I is the scattering cross-section of the atom,

$$\sigma(\Delta, s_0) = \frac{3\lambda_0^2}{2\pi} \frac{1}{1 + s_0 + 4\frac{\Delta^2}{\Gamma^2}} = \frac{\sigma_0}{1 + s_0 + 4\frac{\Delta^2}{\Gamma^2}} \tag{2.28}$$

with

$$\sigma_0 = \sigma(\Delta = 0, s_0 \to 0) = \frac{3\lambda_0^2}{2\pi} \tag{2.29}$$

the resonant scattering cross-section in the linear regime (i.e., for $s_0 \ll 1$). We can also write the cross-section in the linear regime,

$$\sigma_l(\Delta) = \sigma(\Delta, s_0 \to 0) = \frac{\sigma_0}{1 + 4\frac{\Delta^2}{\Gamma^2}} \ . \tag{2.30}$$

The Eq. (2.23), and the fact that $\hat{\mathbf{E}}_1 \simeq \left\langle \hat{\mathbf{E}}_1 \right\rangle$ for low incoming intensity ($s_0 \ll 1$) shows that in this regime, the spectrum of the emitted light is equal to the spectrum of the incoming light. This is a manifestation of the energy conservation of the photons in the model developed here, that does not include the kinetic energy of the atomic center of mass. On the other hand, if we consider the condition for energy conservation including the kinetic energy of the atomic center of mass, this will not be the case. It is easier to calculate this effect by considering the event of one photon absorption, followed by one photon emission. Let's suppose that the incoming light has wavevector in direction z, determined by the unitary vector $\mathbf{e}_z$, and let's calculate the modification of the light frequency emitted in the direction determined by $\mathbf{e}_r$. For an atom with inicial velocity $\mathbf{v}$, the new velocity after the absorption of the incoming photon with momentum $\hbar k_L \mathbf{e}_z$ and emission of one photon with momentum $\hbar k_L \mathbf{e}_r$ is $\mathbf{v}' = \mathbf{v} + \hbar k_L/m(\mathbf{e}_z - \mathbf{e}_r)$, by momentum conservation, with m the atomic mass. Then, the difference in kinetic energy will be

$$\Delta K = \frac{m}{2} v'^2 - \frac{m}{2} v^2 = \hbar k_L \mathbf{v} \cdot (\mathbf{e}_z - \mathbf{e}_r) + \frac{\hbar^2 k_L^2}{2m} \left| \mathbf{e}_z - \mathbf{e}_r \right|^2 \ . \tag{2.31}$$

By energy conservation, this kinetic energy is removed from the photon scattered, such as the new frequency of the emitted light, ω_L' will be given by

$$\omega_L' = \omega_L - \frac{\Delta K}{\hbar} = \omega_L - k_L \mathbf{v} \cdot (\mathbf{e}_z - \mathbf{e}_r) - \frac{\hbar k_L^2}{2m} \left| \mathbf{e}_z - \mathbf{e}_r \right|^2 \ . \tag{2.32}$$

This effect is related to the Doppler shift of the transition, but also includes a term proportional to the recoil energy $\frac{\hbar^2 k_L^2}{2m}$. The recoil energy is equal to the kinetic energy that an atom initially at rest acquires upon absorption of one photon of wavelength k_L.

Before passing to the treatment of several atoms interacting collectively with light, we would want to say a few words about the opposite limit, the saturated regime $s \gtrsim 1$. In this regime, the description of the light scattering becomes quite different. First of all, the

excited atomic population does not vary linearly anymore with the saturation parameter s, but saturates in the regime $s \gg 1$ to the value $\rho_{\mathrm{ee,st}} = 1/2$. Moreover, due to the depletion of the fundamental level, the atomic excitation in different directions of space, such as the excitation by different sources of light, do not add independently, but the saturation created by one light beam influences the other transitions with electric field in perpendicular directions, making it very difficult to describe the light diffusion in material samples in this regime. Last but not least, the quantum fluctuations of the atomic coherence, $\delta\hat{\boldsymbol{\sigma}}^{(-)} = \hat{\boldsymbol{\sigma}}^{(-)} - \left\langle \hat{\boldsymbol{\sigma}}^{(-)} \right\rangle$, become important, and the spectrum of the light scattered is broadened with respect to the spectrum of the incoming light. This broadened spectrum, called the Mollow spectrum (Mollow, 1969; Dias, 2020), further complicates the analysis of the light transport within assemblies of atoms, because the different spectral components of the scattered light interacts differently with the other atoms of the sample. The light scattered present now two components (Cohen-Tannoudji; Dupont-Roc; Grynberg, 1998): the elastic one, as described before, of intensity proportional to $\left\langle \hat{\boldsymbol{\sigma}}^{(+)} \right\rangle \left\langle \hat{\boldsymbol{\sigma}}^{(-)} \right\rangle = s/2(1+s)^2$; and the inelastic one, of intensity proportional to $\left\langle \delta\hat{\boldsymbol{\sigma}}^{(+)}\, \delta\hat{\boldsymbol{\sigma}}^{(-)} \right\rangle = s^2/2(1+s)^2$ and broadened spectrum (of typical width $\sqrt{\Omega^2 + \Gamma^2/16}$). The ratio between the inelastic and elastic components of the scattered light is simply s, which shows that for saturated light, the inelastic component becomes important.

Because of all those complications, we pay attention to keeping the saturation parameter much smaller than one in our experiments, and the theory for the light scattering by ensembles of atoms, to be developed on what follows, will be done in this linear regime of $s \ll 1$.

2.2 An assembly of atoms interacting with low intensity light

We now turn to the problem of N atoms interacting with an incoming laser field. At first, we will discuss a very simple result for the transmission of light by the atomic cloud, the Beer-Lambert law for light extinction. But this mean-field approach does not capture the many-body modifications of the light transport within the material sample, due to the interaction of each atom with the light scattered by the other constituents. To tackle this complexity, we then present two different approaches, the coupled dipoles model and the random walk model, discuss their applicability and limitations.

2.2.1 The Beer-Lambert law for the light transmission by an atomic cloud

A very simple model exists for the light transmission by a material sample, called the Beer-Lambert law. It builds up on the behavior of single constituents of matter interacting with light, fully described by their scattering cross-section. Let's consider that the incoming laser field propagates in the z direction. For a weak atomic excitation (i.e. in the linear regime), neglecting the effect of the light scattered by one atom on the others,

the light intensity at position $(x, y, z + \mathrm{d}z)$ is a function of the light intensity at (x, y, z), for small $\mathrm{d}z$, as

$$I(x, y, z + \mathrm{d}z) = I(x, y, z) - \sigma_l(\Delta)\rho_\mathrm{a}(x, y, z)I(x, y, z) \ , \tag{2.33}$$

where ρ_a is the atomic density. Integrating the equation above from $z \to -\infty$, where the light intensity is equal to $I_0(x, y)$, we obtain

$$I(x, y, z) = I_0(x, y)\,\mathrm{e}^{-\sigma_l(\Delta)\int_{-\infty}^{z}\mathrm{d}z'\rho_\mathrm{a}(x,y,z')} \ . \tag{2.34}$$

The light intensity passing through by the atomic sample of finite extension is given by

$$I(x, y, z \to \infty) = I_0(x, y)\,\mathrm{e}^{-b(\Delta)} \tag{2.35}$$

with

$$b(\Delta) = \sigma_l(\Delta)\int_{-\infty}^{\infty}\mathrm{d}z'\rho_\mathrm{a}(x, y, z') \tag{2.36}$$

the *optical depth* of the sample (for the propagation in the z direction). We also define the resonant optical depth as $b_0 = b(\Delta = 0)$, such as, due to the definition of σ_l,

$$b(\Delta) = \frac{b_0}{1 + \dfrac{\Delta^2}{\Gamma^2}} \ . \tag{2.37}$$

This result does not take into account the effect of the scattered light by the all other atoms on the response of one atom. For that reason, it will fail for dense atomic clouds. We will present a refined model that can take into account the effect of the other dipoles in the interaction of one dipole with light.

2.2.2 The coupled dipoles model

We will develop here an approach very similar to what was developed in the single atom case. Each atom j has a ground level $|g_j\rangle$ and three excited levels $|e_{j,x}\rangle$, $|e_{j,y}\rangle$ and $|e_{j,z}\rangle$, such that the vectorial electric dipole operator of atom j is given by $\hat{\mathbf{d}}_j = \mathrm{d}\left(\hat{\boldsymbol{\sigma}}_j^{(-)} + \hat{\boldsymbol{\sigma}}_j^{(+)}\right)$, with the vectorial coherence operator of atom j, $\hat{\boldsymbol{\sigma}}_j^{(-)} = (\hat{\sigma}_{j,x}^{(-)}, \hat{\sigma}_{j,y}^{(-)}, \hat{\sigma}_{j,z}^{(-)})$; the coherence in each direction $\hat{\sigma}_{j,x}^{(-)} = |g_j\rangle\langle e_{j,x}|$, $\alpha = x, y, z$, and $\hat{\boldsymbol{\sigma}}_j^{(+)} = \left(\hat{\boldsymbol{\sigma}}_j^{(-)}\right)^\dagger$. The coupling to the incoming electric field is described by the Hamiltonian

$$\hat{H}_{\rm d} = -\sum_{j=1..N} \hat{\mathbf{d}}_j \cdot \mathbf{E}_L(\mathbf{r}_j, t) \ , \tag{2.38}$$

where $\mathbf{r}_j$ is the position of the center of mass of atom j. In the same way, the coupling to the vacuum modes of radiation is described by the Hamiltonian

$$\hat{H}_{{\rm d},EM} = -\sum_{j=1..N} \hat{\mathbf{d}}_j \cdot \hat{\mathbf{E}}_{EM}(\mathbf{r}_j, t) \ . \tag{2.39}$$

The total Hamiltonian for N atoms interacting with light is then given by $\hat{H} = \hat{H}_a + \hat{H}_{EM} + \hat{H}_{\rm d} + \hat{H}_{{\rm d},EM}$. Then, as we did before, we can apply the Born-Markov approximation and the rotating wave approximation to this problem (Lehmberg, 1970), which gives the following non-Hermitian Hamiltonian for N atoms interacting with light:

$$\begin{aligned}\hat{H}_{\rm eff} \ = \ -\hbar\,\Delta \sum_{\substack{j=1\ldots N\\ \alpha=x,y,z}} \hat{\beta}^{(+)}_{j,\alpha}\,\hat{\beta}^{(-)}_{j,\alpha} + \sum_{\substack{j=1\ldots N\\ \alpha=x,y,z}} \frac{\hbar}{2}\left(\Omega_{j,\alpha}\,\hat{\beta}^{(+)}_{j,\alpha} + \Omega^*_{j,\alpha}\,\hat{\beta}^{(-)}_{j,\alpha}\right) \\ - \ i\,\frac{\hbar\Gamma}{2} \sum_{\substack{j,m=1\ldots N\\ \alpha,\gamma=x,y,z}} V_{j,\alpha,m,\gamma}\,\hat{\beta}^{(+)}_{j,\alpha}\,\hat{\beta}^{(-)}_{m,\gamma} \ .\end{aligned} \tag{2.40}$$

In the equations above we have used the Rabi frequency seen by the α component of the dipole moment of atom j, $\Omega_{j,\alpha} = {\rm d}\,\left(\mathbf{E}_0(\mathbf{r}_j)\right)_\alpha/\hbar$. The last term of the Hamiltonian is the non-Hermitian term, that arises from the Born-Markov treatment of the coupling to the vacuum modes of radiation. This term shows all-to-all coupling of the atomic coherences, via jump operators $\hat{\beta}^{(+)}_{j,\alpha}\hat{\beta}^{(-)}_{m,\gamma}$ for the coherence of atom m in direction γ to the atom j in direction α. This coupling is mediated by the vacuum modes of the radiation, via emission and reabsorption of photons, and the matrix elements $V_{j,\alpha,m,\gamma}$ are given by

$$\begin{aligned}V_{j,\alpha,m,\gamma} = \frac{3}{2}\,\frac{{\rm e}^{ik_L r_{jm}}}{ik_L r_{jm}}\Bigg[\mathbf{e}^*_\alpha.\mathbf{e}_\gamma - (\mathbf{e}_{jm}.\mathbf{e}^*_\alpha)\,(\mathbf{e}_{jm}.\mathbf{e}_\gamma) \\ + \left(\frac{i}{k_L r_{jm}} - \frac{1}{(k_L r_{jm})^2}\right)\left(\,\mathbf{e}^*_\alpha.\mathbf{e}_\gamma - 3\,(\mathbf{e}_{jm}.\mathbf{e}^*_\alpha)\,(\mathbf{e}_{jm}.\mathbf{e}_\gamma)\right)\Bigg] \ , \\ \text{for} \quad m \neq j \quad \text{and} \quad \alpha,\gamma \in \{x,y,z\} \ ;\end{aligned} \tag{2.41}$$

$$V_{j,\alpha,j,\gamma} = \delta_{\alpha,\gamma} \quad \text{for} \quad \alpha,\gamma \in \{x,y,z\} \ .$$

The unitary vectors $\mathbf{e}_\alpha$ point to the direction α; $\mathbf{r}_{jm} = \mathbf{r}_j - \mathbf{r}_m$ is the relative position of atom j with respect to atom m, of mutual distance $r_{jm} = |\mathbf{r}_{jm}|$; also, $\mathbf{e}_{jm} = \mathbf{r}_{jm}/r_{jm}$

in a unitary vector in the direction $\mathbf{r}_{jm}$. The diagonal terms of the matrix above, $V_{j,\alpha,j,\alpha}$, represent the natural decay of each individual atom, exactly as found in the single-atom model developed before. The non-diagonal terms of the matrix above are proportional to the interaction energy between two electric dipoles in classical electromagnetism, and represent the exchange of excitation among atoms due to the dipolar interaction mediated by the vacuum modes of the radiation.

In the Heisenberg picture, we can deduce the temporal derivative of the coherence operators:

$$\begin{aligned}\frac{\mathrm{d}\hat{\beta}_{j,\alpha}^{(-)}}{\mathrm{d}t} &= \frac{i}{\hbar}\left(\hat{H}_{\text{eff}}\,\hat{\beta}_{j,\alpha}^{(-)} - \hat{\beta}_{j,\alpha}^{(-)}\,\hat{H}_{\text{eff}}^{\dagger}\right) \\ &= \left[\hat{\beta}_{j,\alpha}^{(-)}, \hat{\beta}_{j,\alpha}^{(+)}\right]\left\{\left(i\Delta - \frac{\Gamma}{2}\right)\hat{\beta}_{j,\alpha}^{(-)} + i\frac{\Omega_{j,\alpha}}{2} - \frac{\Gamma}{2}\sum_{\substack{m\neq j \\ \gamma=x,y,z}} V_{j,\alpha,m,\gamma}\,\hat{\beta}_{m,\gamma}^{(-)}\right\} . \quad (2.42)\end{aligned}$$

The equation above is nonlinear, due to the presence of the commutator $\left[\hat{\beta}_{j,\alpha}^{(-)}\,,\,\hat{\beta}_{j,\alpha}^{(+)}\right] = |g_j\rangle\langle g_j| - |e_{j,\alpha}\rangle\langle e_{j,\alpha}|$, creating a dependence of the temporal evolution of $\hat{\beta}_{j,\alpha}^{(-)}$ on products of operators. The exact dynamics given by the equations of motion above is very difficult to calculate in general. If, on the other hand, we suppose that the excited population of each atom remains very small, then

$$\left[\hat{\beta}_{j,\alpha}^{(-)}\,,\,\hat{\beta}_{j,\alpha}^{(+)}\right] = |g_j\rangle\langle g_j| - |e_{j,\alpha}\rangle\langle e_{j,\alpha}| \simeq 1 \,, \quad (2.43)$$

and in this case the evolution equation for $\hat{\sigma}_{j,\alpha}$ depends linearly on the other operators. For Eq. (2.43) to hold, we need in particular that the resonant saturation parameter of the incoming laser field remains much smaller than one, $s_{0,j} \ll 1$ for any atom j; but we remark also that due to the possible strong coupling between atoms, it is possible that $s_{0,j} \ll 1$ is not a sufficient condition for Eq. (2.43) to hold when the atoms become too close in the atomic cloud. We will nevertheless assume Eq. (2.43) for the remaining of this section, in order to deduce the Coupled Dipoles Model dynamical equations, that suppose a linear coupling between all coherences. In this linear regime, the quantum fluctuations of the atomic coherences can be neglected, such as $\hat{\beta}_{j,\alpha}^{(-)} \simeq \left\langle\hat{\beta}_{j,\alpha}^{(-)}\right\rangle$; we will keep the simplified notation $\beta_{j,\alpha} \equiv \left\langle\hat{\beta}_{j,\alpha}^{(-)}\right\rangle$ for the average value of the coherences. This means that in this limit, the atoms behave just as classical dipoles, of amplitude in each direction of space α

$$\mathrm{d}_{j,\alpha} = \mathrm{d}\left(\beta_{j,\alpha}\mathrm{e}^{-i\omega_L t} + \text{c.c.}\right) . \quad (2.44)$$

Taking the average of Eq. (2.42), and considering (2.43), we arrive to the evolution of the atomic coherences

$$\frac{\mathrm{d}\beta_{j,\alpha}}{\mathrm{d}t} = \left(i\Delta - \frac{\Gamma}{2}\right)\,\beta_{j,\alpha} + i\frac{\Omega_{j,\alpha}}{2} - \frac{\Gamma}{2}\sum_{\substack{m\neq j\\ \gamma=x,y,z}} V_{j,\alpha,m,\gamma}\,\beta_{m,\gamma}\ . \tag{2.45}$$

This linear set of first-order differential equations can also be rewritten in order to explicitly separate its homogeneous and inhomogeneous terms, as

$$\frac{\mathrm{d}\beta_{j,\alpha}}{\mathrm{d}t} \;=\; \sum_{\substack{m=1\ldots N\\ \gamma=x,y,z}} K_{j,\alpha,m,\gamma}\,\beta_{m,\gamma} \;+\; i\,\frac{\Omega_{j,\alpha}}{2}\ . \tag{2.46}$$

The matrix K, of dimension $3N \times 3N$ with matrix elements $K_{j,\alpha,m,\gamma}$, given by

$$K_{j,\alpha,m,\gamma} = -\frac{\Gamma}{2}V_{j,\alpha,m,\gamma} \;+\; i\,\Delta\,\delta_{j,m}\,\delta_{\alpha,\gamma} \tag{2.47}$$

determines the effective coupling between the atomic dipoles, mediated by the modes of the vacuum field.

In absence of laser excitation of the atoms, $\Omega_{j,\alpha} = 0$ for all j and α, and the set of differential equations, eq. (2.46) become homogeneous:

$$\frac{\mathrm{d}\beta_{j,\alpha}}{\mathrm{d}t} \;=\; \sum_{\substack{m=1\ldots N\\ \gamma=x,y,z}} K_{j,\alpha,m,\gamma}\,\beta_{m,\gamma}\ . \tag{2.48}$$

To obtain the behavior of the dipole amplitudes, we must solve this set of $3N$ first-order differential equations given at Eq. (2.48). This is done by the diagonalization of the matrix K. One must though be careful, since K is not a Hermitian matrix, and so we cannot apply all properties that Hermitian operators usually have. Although K is not Hermitian, it is a symmetric matrix, i.e., $K^T = K$, because $K_{j,\alpha,m,\gamma} = K_{m,\gamma,j,\alpha}$. For a symmetric matrix A of dimension M, one can still find a set of M numbers λ_n and vectors $\mathbf{v}_n$, for $n \in \{1, ..., M\}$, such that (Skipetrov; Sokolov, 2019)

$$A\,\mathbf{v}_n = \lambda_n\,\mathbf{v}_n \tag{2.49}$$

The vectors $\mathbf{v}_n$ are called the right-side eigenvectors of the matrix. Since the matrix is symmetric, it is easy to find the left-side eigenvectors of the matrix A, by taking the transpose of the equation above:

$$(A\,\mathbf{v}_n)^T = (\mathbf{v}_n)^T\,(A)^T = (\mathbf{v}_n)^T\,A = \lambda_n\,(\mathbf{v}_n)^T\ , \tag{2.50}$$

which shows that the left-side eigenvectors of the matrix are simply given by the transpose of the right-side eigenvectors, $(\mathbf{v}_n)^T$. Our matrix $K^{(v)}$ has a dimension $M = 3N$, and

it will have $3N$ eigenvalues, that we write as $\lambda_n = -\Gamma_n/2 + i\Delta_n$, with $n \in \{1, ..., 3N\}$, separating its real and imaginary parts, by analogy with the independent-atom picture: $\mathrm{Re}[\lambda_n] = -\Gamma_n/2$, $\mathrm{Im}[\lambda_n] = \Delta_n$. These eigenvalues are related to eigenmodes, that will be linear combinations of the $3N$ operators $\sigma_{j,\alpha}$, and that we can call $\hat{v}_n$ for $n \in \{1, ..., 3N\}$. Each one of these eigenmodes evolve on time in an independent way, since they are eigenmodes of the matrix K: We have

$$\frac{\mathrm{d}\hat{v}_n}{\mathrm{d}t} = \left(i\,\Delta_n - \frac{\Gamma_n}{2}\right)\,\hat{v}_n\ , \tag{2.51}$$

which has as a solution $\hat{v}_n(t) = \hat{v}_n(0)\mathrm{e}^{\left(i\,\Delta_n - \frac{\Gamma_n}{2}\right)t}$. In analogy with the single-atom case, we identify the imaginary part Γ_n of the eigenvalues to the decay rate of this mode, which can be different from the natural decay Γ. The modes that present $\Gamma_n > \Gamma$ ($\Gamma_n < \Gamma$) are called *superradiant* (*subradiant*), because the decay of the atomic excitation will be faster (slower) than for the independent atoms' case. This modification of the natural decay is an intrinsic collective phenomenon, much studied in the last few years in this linear regime (Araújo *et al.*, 2016; Scully, 2009). We also note that this linear superradiance is different from the initial prediction made by Dicke in his seminal paper, which is nowadays called Dicke superradiance. Dicke superradiance takes place for atoms interacting symetrically with the same light mode (as, for example, for atoms in a volume of size much smaller than λ), and in the opposite regime as the linear superradiance, i.e. for an excited population initially equal to 1.

The real part Δ_n of the eigenvalue represent a shift of $\Delta - \Delta_n$ of the resonance of the mode with respect to the bare atomic resonance. It is related to the collective Lamb shift of an atomic cloud (Manassah, 2012). The collective Lamb shift is the collective shift of center of the spectrum of a cloud of atoms, and can be (at least qualitatively) thought of as the average value of the shifts of each mode, weighted by the probability of excitation of the mode upon the incidence of the incoming laser.

2.2.2.1 Transmission of a Gaussian beam through an atomic cloud

The coupled dipole model can be used to calculate the transmission coefficient for light impinging on the cloud in a steady-state configuration. For that, we must use the couple dipoles model system of equations given at Eq. (2.46). Once the laser excitation is turned on, the atoms will begin to absorb and emit photons, and after some transient response of the cloud, of typical timescale Γ^{-1}, the atomic dipoles will reach a steady state. In this situation, the average value of the operators do not change anymore, and we can find their steady state values by setting the temporal derivatives to zero at Eq. (2.46), which produces a system of $3N$ linear equations with solution

$$\beta_{j,\alpha} = -i \sum_{\substack{n=1...N \\ \alpha=x,y,z}} (K)^{-1}_{j,\alpha,m,\gamma} \frac{\Omega_{m,\gamma}}{2} , \tag{2.52}$$

where $(K)^{-1}_{j,\alpha,m,\gamma}$ is the matrix element of K^{-1}, the inverse of the matrix K. This solution can be used to calculate the total electric field at any point of space, in particular at the direction of the incoming beam. Let's consider a Gaussian beam propagating in the z direction, that impinges on the atomic cloud (of center $z = 0$, same position as the focal plane of the Gaussian beam), that has the complex amplitude of its electric field given by

$$\mathbf{E}_0(\mathbf{r}) = E_0 \, \mathbf{e}_x \, \frac{w_0}{w(z)} \exp\left(\frac{-\rho^2}{w(z)^2}\right) \exp\left(-i\left(k_L z + k_L \frac{\rho^2}{2R_G(z)} - \psi_G(z)\right)\right) , \tag{2.53}$$

with $\rho = \sqrt{x^2 + y^2}$ the transverse distance to the propagation axis of the beam, $w(z) = w_0\sqrt{1 + \frac{z}{z_R}}$ the waist of the beam, w_0 the waist at the focal plane, $z_R = \pi w_0^2/\lambda_L$ the Rayleigh length, $R_G(z) = z\sqrt{1 + \left(\frac{z_R}{z}\right)^2}$ the radius of curvature of the wavefront of the beam, and $\psi_G(z) = \arctan\left(\frac{z}{z_R}\right)$ the extra Gouy phase acquired by the beam upon propagation. The incoming beam, of polarization in x direction, excites each atom with a Rabi frequency $\Omega_{j,x} = \mathrm{d}\,|\mathbf{E}_0(\mathbf{r}_j)|/\hbar$, $\Omega_{j,y} = \Omega_{j,z} = 0$, and the calculated $\beta_{j,\alpha}$ is used to calculate the total electric field in any point of space, which is the sum of the incoming and the scattered electric field. In the far field (i.e., for a distance $\gg \lambda_L$ of any atom), we can use Eq. (2.24) taken in the classical limit due to the linear regime of validity of the coupled dipoles model (i.e., replacing $\hat{\beta}^{(-)}_{j,\alpha}$ by $\beta_{j,\alpha}$) to obtain the total complex amplitude of the electric field at position $\mathbf{r}$:

$$\mathbf{E}_{\mathrm{tot}}(\mathbf{r}) = \mathbf{E}_0(\mathbf{r}) + \frac{\mathrm{d}\,k_L^2}{4\pi\epsilon_0} \sum_{j=1..N} \mathrm{e}^{ik_L|\mathbf{r}-\mathbf{r}_j| - i\omega_L t} \left[\frac{\left(\mathbf{e}_{r,j} \times \boldsymbol{\beta}_j\right) \times \mathbf{e}_{r,j}}{|\mathbf{r} - \mathbf{r}_j|}\right] , \tag{2.54}$$

with $\mathbf{e}_{r,j} = (\mathbf{r} - \mathbf{r}_j)/|\mathbf{r} - \mathbf{r}_j|$ the unitary vector that points from atom j to the observation point at $\mathbf{r}$. The attenuation of the incoming beam while passing by the atomic cloud must be an effect derived from the total electric field calculated from the expression above. This means that in the direction of the incoming beam, the light scattered by each atom has opposite phase with respect to the incoming light, and in this picture the attenuation of the light beam is seen as the destructive interference of the incoming light beam (the first term at the right side of the expression above) and the scattered light from the atoms (the second term at the right side of the expression above).

From this electric field, we can define a transmission coefficient, which should represent the relative transmitted power through the sample. There is more than one way of defining this transmission coefficient. For an incoming Gaussian laser beam, we can

think of the transmission as the amount of power that remains in the same spatial mode of the incoming beam, measured at a distance $Z \to \infty$ (in practice, the distance Z must be in the far field of the light emitted by the cloud and in the far field of the incoming Gaussian beam, which means that $Z \gg \pi R^2/\lambda$ and $Z \gg z_R$, with R the typical transverse size of the atomic cloud). For a definite realization of the atomic cloud, with each atom in a fixed position, we can calculate the projection of the total electric field in the incoming mode of the light, and normalize it to the incoming electric field, defining a (complex) transmission coefficient t_{G} as

$$t_{\mathrm{G}} = \frac{\int_{-\infty}^{\infty}\int_{-\infty}^{\infty} \mathrm{d}x\,\mathrm{d}y\,\mathbf{E}_{\mathrm{tot}}(x,y,Z)\cdot\mathbf{E}_0^*(x,y,Z)}{\int_{-\infty}^{\infty}\int_{-\infty}^{\infty} \mathrm{d}x\,\mathrm{d}y\,\mathbf{E}_0(x,y,Z)\cdot\mathbf{E}_0^*(x,y,Z)} \ . \tag{2.55}$$

For each realization of the atomic cloud for same average density and geometry, the atoms will have different positions, and the transmission t_{G} will fluctuate. It is most practical to measure directly the total transmitted intensity in the incoming light mode. The total transmitted intensity is proportional to the electric field squared, which means that the transmitted intensity, normalized to the incoming intensity, is given by $|t_{\mathrm{G}}|^2$. We then define the intensity transmission coefficient, averaged over many realizations of the atomic cloud, as

$$T_{\mathrm{G,I}} = \left\langle |t_{\mathrm{G}}|^2 \right\rangle \ . \tag{2.56}$$

Experimentally, this coefficient can be measured by coupling the transmitted laser beam in the far field to the input of a monomode, polarization-maintaining optical fiber, and measuring its intensity at the output of the fiber for many realizations of the atomic cloud. This average intensity is then normalized to the intensity measured in the absence of atoms, where no attenuation is to be expected (only of the passive optical elements in the light path, which are present with and without the atoms). We could also define a different transmission coefficient, based on the average transmitted electric field:

$$T_{\mathrm{G,coh}} = |\langle t_{\mathrm{G}} \rangle|^2 \ . \tag{2.57}$$

We say that this is the coefficient of the *coherent* transmission, because it only considers the portion of light that keeps a definite phase relation with the incoming light after averaging over atomic positions. Mathematically, using the Cauchy-Schwarz inequality, it is possible to verify that

$$T_{\mathrm{G,I}} \geq T_{\mathrm{G,coh}} \ . \tag{2.58}$$

Physically, we must have phase coherence of the transmitted electric field (with respect to the phase of the incoming field) for the equality to hold. Any mechanism that randomizes the phase of the transmitted electric field will produce a reduction of the averaged electric field with respect to the amplitude of the electric field at each realization, and thus will entail $T_{\mathrm{G,coh}} < T_{\mathrm{G,I}}$.

Which physical mechanisms could reduce the coherence of the transmitted light, (partially) randomizing the phase of the light transmitted in the direction of the incoming beam? In the linear regime, where $\hat{\boldsymbol{\beta}}_j \simeq \boldsymbol{\beta}_j$, the light directly scattered in the direction of the incoming radiation is purely elastic and phase-locked with respect to the incoming radiation, because of the phase of the atomic coherence that is inherited from the laser excitation, and the light path which is the same for all scattered photons. On the other hand, the light which is *multiply scattered* to the direction of the incoming radiation (i.e., scattered to another atom, and eventually to others, until being rescattered at the direction of the incoming light again) corresponds to the sum of scattered light with different optical paths; those paths strongly depend on the specific atomic positions at each realization of the atomic cloud, which means that the electric field of the multiply scattered light is random with respect to the light of the incoming beam. The multiple scattered light, thus, only contribute to $T_{\mathrm{G,I}}$, but not to $T_{\mathrm{G,coh}}$.

Another effect that reduces the coherence of the transmitted light is the presence of inelastic scattering, due to the quantum fluctuations of the atomic coherences when the atomic populations are not negliglble (Cohen-Tannoudji; Dupont-Roc; Grynberg, 1998). The spectral broadening of the inelastic component of the light scattered by the atoms entails fluctuations on the light phase, which for $Z \to \infty$ gives a totally random phase with respect to the incoming field. The inelastic component of the scattered light will only contribute to $T_{\mathrm{G,I}}$, but not to $T_{\mathrm{G,coh}}$.

2.2.3 A random walk model for the light diffusion

In a certain regime, it is possible to simulate the light scattering by the atomic cloud as a random walk of photons, just like classical point particles bouncing on the atoms. This model can be interpreted as a Monte Carlo treatment of the wave light diffusion, where the trajectories of single photons are calculated from the diffusion probability of light within the atomic sample. In practice, the numerical implementation of the random walk model calculates the trajectories of many of such photons, taking into account the spatial distribution of the atoms, $\rho_a(\mathbf{r})$, and the thermal distribution of velocities in a specific direction,

$$\rho_v(v_\alpha) = \frac{1}{\sqrt{2\pi}v_{\mathrm{RMS}}} \mathrm{e}^{-\frac{v_\alpha^2}{2v_{\mathrm{RMS}}^2}} , \tag{2.59}$$

with $v_{\mathrm{RMS}} = \sqrt{\frac{k_B T}{m}}$ the root mean square velocity in one direction. For photons of initial detuning Δ_0 with respect to the atomic bare resonance, propagating from the initial position $\mathbf{r}_0$ with propagation direction $\mathbf{e}_{k,0}$ and polarization direction $\mathbf{e}_{p,0}$, the fraction of them having not been scattered after a propagation length l can be calculated in the same way as Eq. (2.34), giving a probability distribution $\mathcal{P}_0(l)$, with

$$\mathcal{P}_n(l) = \mathrm{e}^{-\sigma_l(\Delta_n)\int_0^l \mathrm{d}l' \rho_{\mathrm{a}}(\mathbf{r}_n + l'\,\mathbf{e}_{k,n})} \quad . \tag{2.60}$$

Just as for the derivation of the Beer-Lambert law, this result does not take into account the effect of other atoms for the scattering of a first atom. For this to hold, the scattering must be in the linear regime; also, the density of the sample should not be high. Collective effects linked to the density of the cloud will be absent here, as it was the case for the Beer-Lambert law. On the other hand, this model will be able to capture the influence of the multiple scattering on the light transmitted by the cloud.

The distribution probability $\mathcal{P}_0(l)$ is used to decide if, and where, the photon has been scattered. If the photon was scattered at position $\mathbf{r}_1$, then we pick up randomly the new propagation direction $\mathbf{e}_{k,1}$ with a weight given by the angular distribution of the dipolar emission of an atom excited with light of polarization $\mathbf{e}_{p,0}$ (see Eq.(2.25)): The angle $\theta_p = \arccos(\mathbf{e}_{k,1} \cdot \mathbf{e}_{p,0})$ is sorted with weight $\propto \sin(\theta_p)^3$, while the azimuthal angle ϕ_p is uniformly distributed. The new photon polarization is also obtained from the dipolar emission (see Eq.(2.24)) as $\mathbf{e}_{p,1} = \frac{(\mathbf{e}_{k,1}\times\mathbf{e}_{p,0})\times\mathbf{e}_{k,1}}{|(\mathbf{e}_{k,1}\times\mathbf{e}_{p,0})\times\mathbf{e}_{k,1}|}$. Finally, we also need to sort the velocity $\mathbf{v}$ of the atom that scattered the photon, by using the probability distribution of Eq. (2.59) to sort each component of $\mathbf{v}$. This velocity is used to calculated the new light detuning, following Eq. 2.32), as

$$\Delta_1 = \Delta_0 - k_L \mathbf{v}\cdot(\mathbf{e}_{k,0} - \mathbf{e}_{k,1}) - \frac{\hbar k_L^2}{2m}\left|\mathbf{e}_{k,0} - \mathbf{e}_{k,1}\right|^2 \quad . \tag{2.61}$$

Note that the velocity distribution of the atomic cloud does not evolve on time in this model; this means that we do not consider any heating effect related to the photon scattering.

We proceed again as above, based now on the survival probability distribution $\mathcal{P}_1(l)$, and so on, until the photon escapes the cloud. At each step n, the photon has a probability of $\mathcal{P}_n(\infty)$ of escaping the cloud; once this arrives, the frequency Δ_n, the propagation direction $\mathbf{e}_{k,n}$ of the photon and is polarization $\mathbf{e}_{p,n}$ are registered by the simulation, in order to compute the frequency distribution and the angular distribution of the light scattered. In particular, we can compute the cloud transmission by looking at the fraction of photons that are scattered within the spherical angle that is determined by the propagation of the incoming Gaussian beam in the far field. The Gaussian beam has a

typical divergence in the far field which is related to its waist at the focal plane, $\theta_G = \frac{\lambda}{\pi w_0}$, inside which a fraction of the photons will be found.

3 EXPERIMENTAL DESCRIPTION

3.1 Strontium – Our chosen atom

In our experiment we use the isotope Strontium-88 as atomic species. For this part, we'll discuss some atomic properties of this element, as well as other remarkable experiments involving the same atom.

Strontium is an alkaline earth metal with 2 electrons in the valence shell (the electronic distribution is: $1s^2\,2s^2\,2p^6\,3s^2\,3p^6\,3d^{10}\,4s^2\,4p^6\,5s^2$), resulting in Helium-like energy levels with the appearance of singlet and triplet states. It can be found naturally in 4 different isotopes, with the ^{88}Sr being responsible for 82.58% of the natural occurrence. Other abundances and properties can be seen in Table 1.

Table 1 – Natural occurrence of Strontium isotope and its properties.

Isotope	Abundance	Particle type	Isotope shift (MHz)
^{88}Sr	82.58%	bosonic	0
^{86}Sr	9.86%	bosonic	-46.5
^{87}Sr	7%	fermionic (I = 9/2)	-124.8
^{84}Sr	0.56%	bosonic	-270.8

Source: by author.

Recently strontium has attracted great interest from the atomic and metrology community because of its electronic structure. Beyond the natural occurrence of singlet (J = 0) and triplet (J = 1) states, the natural repulsion between electrons due to Pauli's exclusion principle provided the ground state to be a singlet level, as can be seen in the energy diagram in Figure 3. As a result, for the bosonic isotopes, the ground state is non-magnetic and weakly interacting, making it a good candidate for metrology applications. Moreover, the inter-combination lines, connecting singlet and triplet states are forbidden in first-order resulting in very narrow clock-transitions, making Strontium a good candidate to be the future time reference (Ball, 2013).

For the atomic community, the two electrons make strontium useful for Rydberg physics and applications, since it's possible to excite one of the electrons to a Rydberg level while using the remaining one for probe and other applications. The inner electron can be then used to trap the atom, or to read in a nondestructive way the state of the outer electron (Lachaud *et al.*, 2024; Muni *et al.*, 2022).

In our laboratory, we are interested in studying light-matter interactions focused on light-induced interaction between atoms, making the bosonic isotopes of Strontium

good candidates because of the true J = 0 → J = 1 transition. Moreover, the ^{88}Sr has a very low scattering cross-section for s-wave collision $a_0 = -1.2a_B$ (Stellmer; Grimm; Schreck, 2013), enabling the production of high-density clouds without the losses through the 3-body collision channel (Krstajić *et al.*, 2023). The light-mediated interaction we would like to study starts to be important in the regime of spacial densities $\rho = 10^{14}$ atoms/cm^3.

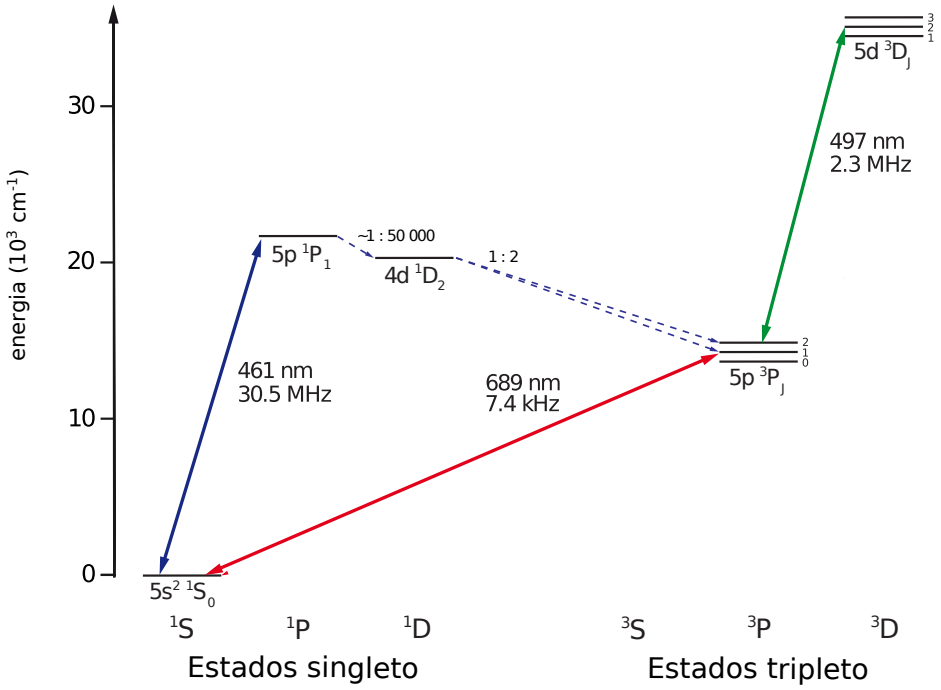

Figure 3 – ^{88}Sr energy levels: in this figure, we present only the energy levels relevant to our experiment.

A few drawbacks of using Strontium as an atomic species are the need for different laser systems for atomic manipulation, and different stabilization methods to achieve the various regimes of linewidth necessary. From the energy levels presented before, at least three wavelengths are needed: the 461 nm, which we'll call **blue**, the 689 nm, called **red**, and the 497 nm called **green** or **repumper**. For the stability of these laser systems, it is necessary a range of linewidths, going from MHz to kHz. More details about this will be given later.

Unlike mostly alkaline species, alkaline-earth metals have high melting points, making necessary temperatures as high as 800 K to ensure enough flux of atoms in an atomic oven. A vapor pressure curve for Strontium can be seen in figure 4. We usually operate our oven at a temperature of 600 ºC, but more details are given in the 3.4.1 section.

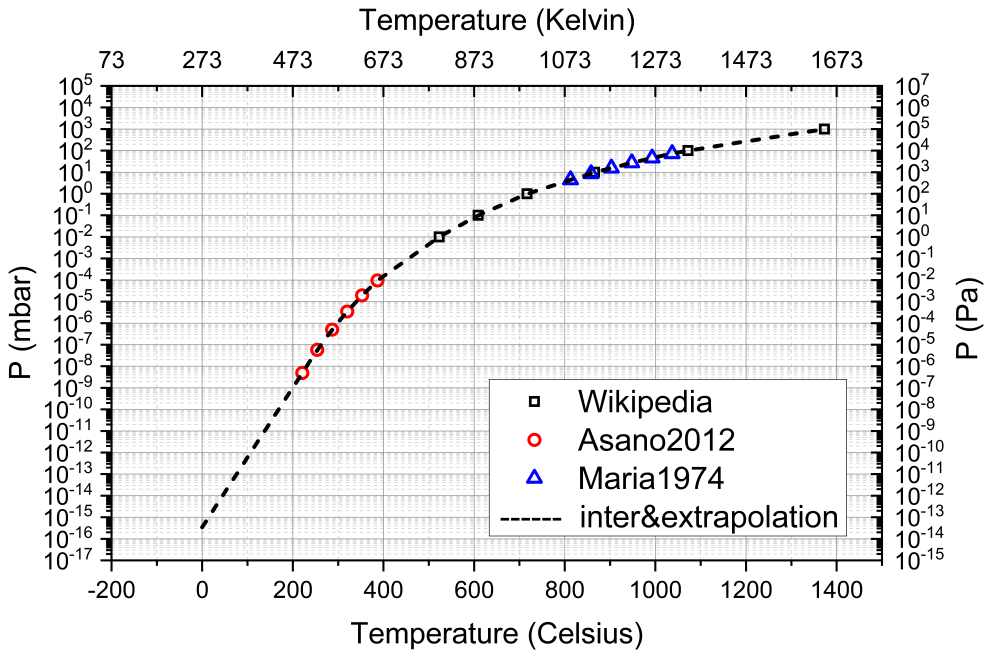

Figure 4 – Vapor pressure for Strontium. The data from the graph is from (Asano; Kubo, 1978) and (Maria; Piacente, 1974), and the extrapolation follows the Antoine equation.

3.2 Laser systems - How to address the atoms

In our experiment we work with neutral atoms; moreover, due to the absence of angular momentum in the ground state (J = 0 for the $^1S_0$), ^{88}Sr has no sensibility to magnetic fields, so the only way to interact with it is through the use of lasers, either using radiation pressure or dipolar potentials. In the following, a brief description of the laser systems used to capture, cool, and probe the atoms is provided. Beyond the three wavelengths mentioned before, we will also cover the extra 1064 nm laser, called **Mephisto** used to produce an Optical Dipole Trap (ODT).

3.2.1 Remarks on Gaussian beams

Before going to the description of each one of the laser systems, it is important to describe the spatial properties of the laser beam. In general, except when explicitly mentioned, all lasers have the spatial distribution of intensity given by a Gaussian beam. The Gaussian distribution for a propagating wave is a solution of Helmholtz's equation in the paraxial approximation with cylindrical symmetry (Kogelnik; Li, 1966). The intensity of this laser beam have the following form:

$$I(r,z) = \frac{2P}{\pi\omega(z)^2}\left(\frac{\omega_0}{\omega(z)}\right)^2 \exp\left(-2\frac{r^2}{\omega(z)^2}\right) \tag{3.1}$$

where: P is the total power in energy units, ω_0 is the radius of the beam at $z = 0$ and $\omega(z)$ is a function describing the beam radius evolution during its propagation. The evolution of the radius ($\omega(z)$) is given by:

$$\omega(z) = \omega_0\sqrt{1 + (z/z_R)} = \omega_0\sqrt{1 + z/(\pi\omega_0^2 n/\lambda)} \tag{3.2}$$

where: n is the index of refraction of the medium at which the beam is traveling, λ is the wavelength of the wave, and z_R is the Rayleigh range of the beam. To conclude, when mentioned in the future the radius of the beam is refereed to ω_0, the diameter is given by $2\omega_0$ and the Rayleigh range is z_R.

3.2.2 Blue lasers

The most strong transition is the dipole-allowed transition $^1S_0 \rightarrow {}^1P_1$ with a wavelength of 461 nm and a linewidth of 30.5 MHz. Because of the high scattering rate, this transition is good for capture and cooling hot atoms, being the most used transition in our experiment.

For the optical table we have two lasers responsible for generating this wavelength, one responsible for the main source of optical power and a second one used to produce light with a variable detuning from the atomic resonance. They are called **blue** and the **baby-blue**, respectively.

3.2.3 Main **blue**

The first one is a second-harmonic generator laser from Toptica model TA-SHG-Pro. Despite being a commercial laser, Toptica provides some good schemes from the internal part of the laser, available in figure 5. To briefly describe it: The light starts with an IR laser diode providing 40 mW of power, this light is sent to a Tapered Amplifier (TA), which produces around 1.7 W of light at 922 nm for 2700 mA. The current TA is a more powerful one, and was exchanged to increase the total laser power. A curve of TA power vs. TA current is available in figure 6.

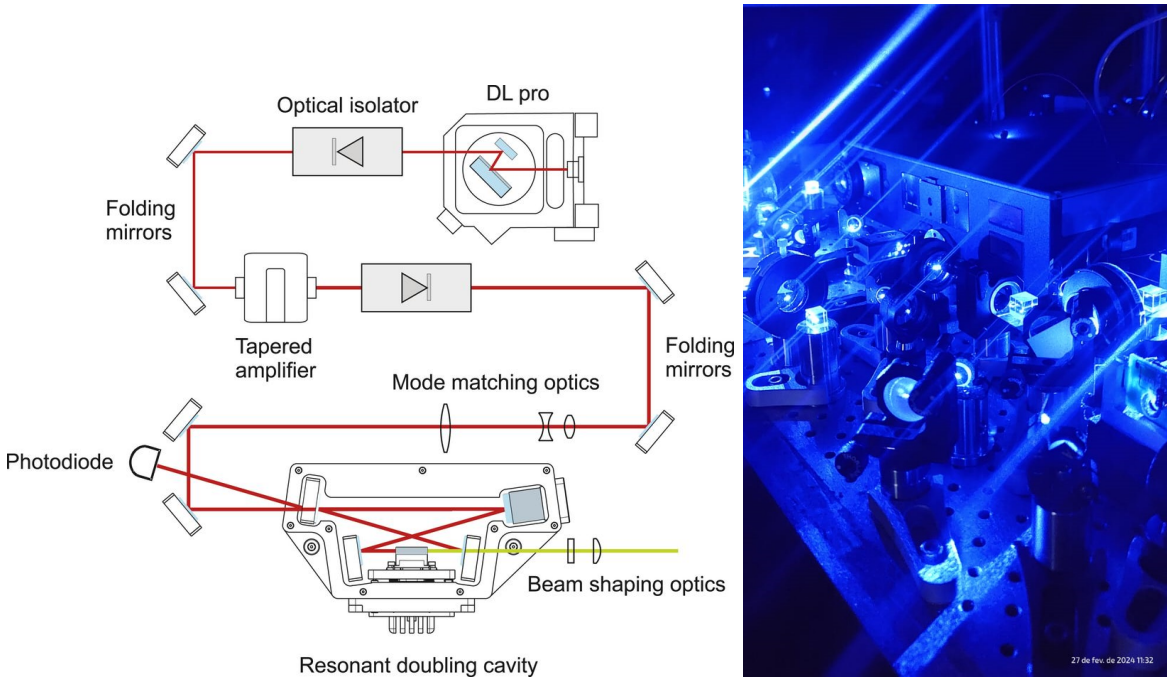

Figure 5 – left: internal scheme of TA-SHG-Pro extract from (TOPTICA-Photonics,); right: photo of optical table with **blue** in the background.

After this amplification, the light is mode-matched to maximize the coupling in the doubling cavity. This bow-tie cavity has a non-linear crystal responsible for producing one 461 nm photon for every two 922 nm photons. The crystal temperature is also adjusted to ensure phase-matching in the frequency doubling process (see figure 6 right).

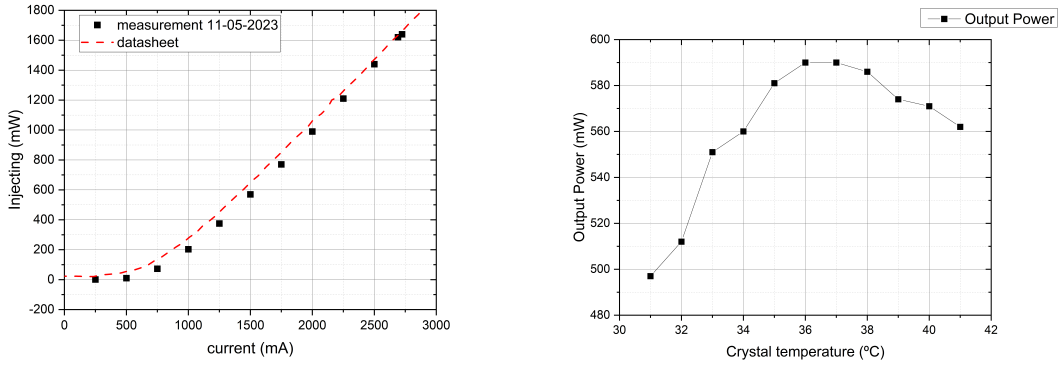

Figure 6 – left: TA power vs. supply current, the squares are measurements while the dashed curve is the data-sheet; right: Total 461 nm power vs. doubling crystal temperature. The crystal temperature is adjusted to ensure phase-matching, making the frequency-doubling process more efficient.

This laser, from now on called **blue**, is our main source of power in $^1S_0 \rightarrow {}^1P_1$ transition. In total, we get around 600 mW of blue light that will be divided according to the need of power. Most of the time the amount of power is decided through the

optimization of the atomic cloud, looking for either maximizing the atoms' number or minimizing the cloud temperature, so it is important to keep in mind that the values mentioned in here are compromised by this, and also by the total available power.

All the available power is concentrated in one beam that is going to be divided into several others. The easiest way to divide a laser beam is by controlling its polarization and using a polarizing beam splitter cube (PBS) to divide the power into its orthogonal components. In this way, using a combination of one half-waveplate and a PBS it is possible to divide one beam in two with orthogonal polarization and also in orthogonal directions.

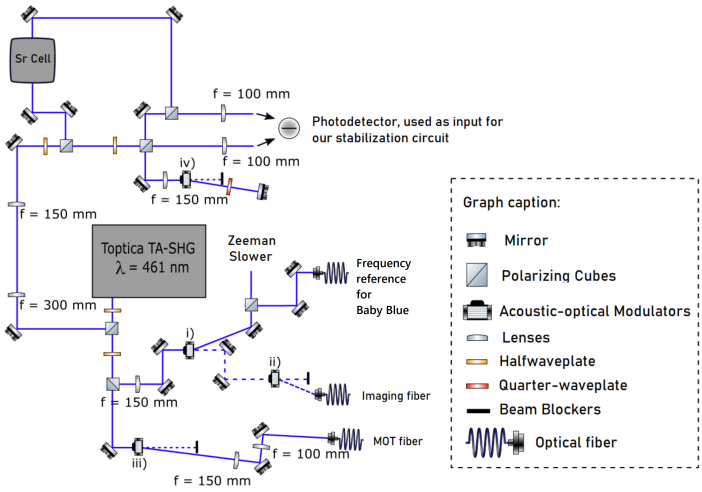

Figure 7 – Scheme of the optical table that creates all beams derived from the blue laser.

At the output of the laser, we have an elliptical beam with a radius of (1.086 ± 0.006) mm and (0.863 ± 0.005) mm, given an average Rayleigh-range $z_R = (6.55 \pm 0.04)$ m. The **blue** laser will be divided into the following laser beams: blueMOT, Zeeman, beat signal, Spectroscopy, and Probe-H. Following is a short description of each:

- blueMOT: This beam is the light used to produce the blueMOT, after a fiber its size is adjusted producing a beam with 12.7 mm. This beam is red-shifted from the atomic resonance by a value of 48.5 MHz using the +1 order of an AOM driven with radio frequency (RF) of 70.2 MHz. The power after the fiber is 27 mW, however, this is split into three beams for each arm of blueMOT.

- Zeeman: This beam is the first one responsible for decelerating the atoms, together with the magnetic field they form the Zeeman slower, described in more detail further. After the AOM we have 124 mW of power red-shifted by 385.8 MHz from the resonance using the -1 order of an AOM driven with a frequency of 267.1 MHz. The beam is expanded but focused on the output of the oven with a radius of 4 mm.

- beat signal: The baby-blue laser has a stabilization system that makes it easy to scan its frequency up to 1 GHz around the resonance. For **baby-blue** stabilization, we'll

use this beam to make a beat-note between **blue** and **baby-blue**. It is produced by sampling some power from the Zeeman beam, around 8 mW, to be coupled in a 75:25 fiber.

- Spectroscopy: For the **blue** stabilization we use a homemade Strontium vapor cell. To extract the absorption signal we use the technique of Saturation absorption spectroscopy with this beam being used to produce the pump and the probe. The probe has the same frequency as the **blue** while the pump frequency is changed using an AOM in a double-pass configuration (Donley *et al.*, 2005). The RF for this AOM is modulated with a central frequency of 112.3 MHz and a modulation depth of 24 MHz.

- Probe-H: This beam is responsible for making the absorption imaging of the atoms, it is resonant with the atomic transition using the +1 order of an AOM with RF at 118.7 MHz. To avoid the saturation effect the beam has a size of 5 mm and a total power of 300 μW.

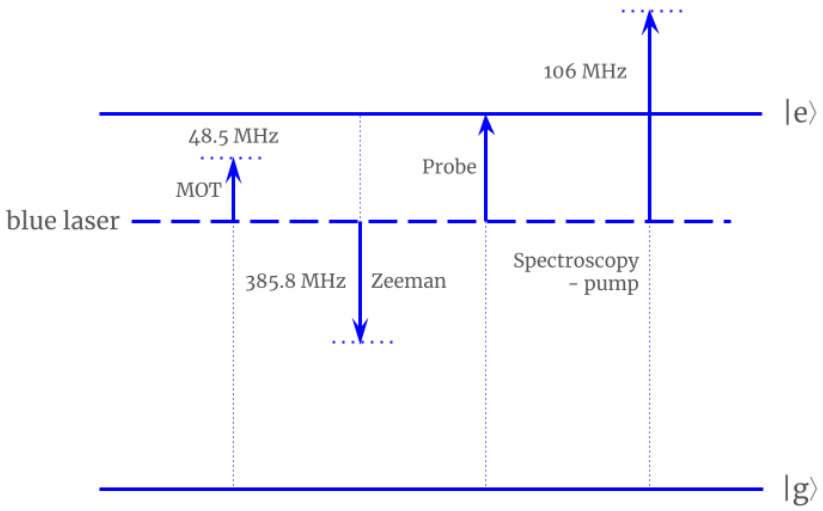

Figure 8 – Frequency scheme for all laser beams mentioned before. The figure is representing the blue transition so $|g\rangle$ refers to $^1S_0$ and $|e\rangle$ refers to $^1P_1$. The scheme is out-of-scale.

3.2.3.1 Spectroscopy cell - The reference of frequency

While the power stabilization is provided from the double-cavity lock-in we use a Spectroscopy cell to ensure the frequency stabilization. As mentioned before, when working with Strontium is needed to heat the element until high temperatures to enable some reasonable amount of atoms in the gas phase. Our spectroscopy cell is a homemade one welded by the mechanical workshop. It's composed of a cylindrical tube and a small reservoir where one may load pieces of Strontium.

The geometry of the cell is also justified by the high temperature we need to reach. Regular vacuum windows cannot be heated to more than 150 °C, this low temperature could cause the Strontium gas to deposit over the glass and block the beam from passing. We avoided this with a long tube and also added a small pressure of Argon to work as a buffer gas that will stop the strontium atoms before hitting the windows (Shiga *et al.*, 2009).

Strontium is also very reactive with oxygen, forming strontium-oxide (SrO), to prevent metal oxidation during the filling process we first load the Strontium and make a quick vacuum using a turbo pump. Later, with most of the air removed, we break the vacuum with Argon gas and start pumping again until a pressure of roughly 1 mbar of Argon remains. Although the pressure of the buffer gas is important, since too high pressure may deform the absorption line while too low could not be enough for a buffer gas, we found this method is sufficient to ensure a good line shape and also avoid the clogging of windows.

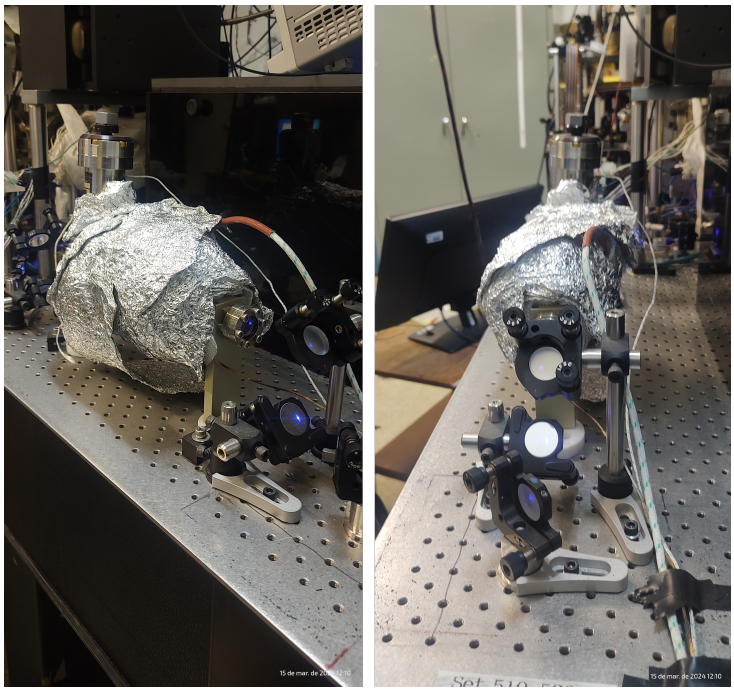

Figure 9 – Pictures of the spectroscopy cell wrapped with glassfiber and aluminium foil, the probe beam is also shown in the picture on the left in the 45-degree mirror.

The normal temperature of cell operation is around 316 ºC (see the pictures in figure 9), at this temperature the Doppler broadening of the gas is 512 MHz, much larger than the linewidth we want to resolve. To solve this problem we use the saturation absorption spectroscopy technique (Raven, 2024).

The idea is to use two beams, called pump and probe, with very unbalanced power ($P_{pump} \gg P_{probe}$) but the same detuning Δ from the resonance. Sending both beams

counter-propagating, because of Doppler's effect, each one will interact with a different class of velocities, but with the same modulus that compensates the Doppler's effect: $\Delta = \vec{k} \cdot \vec{v}$. If we monitor the absorption of the probe beam as a function of the detuning, when $\Delta = 0$, both beams interact with the same class of velocities $\vec{v} = 0$, but because of the power difference, the pump beam saturates the atoms and the transmission of probe beam increases. This results in a small *peak* in the middle of Doppler's absorption profile, see the figure 10 below.

In our case, the pump and probe do not have the same frequency, since the pump beam has its frequency shifted by 2×112.3 MHz. One may redo the calculations to find out that in this situation the class of velocities at which both beams interact together is not the stationary one, but the one for which the Doppler shift is equal to half the frequency difference $\vec{k} \cdot \vec{v} = f$. This is also the explanation for the resonance not being centered in the Doppler absorption curve in figure 10. We may also find that in the condition where both beams interact with the same class of velocities, their detunings are opposite: $\Delta_{pump} = -\Delta_{probe}$, resulting in the pump beam being above resonance and the probe beam below. Since the probe beam has the same frequency as **blue**, the light from the laser is below resonance.

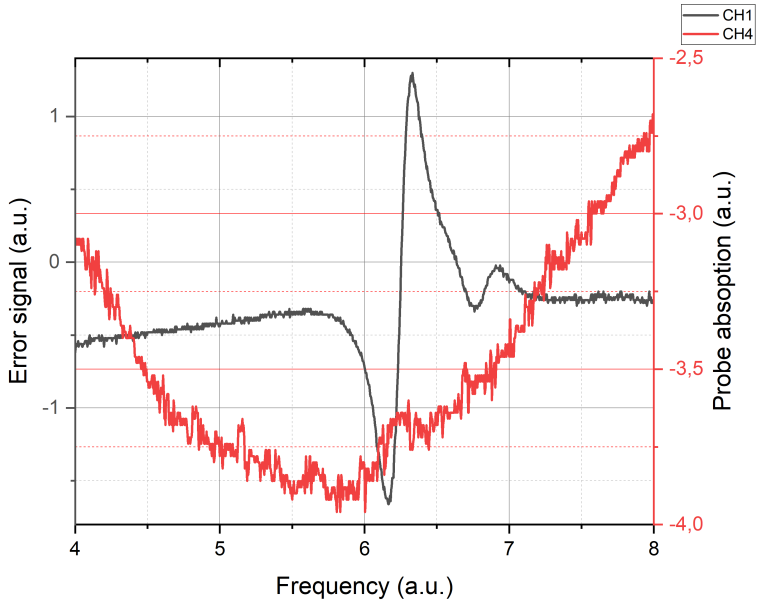

Figure 10 – Absorption curve showing the Doppler distribution with the saturated absorption peak in red, and error signal used for **blue** stabilization in black. One may also check for an extra dispersive peak from the absorption of ^{84}Sr isotope to the right.

To filter the noise and also transform this *peak* in a dispersive signal, which is more suitable for stabilization, we use the lock-in technique (Weel; Kumarakrishnan, 2002) modulating the frequency of the pump beam by an amplitude of 24 MHz with a

frequency of 900 Hz. This modulation is transferred to the probe signal through the atoms. After demodulating this absorption we have the error signal used for the stabilization. In conclusion, the lock-in technique has enough precision to resolve another absorption, at first invisible at the absorption curve, from the ^{84}Sr isotope, the small error signal at the right in 10.

3.2.4 **Baby-blue**

The **baby-blue** is the second laser system we used to drive the atoms at $^1S_0 \rightarrow {}^1P_1$ transition. This is a DL-Pro that produces around 30 mW of optical power.

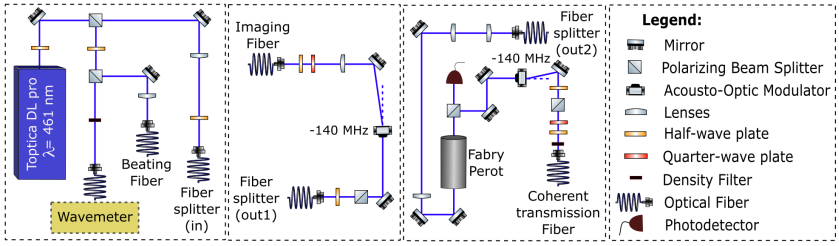

Figure 11 – Optical table scheme for the several light beams derived from the **baby-blue**.

The light from this laser is divided into 4 beams at the output, they are wavemeter, beat signal, Probe-V (sometimes also called ThorCam Probe), and Coherent transmission, in more detail:

- wavemeter: as the name suggests this beam is coupled into a fiber that goes to the wavemeter for continuous frequency monitoring. For this one, the power varies because of the fiber coupling, but roughly we have a few hundreds of uW.

- beat signal: This beam is responsible for the beat note with the Zeeman beam and serves as the reference for the stabilization of the **baby-blue**.

- Probe-V (or ThorCam Probe): This is the beam used for the vertical imaging system. Since the frequency for this laser can be easily varied it doesn't have a fixed detuning, but the light pulses are created using an AOM using the -1-order and RF with frequency of 118.7 MHz.

- Coherent transmission: This is the beam we used the most for probing the transmission of the cloud. Before going to the atoms the light from this beam is also frequently filtered using a Fabry-Perot (FP) cavity. After the installation of the FP cavity, we noticed a strong disturbance of the diode emission because of FP reflection, so we had to install another optical insulator before the FP cavity.

3.2.4.1 Offset lock - Transferring the stability

To probe the very high spatial densities we achieve, up to OD = 50, we have a dispersive imaging system called Phase-Contrast Imaging (PCI) (Fernandez *et al.*, 2025). In contrast with the more traditional Absorption Imaging (AI), which usually requires resonance or close-to-resonance light, for PCI it is necessary far-from-resonance light to avoid absorption so that we can probe only the phase change in the phase-front of the light beam. To be more quantitative, for a cloud with a given OD, it is enough to have a detuning of the same amount in units of Γ (Δ =OD$\times\Gamma$).

This requires a flexible stabilization system that allows some considerable change in the frequency of laser light, up to 1 GHz. We achieve this through an offset-lock system. The idea is to use a beat-note between the **baby-blue** and the reference Zeeman beam, comparing the frequency of this beat with the frequency of some RF generator (model: SG440L from DS Instruments) and stabilize the **baby-blue** to keep this frequency difference constant. With the **blue** stabilized at the spectroscopy cell, using this offset lock we can transfer the stability in frequency from the **blue** to **baby-blue**.

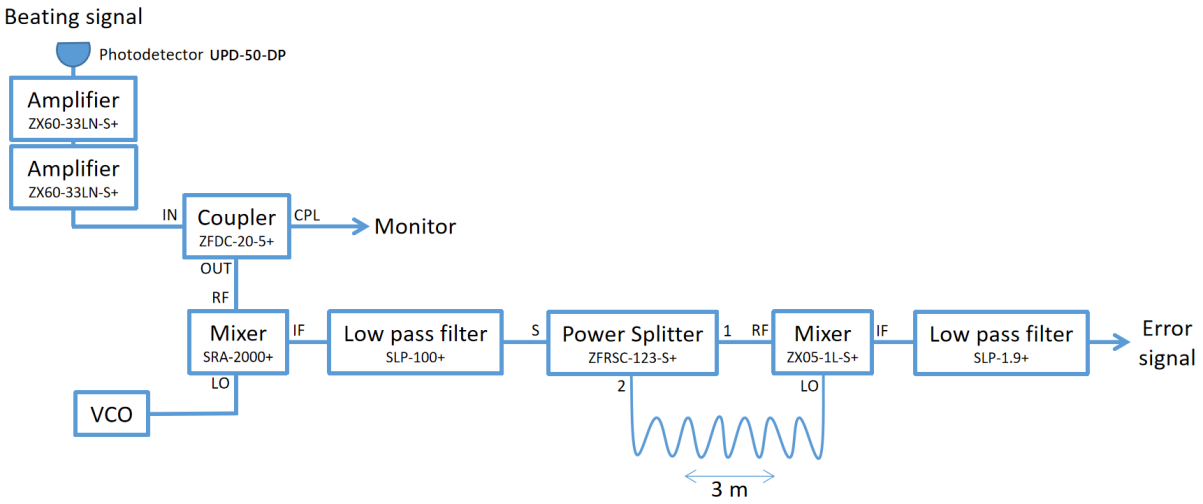

Figure 12 – Electronics for creating the error signal from the beating signal detected at the fast UPD-50-DP photodetector.

To assemble the whole system we used RF components from mini-circuits, while to collect the beat note we used a high-frequency photo-detector from ALPHALAS model UPD-50-DP with a response time of 50 ps. We continuously monitor the frequency of the beat-note using the CPL output on the ZFDC-20-5+ component (see figure 12).

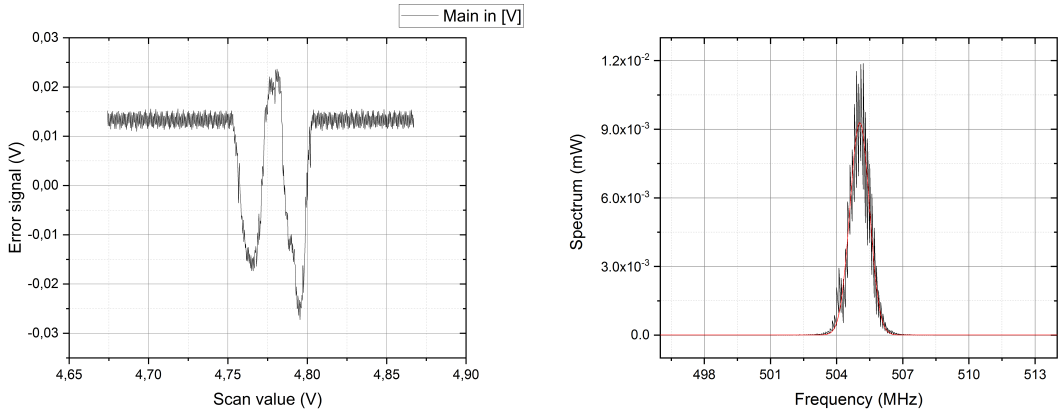

Figure 13 – Left: Error signal resultant from the offset locking circuit. Because of some imperfections with the mixer our baseline is not around zero, so we add as small offset. It's possible to use any zero-crossing points for locking. Right: Beat-note for the laser locked, from a Gaussian fit of the curve we extract the width as (880 ± 10) kHz, meaning both lasers have a stability better than MHz.

For the stabilization, we connect the output from the low-pass filter SLP-1.9+ which serves as an error signal in a Digilock module from Toptica. A typical error signal curve can be found in figure 13. The number of oscillations is proportional to the bandwidth of the low pass filter after the first mixer.

The stability of the system is then given by the width of the beat note. This width is a convolution of both lasers' stability but still serves as an upper limit on each laser frequency stability. In the best conditions, we have this beat note with a typical width of (880 ± 10) kHz.

In our arrangement of frequencies, both the ThorCam Probe and Coherent transmission beam have the same constant shift of - 118.7 MHz. Moreover, the Zeeman beam has a detuning of -385.8 MHz, while the frequency of the beat-note is defined as $f_{beat} = f_{baby-blue} - f_{Zeeman}$. Now, to have ThorCam Probe at resonance we need $f_{baby-blue} = -f_{ThorCam}$, which means $f_{beat} = 504.5$ MHz, roughly the condition shown.

3.2.5 Green laser - dealing with meta-stable states

A closed transition is when there is only one possible decay: back to the initial state. In the case of the $^1S_0 \rightarrow {}^1P_1$ transition, it's not closed, since it has a very small, 1:50.000 probability of the atom to decay to the $^1D_2$ level. From this intermediate level the atom could decay either to $^3P_1$ or $^3P_2$. While the $^3P_1$ level has a lifetime of 21 µs, the $^3P_2$ is a problem with a few seconds lifetime, which promotes the loss of these atoms from the cooling cycle. To recover them we add a laser resonant at the transition $^3P_2 \rightarrow {}^3D_2$ (green transition in figure 3).

The 497 nm wavelength is of difficult experimental production using laser diodes, so in our laboratory, we produce it through frequency doubling using a Toptica TA-SHG-Pro. This laser is similar to the **blue** laser but without the TA stage, at the end, we get 55 mW of light at 497 nm. We also don't stabilize this laser since a very few photons exchanged already repump the atoms, and so we can afford some detuning with no huge consequences for the atom number. Even though the loss channel is quite small (1:100 000), we observe an increase of 23-fold in atoms number once the green laser is added, being essential for the experiment.

3.2.6 Red laser system - Driving the narrow transition

As mentioned before, strontium has singlet (J=0) and triplet (J=1) levels. In first-order, light cannot drive a transition from singlet to triplet levels, because the transitions promoted by the optical dipole cannot change the total spin ($\Delta S = 0$). However, there is some contamination in the $^3P_1$ level by the $^1P_1$ that allows this transition. The transition $^1S_0 \rightarrow {}^3P_1$ is then called inter-combination line. As a result, this is a narrow transition with a linewidth $\Gamma = 7.4$ kHz, so our stabilization system needs to achieve stability better than this.

To increase the power available for driving the transition we use a diode in the master-slave configuration through the injection locking. With the laser diode powered but without feedback, we may insert some small amount of the master laser, already stabilized, as the seed to force the slave to laser at the same frequency. This way of increasing the power ensures the slave emission has the same linewidth as the master. Below is the description of the light emission for master and slave.

3.2.6.1 Red master

The master laser is a DL-Pro with 12 mW of power. This laser also has a fiber dock at the output that guarantees the alignment, as well as, good output mode. As a frequency reference, we use a *super cavity* from UltraStable company made in Zerodur material under a vacuum of 10^{-7} mbar, with very good reflection mirrors. The Zerodur is a glass-ceramic material with both amorphous and crystalline components. The most remarkable property is the low thermal expansion coefficient that crosses zero at a specific temperature; this occurs in the crossing of amorphous and crystalline phases, where the expansion coefficients have opposite signals, canceling each other.

For the FP etalon, this ensures a cavity with a stable size as a frequency reference. Our cavity has a length of 100.05 mm with a free spectral range (FSR) of 1.5 GHz, together with the *Finesse* of 20000, which results in a transmission linewidth of 75 kHz. Using the Pound-Drever-Hall technique (Black, 2001) we can effectively decrease the linewidth of the master laser. In our laboratory, we have two uncorrelated lasers, each one stabilized in

a different *supercavity*, in this way, the width of the beating between both lasers gives the upper limit of frequency stabilization for each.

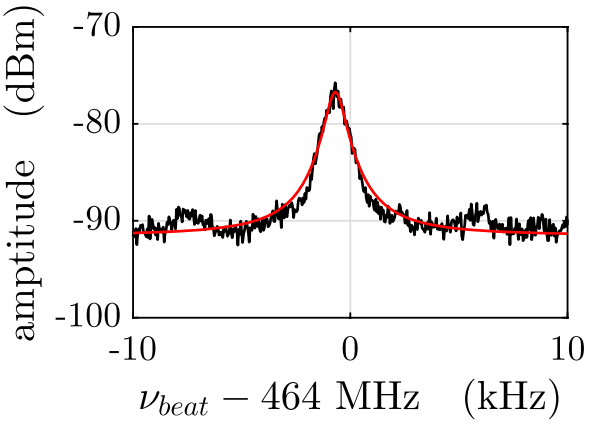

Figure 14 – Beat signal of a beam derived from our red laser and a beam derived from a red laser of the other cold Strontium machine of our group, separated in frequency by 464 MHz. The bandwidth of the spectrum analyser is 10 Hz. The Lorentzian shows a width of 450 Hz.

3.2.6.2 Red slave

Although the saturation intensity of the $^1S_0 \rightarrow {}^3P_1$ transition is quite low, $I_{sat} = 3$ $\mu W/cm^3$, due to the multiple stages of the redMOT, to be described later, we need more power. To amplify this power we use the injection lock technique (Stover; Steier, 1966) that consists of injecting a seed in a powered laser diode. For this, we have a homemade laser mount with temperature control, and using an optical insulator we inject around 18 μWto obtain 20 mW of laser power.

The light injected into the slave is the one transmitted from the supercavity. As mentioned before the FSR of this super-cavity is 1.5 GHz, this means, in the worst case, the $^1S_0 \rightarrow {}^3P_1$ resonance is between two consecutive cavity resonances, which is our case. For the stabilization, we decided to use the cavity resonance just before the atomic resonance, so is necessary to use an AOM to increase light frequency by 800 MHz before sending it to the slave.

This AOM needs to be driven by a very stable RF, for this, we use a RF generator from Rhode&Schwars model SMB-100A. This equipment has a linewidth stability better than a few Hz, ideal for our application. The AOM is mounted in a double-pass configuration allowing the central frequency modulation without loss of efficiency. After this AOM the light is mode-matched to maximize the injection efficiency with the use of an anamorphic prim pair and injected in the slave.

For monitoring the injection locking, we have a FP cavity where one can see the change in light frequency profile when it's free running or injected. Before being sent to atoms the light power is controlled using a second AOM driven by a frequency synthesizer

PLOX150-10 from Luff Research. This frequency synthesizer uses the Rhode&Schwarz 10 MHz output, ensuring again a stable linewidth. The light power is controlled through the modulation of AOM diffraction efficiency controlling the total RF power using two alternators (model: ZX73-2500-S+) in series, before the RF amplifier. This allows a logarithm control of light power.

The redMOT beam size is of (5.1 ± 0.2) mm, and the maximum power is around 12 mW, however, this power can be precisely tuned through several orders of magnitude, going from thousands to just a few I_{sat}, available in figure 15.

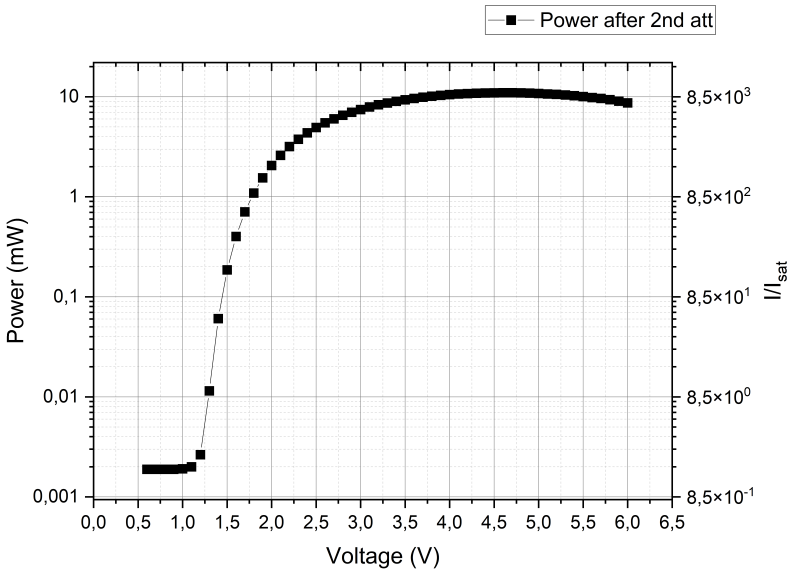

Figure 15 – Attenuation for redMOT light, controlled using the variable attenuator ZX73-2500-S+ from Mini-Circuits, applied to the RF that controls the beam diffraction at an AOM. With this, we may control the power for redlight from a few thousand of I_{sat} to a little less than one I_{sat}.

3.2.7 Infrared - Out of sight

All the lasers described above are used to drive atoms based on radiation pressure, i.e. absorption and emission of photons. Another way of light interaction is through the induced dipole on atoms by light generating an alignment of these dipoles with the laser field. This effect is more important for light with far resonant light, the case of our 1064 nm laser.

From now on we will call this laser Mephisto. It is also a commercial laser from Coherent specified to produce up to 25 W of light. Internally, this laser is composed of a master laser diode with 1.15 W of 1064 nm and good spectral purity followed by several amplification stages using the MOPA scheme. In the figure 16 one can see the laser open with the Master Oscillator (MO) and the two Power Amplifier (PA) stages.

Through this doctorate, the total power of Mephisto has decreased by a considerable amount. This loss of power is expected through the degradation of the diode used in the amplification stage. The total power after an optical insulator installed at the output of the laser is 9.8 W, compared with the initial 14 W a few years ago. This imposes some limitations on the Optical Dipole Trap (ODT) depth, limiting the maximum achievable OD and spatial density.

After the output, the total power is split into two beams responsible for the horizontal (ODT-H) and vertical (ODT-V) arms of ODT. After the division, each beam is sent through a different AOM allowing independent control of power using an RF attenuator before the RF amplifier that drives each AOM. We also choose opposite orders in each AOM, +1 for ODT-H and -1 for ODT-V. Since they are driven with the same frequency we can use this to avoid the interference effect of each beam. The resulting standing wave will oscillate at a frequency of 200 MHz, which will be average-out and not seen by the atoms' movement.

Figure 16 – Inside the Mephisto laser showing the Master Oscillator (MO) inside the yellow box, the Power Amplifier (PA) inside the blue box and the laser light path on dark red.

As will be described further, the final stage of redMOT produces a disk-shaped, or pancake-shaped cloud. To optimize the load of these atoms at ODT is important to have a good shape overlap between both traps (redMOT and ODT). For this the ODT-H is an elliptical beam, currently with 2.0 W of power and sizes at a focus of 241 μm and 17 μm. The vertical beam is responsible for increasing the confinement to reach the dense regime needed, it has circular geometry with a radius of 49 μm. Some pictures of the beam profile at the focus can be seen in figure 17.

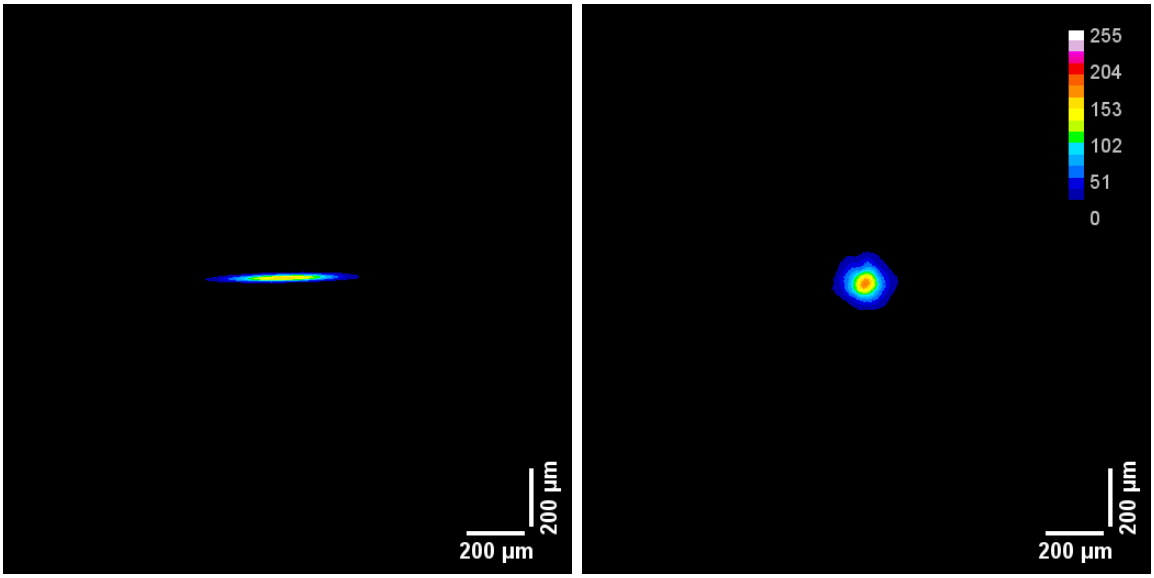

Figure 17 – ODT beams at focus. Left: ODT-H showing the elliptical shape of the beam. Right: ODT-V beam with circular geometry. The colors are a LookUp table representing the intensity given in an 8-bit scale.

3.3 Magnetic field control

The control of the magnetic field is essential in any atomic physics experiment. Although ^{88}Sr has zero angular momentum in the ground state, this is not true for the excited states, making the control over the magnetic field essential. Along the experimental sequence, a well-defined quantization direction is important for allowing access to specific projections. For the magneto-optical trap (MOT) for example, the magnetic field is essential for producing the restoring force responsible for the trapping part.

In the following subsection, we'll describe different experimental procedures for generating and controlling the magnetic field.

3.3.1 Zeeman slower magnetic field

As mentioned during the description of **blue** laser beams, the experiment starts with a Zeeman slower. From now it's enough to keep in mind that our source of atoms is an atomic oven that produces an atomic beam with typical velocities of 600 m/s. Usually, in an atomic beam, one of the directions has a larger velocity than the other two, this was even used in the first experiments where various properties could be measured using only the Doppler free transverse directions (Wu; Grove; Ezekiel, 1975). To start the deceleration of this atomic beam, to be further captured using the MOT, we use the Zeeman slower technique (Günter, 2004).

The idea of Zeeman slower is not new, however is still useful today, and recently got some renewed interest because of the possibility of decelerating molecules (Liang

et al., 2019). The key concept behind this technique is the use of a magnetic field for compensating the Doppler shift.

Once we have the atomic beam we could start the velocity reduction process using radiation pressure with a light beam propagating in the opposite direction of the atomic beam. However, as soon as the deceleration starts the atoms lose velocity and the laser beam becomes out of resonance, reducing the radiation pressure. To keep the atoms in resonance the idea is to use a magnetic field that varies along the atoms' trajectory, always compensating for the Doppler effect.

The atomic deceleration ($\vec{a}$), because of radiation pressure, is given by the scattering rate $\Gamma(s, \delta)$ time the velocity change due to the absorption of a single photon $\hbar\vec{k}/M$:

$$\vec{a} = \frac{\hbar\vec{k}}{M} \times \frac{\gamma}{2} \frac{s_0}{1 + s_0 + 2\Delta\gamma} \tag{3.3}$$

The magnetic field for the Zeeman slower in our experiment is generated with 6 coils with different numbers of turns and sizes, the resulting magnetic field can be seen in figure 18, on the right. It's important to guarantee the variation if the magnetic field doesn't pass the value of $\left|\frac{\mathrm{d}B(x)}{\mathrm{d}x}\right|_{max} = \frac{\hbar k a_{max}}{\mu v}$ (Günter, 2004), with $a_{max} = \frac{\hbar k \gamma}{2M}$ the maximum achievable acceleration. If this condition is satisfied, the atoms will follow the derivative of the field and decelerate continuously.

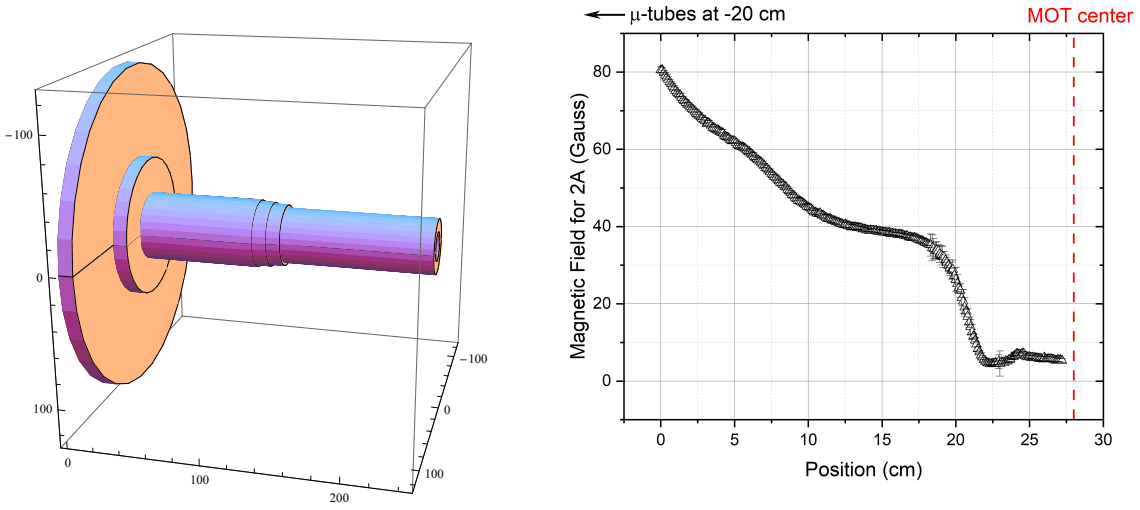

Figure 18 – Left: Drawing of the profile of the Zeeman coils. Right: Magnetic field profile when the Zeeman coils are operated with 2 A.

The light used in this case also needs to have a well-defined polarization. Because both projections of $J = 1$ ($m_J = \pm 1$) have opposite detunings, only one projection with be in resonance. Before entering the vacuum systems, we use a quarter-waveplate to circularize the light and adjust its position for a larger effect on the blueMOT number.

3.3.2 MOT coils

The MOT coils, as the name suggests, are the responsible for generating the magnetic field for the MOT. Two equal coils are set in an anti-Helmholtz configuration for generating a linear varying magnetic, with zero value in the center.

Because of the low separation of vertical windows in our experiment, we decided to produce the coils the small as possible to work at a low current and avoid the need for cooling. Another important constraint to be satisfied is to keep good optical access to the system. The final design was of conical coils with 95 turns in total.

For the fabrication we first produced, at the mechanical workshop, a mold to wrap the coils. To increase the heat dissipation efficiency, as we wrapped the coils, the multiple turns were glued together using a specific epoxy glue with good thermal conductivity (Duralco 132-1). For the coils, we used a cooper wire with diameter 1.45 mm.

The final produced coils can be seen in figure 19, together with the characterized magnetic field for 1 A. We measured the magnetic field for each point using a Hall probe. The position of the hall probe was varied using a linear translation stage and the gradient at the center can be extracted using a linear fitting of the data around the center values. We obtained a gradient of (-13.75 ± 0.08) Gauss/cm/A, so for a current of around 4 A we obtain a gradient of 55 Gauss/cm, a typical value used for producing a MOT on blue transition.

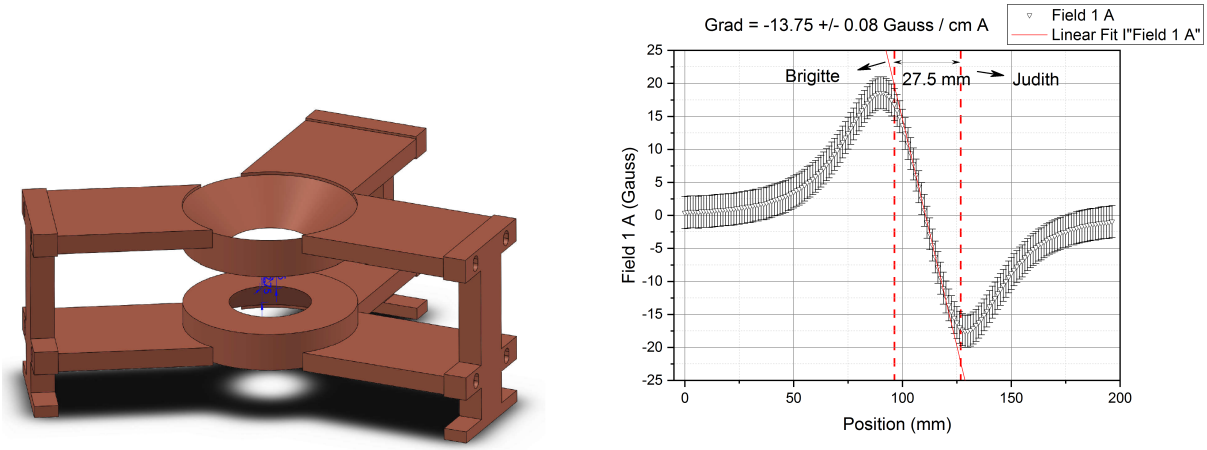

Figure 19 – Left: drawing of the two coils, plus the copper holders designed to hold them and to conduct the excess heat to the optical table. Right: Measurement of the magnetic field caused by both coils at their axis, for a current of 1 A.

The measurement above was done with the coils outside the optical chamber. For mounting the coils in the optical chamber we designed a pair of 3 copper holders which also are responsible for removing part of the coils heating. In the end, we characterized the coils' temperature vs. current, and the results show a limit of 5 A for keeping the

coils temperature below 60 ºC. In this way, we produced coils that generate the desired gradient without the need for additional cooling.

3.3.3 Compensation coils

The compensation coils are a set of 3 pairs of coils in each direction of space. Each pair is equal, with current flowing at the same orientation, in order to generate a homogeneous magnetic field at the center of the science chamber. Each pair of coils is oriented in one direction of space. The resulting magnetic field for each direction is:

- X = $(1.04 \pm 0.02)\ \frac{Gauss}{A}$.
- Y = $(0.66 \pm 0.02)\frac{Gauss}{A}$.
- Z = $(1.77 \pm 0.01)\frac{Gauss}{A}$.

These systems of coils have two roles in our experiment:

- Compensate stray fields + Earth magnetic field;
- Produce a constant field in the Z-direction to compress the cloud.

For experiments where there is a hyperfine structure, one may use RF spectroscopy to drive the atoms through different m_F projections and use this effect to compensate for the magnetic field, producing a null magnetic field at the atoms' location. For ^{88}Sr , this structure is absent and we need to develop another spectroscopy method for measuring the resulting field.

We managed to find a good compensation method for the magnetic field using optical molasses on the intercombination line. The magnetic constant for $^1S_0 \rightarrow {}^3P_1$ transition is 2.1 MHz/Gauss, for a linewidth of 7.4 kHZ, a small magnetic field of 4 mGauss is already enough to separate the fine structure by Γ. However, for our cloud of roughly 1 μK the Doppler broadening is 40 kHZ, giving a maximum resolution for our magnetic field stabilization of 20 mGauss.

For compensating we start by doing molasses at different resonances, when the frequency is resonant with a transition the effect of the cooling is more evident and we notice a reduction in the cloud size after 24 ms of molasses. In figure 20 one may see the effect of all 3 projections of J. The effect of the molasses for each transition is a dispersive curve, so for each m_J this results in three dispersive curves (figure 20 (a)). As we scan the magnetic field we see the curves moving until the moment all of them collapse in the central one (figure 20 (b)). Also, the molasses efficiency is larger for the condition of $\vec{B} = 0$, which means the cooling and heating effect is also better (figure 20 (c)).

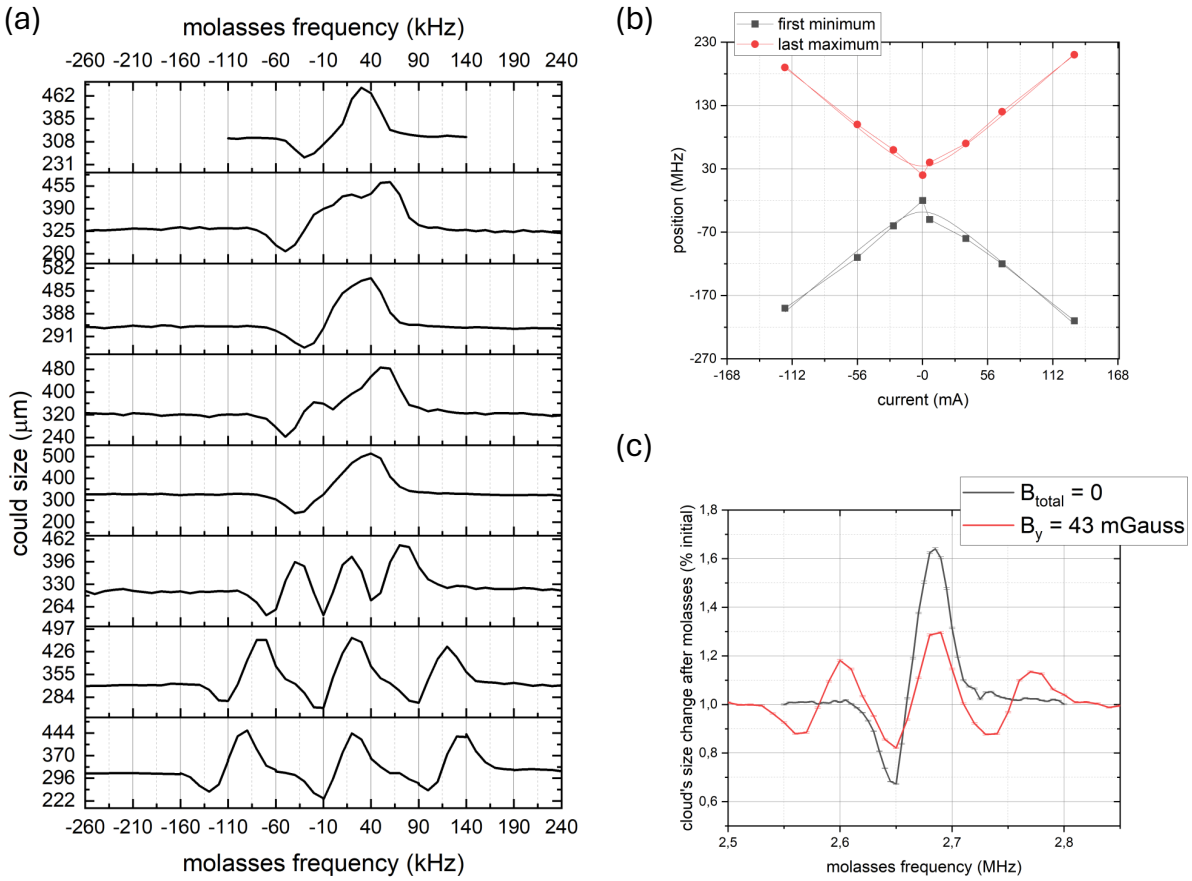

Figure 20 – Magnetic field cancelation procedure. (a) multiple spectra for different total field conditions, one may see the three dispersive curves collapsing in one. (b) monitoring the position of the first minimum and the last maximum we may plot and fit hyperbole to extract the minimum distance value. (c) comparing the molasses effect in two different conditions, for a null total field the effect is much stronger and decreases the cloud's size by almost 40%.

Because of the Doppler's effect, the temperature reduction doesn't happen at the same frequency for different directions. As the cloud falls and gains velocity we can see the effect on the vertical direction before the effect on the horizontal. Still, this is not a problem, and only the size after molasses in the horizontal plane (figure 20 is considered for magnetic field compensation. The value for compensating the magnetic field needs to be checked and adjusted daily, usually, it changes by a few mGauss.

The Z-direction coils have a circuit allowing for the adjustment of current in real-time, which is a class-AB amplifier adjusted to produce 100 mA/V. This circuit is important for adjusting the magnetic field only in the Z-direction during a compression stage to increase the number of atoms loaded in the optical trap.

3.4 Vacuum systems - Where science happens

The vacuum system is the core of an atomic physics experiment, since it's inside it that all the science happens. Our system can be seen in figure 21 and is composed of two sections:

- Oven section;
- Science chamber section.

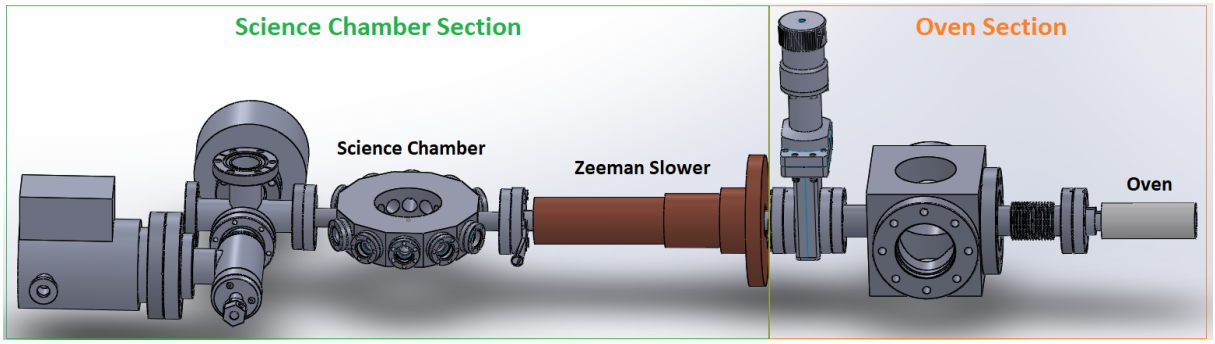

Figure 21 – Drawing of our vacuum system, showing the oven section and the science chamber.

The connection between both sections is done with the help of a differential pressure tube. This is a thin tube with 4 mm of diameter and 60 cm of length. For these values, this tube can hold a pressure difference up to 10^{-2} mbar. This is due to the unlikeness of a random vapor particle to have velocity in the specified direction for crossing the tube. In the following, we'll describe each section in detail highlighting the most important characteristics of each.

3.4.1 Oven section

The oven is our source of atoms. It was fabricated here at our mechanical workshop in Inox. The geometry of it can be seen in figure 22, where the two cuts are used to roll the heating resistances.

Inside it is divided into two chambers connected by a hollow screw. The metallic pieces of strontium are fitted inside the deeper chamber, while at the center of the screw, we fit a few hundred of μ-tubes. The idea behind these μ-tubes is once the Strontium is heated up to 600 ^{o}C, the metallic pieces will be filled with an atomic vapor with velocities at all directions. The μ-tubes serve to select only the atoms with velocity at some specific direction creating an atomic beam that is our initial source of atoms. This set of μ-tubes was recently exchanged to wider ones with 300 μm of internal diameter, 500 μm of external

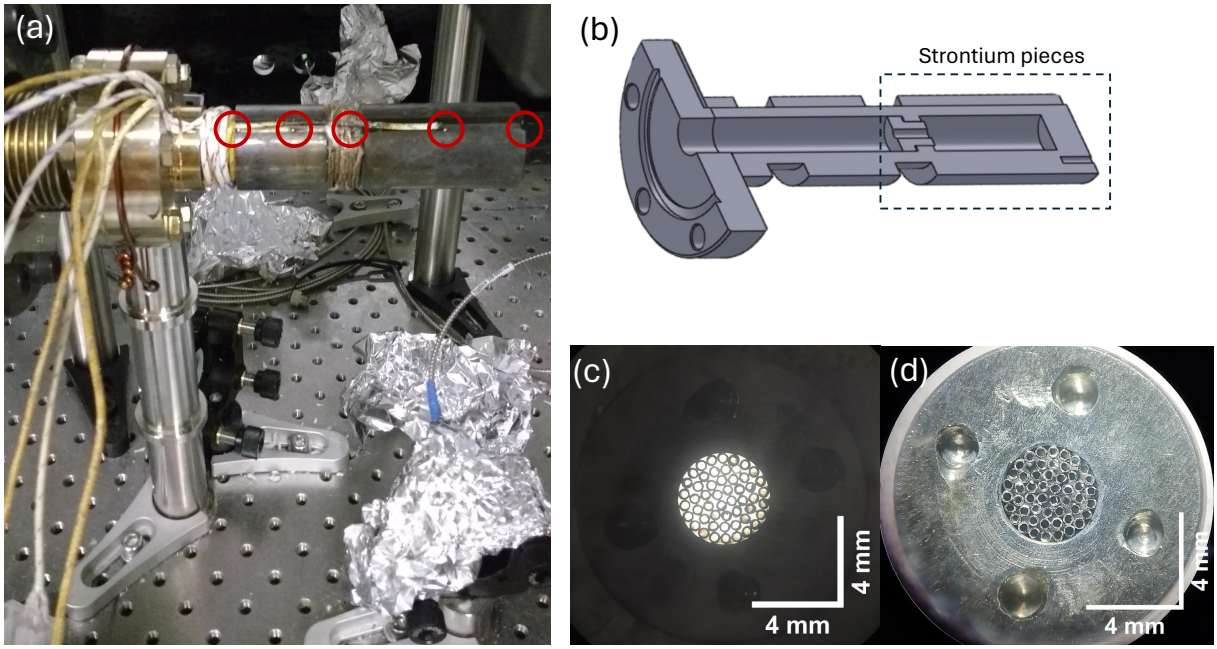

Figure 22 – (a) Picture of the oven, showing the different points where the temperature is measured. (b) Drawing of the oven. (c) Picture of the array of mirotubes at the exit of the oven, with backillumination. (d) Same as (c), with front illumination.

diameter and 8 mm length. In total we managed to fit 51 µ-tubes inside the 4 mm diameter hole, check the picture 23:

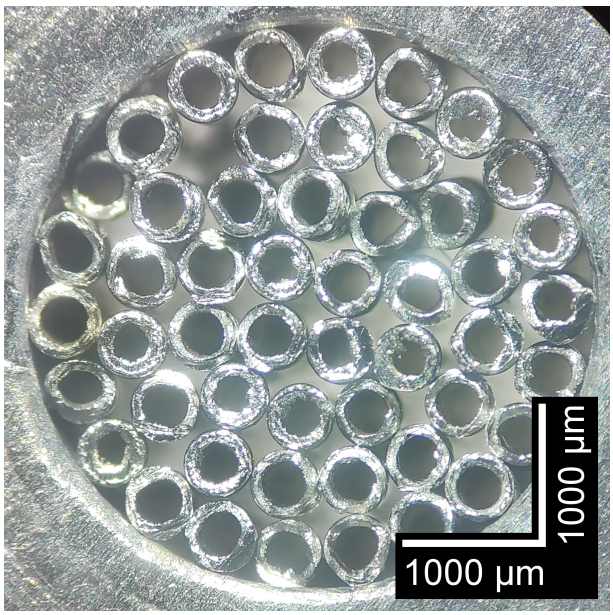

Figure 23 – Close-up of µ-tubes arranged.

To avoid the µ-tubes from clogging we always have them with a temperature higher

than the remaining parts of the oven. The temperature in the oven is constantly measured in 4 different points plus a temperature measured at the flange that connects the oven to the whole vacuum system.

Table 2 – Temperature of the oven, see the thermocouple locations in figure 22

Measurement	Temperature On (ºC)	Temperature off (ºC)
flange	330	199
front	482	289
μ-tubes	516	320
Oven	500	315
back	502	310

Source: From the author.

The temperature of the oven is constantly monitored using an Arduino that measures temperatures in several points around the room and loads the resulting values in the cloud using ThingSpeak. The oven is turned on and off automatically using relays connected to a digital timer. Given the typical turning-on time of 43 min(check the figure 24), the timer is programmed at 6 AM to 9 PM during working days, however, for most measurements present in the following chapter, we also took data overnight.

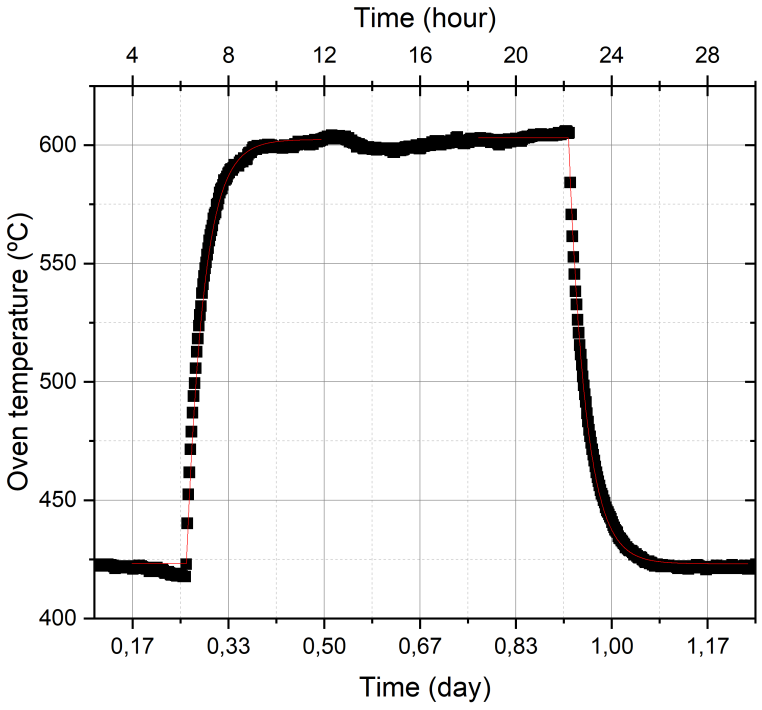

Figure 24 – Temperature of the oven during a 24h operating cycle.

For filling the oven one may use the valve connecting both sections to protect the vacuum inside the Science chamber. After breaking the vacuum and removing the oven we load few pieces of metallic Strontium inside it. The source of metallic strontium is a huge block of strontium immerse in paraffin oil, to avoid oxidation. Once we break some pieces we just remove the paraffin using Hexan, and fastly load them in the oven to avoid contact with oxygen and water in the air. Typically, each filling is enough for 1-2 years of oven operation before we have to fill it again.

Because of the high operation temperature, it's normal for the resistance wrapped around the oven to break when removed, so we decided to use tempo-couple wires as heating resistances since they are cheap and have some considerable electrical resistance of 14 Ω at 25 ^{o}C, but this resistance grows up to 18 Ω in normal oven operation values. They can also be easily wrapped around grooves showed in figure 22 (b)

We produced an article with some characterization of the atomic flux generated by the oven (Dias *et al.*, 2021). The data in this article were collected before the change of μ-tubes, but for the previous version with narrow μ-tubes, we found the atomic beam divergence to be equal to 13 degrees.

The pressure inside the oven chamber is 1.8×10^{-8} mbar, maintained using an Ion-pump model VacIon Plus 40 - diode. With the oven off, we noticed a small reduction of the pressure to 1.2×10^{-8} mbar. We also have installed a pressure gauge model IKR 050 from Pfeiffer Vacuum reporting 2.4×10^{-8} mbar and 2.0×10^{-8} mbar, with the oven on and off respectively.

Table 3 – Resistances used for heating the oven

Resistance	Voltage (V)	Current (A)	Power (W)
μ-tubes	29.6 (AC)	1.63 (AC)	48.2
Front	25.0	1.486	37.2
Oven	18.5	1.5	27.8

Source: From the author.

Despite the two before mentioned resistances, there is a third one used for heating. In total, we are dissipating 113 W of power to heat up the oven (see the table 3 for the values). To avoid all this thermal energy to escape we covered the oven in a few layers. First, there is a ceramic cylinder, covered in glass wool and finally wrapped with fiberglass cloth. To protect us from all these glass pieces, this whole insulation package is covered in aluminum foil.

3.4.2 Science chamber section

The second vacuum region is the one corresponding to the science chamber, with pressure equal to 1.2×10^{-9} mbar maintained with a VacIon Plus 40 - StarCell ion pump, controlled using a MidiVac controller model 929-5002. We also monitored the pressure of this region using a pressure Gauge. However, because they are located in different regions, the pressure measurement slightly differs with the Gauge registering 2.6×10^{-9} mbar.

This region also holds the entrance window for the Zeeman Slower beam. This is a Sapphire window that can be heated up to 500 ºC. This window is the one opposite to the atomic beam, so it needs to be heated to avoid atoms adhering to the surface and clogging the window. For heating, we cover it with fiberglass and using a resistance dissipating 83 W (156 V and 0.53 A) we achieve up to 300 ºC at the window.

Our science chamber is a dodecagon (see figure 25), with two vertical windows. It was fabricated with the vertical windows receiving a special anti-reflection coating with 3 central wavelengths: 461 nm, 689 nm, and 1064 nm. For the last one, the coating was also designed to withstand high-power laser light. This window was designed to allow great optical access through the vertical windows, which explains the choice for the conical-shaped MOT coils that still maximize the optical access.

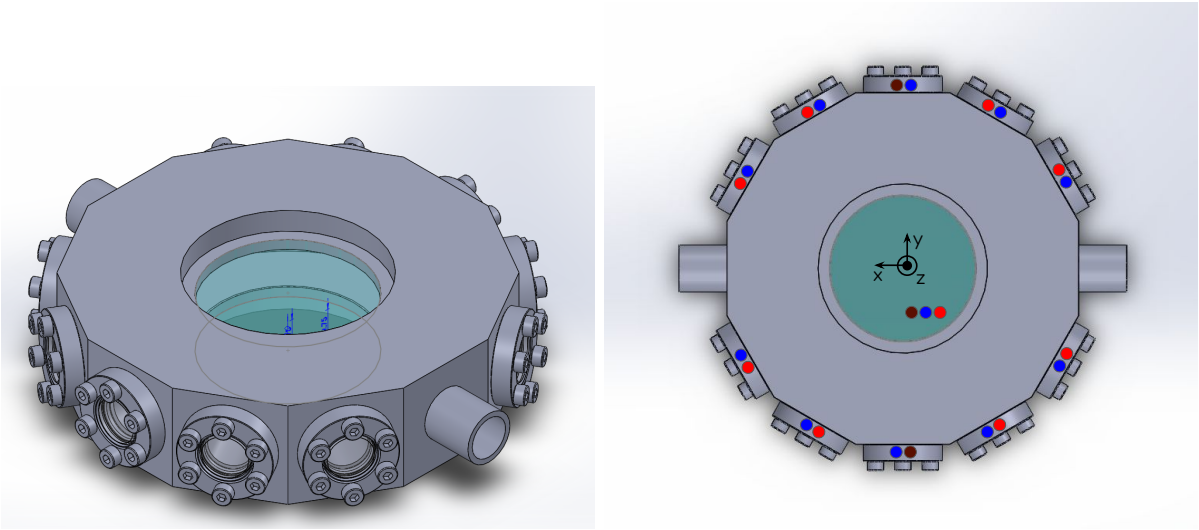

Figure 25 – Drawing of the science chamber. The colored circles represents the AR-coatings for different wavelengths.

The horizontal windows were selected between two coating options available: AR-coating for 461 nm and 689 nm, or 461 nm and 1064 nm. In the figure 25 one may check the final configuration. The dots in the windows represent the AR-coating wavelength.

3.5 Producing the cloud

3.5.1 Controlling the machine

In our experiment, there are a few steps to be followed for the production of the atomic cloud This means different cooling stages from the capture of atoms from the oven to be loaded in the final trap, where we can take measurements.

There are several time scales to be considered, so if we discuss a few of them, the need for precise time control becomes explicit. One time scale is the blueMOT loading time, from the moment we start capturing atoms to reach the stationary limit, which is typically on the order of seconds.

Another important time scale is the typical time for cloud expansion. We may define this as the time it takes for the cloud to double its size. However, one needs to consider the different temperatures we may have. Assuming for example the Doppler temperature for blueMOT and redMOT, this gives 700 μK for blueMOT and 400 nK for redMOT. At these temperatures, assuming the size of 1 mm for blueMOT and 200 μm for redMOT, we have 4 ms and 30 ms, respectively. The last time scale to be discussed is the trap oscillation of atoms in the ODT. Our ODT frequencies are 500 Hz and 250 Hz. In this way, a full period of oscillation is 2 ms and 4 ms. In both cases discussed before, expansion and oscillation times should be understood as an upper limit, since we need to resolve a fraction of these times to properly monitor the size of the cloud and its center of mass position.

Beyond the natural time scales discussed above, for imaging the time we need to be able to do pulses of light is as short as 20 μs to avoid saturating our cameras.

With all this said, is necessary μs precision for controlling the experiments. For this, we use control boards for National Instrument (NI) by generating the multiple signals used in the experiment.

Currently, we have two boards focused on generating different types of signals. They are NI-6259 and NI-6723. The first one has 32 digital output channels that produce either 0 or 5 V as output, and 4 analogical channels to produce signals between -10 V and 10 V. The NI-6259 board is the fastest one with a sample rate of 1MHz. The second is slower but very useful for producing analogical waves going from -10 V to 10 V, with its 32 analog output channels, so it is used with equipment that requires continuous control. It has a sample rate of 800 kHZ and 16-bit of depth for digital to analogical conversion. To use the most of it, if a signal from 0 to 1 V is necessary, we choose to produce a simple circuit that divides the output by 10 in other to have more resolution in the voltage selection.

For connecting the boards to the signals in the experiment we developed some buffers and protection to ensure the boards inside the computer won't be damaged. The

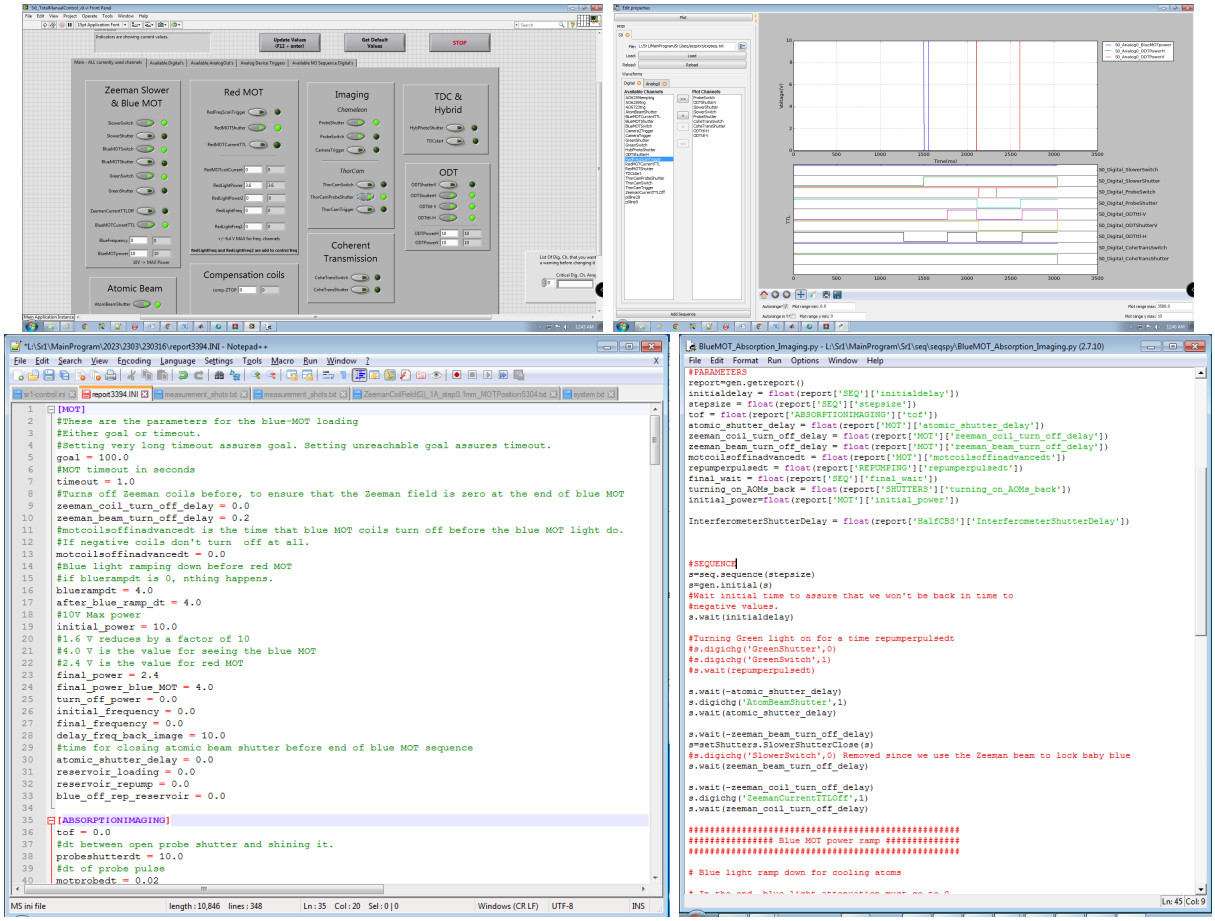

Figure 26 – Screen captures of the old version of the control program.

connection of these boards inside the computer is done with the use of PCI connection.

3.5.2 A new control program – An important upgrade

The previous program for writing the experimental sequences and communicating with the NI boards was a hybrid between Python and LabView, where the experimental sequences were written in Python while the communication with NI boards was done in LabView. A lot of good practices were implemented on these programs, internally developed in our group, like the ability to control and program multiple signals independently, the possibility of reusing "blocks" of sequence among different experiments, and the possibility of sequence viewer with the multiple channels in time synchrony.

The biggest drawbacks were: the board's programming and execution time and the absence of signals measurements during the sequence execution. Mostly to increase the repetition rate we decided to change our control program to labscript (Garcia *et al.*, 2019).

Labscript suite is a framework of control and analyses programs developed to control time-precisely experiments by P. T. Starkey at Monash University. This framework has implemented a pseudo-clock scheme which enables a strong reduction of the programming

and execution time.

In these experiments, a clock is a device that synchronizes different equipment but also dictates the execution rhythm at which they should be executed. In our previous version, the clock was configured to 1 MHz, which means that a new instruction needs to be sent to the boards every clock time (2 μs), so if a sequence has 4 s around 2 mi instructions need to be sent and executed. An instruction is the state of every output in the board, so an output for all 68 channels available, clearly this is a HUGE file. It's important to note that many of these instructions are repeated since usually, no change is necessary at the clock time scale, with a few exceptions.

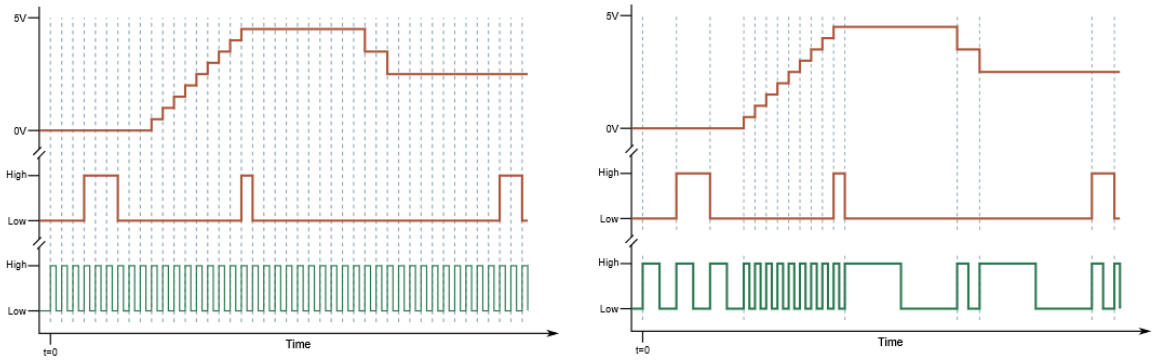

Figure 27 – Left: Clock operation for the old Labview control program. The clock (red line) ticks every resolution time, regardless of having a change or not on the control channels (red lines). Right: Clock operation for the new Labscript control program. The clock (red line) ticks only when at least one control channel (red lines) needs to be updated.

In the pseudo-clock scheme, a third device has an internal clock at 1 MHz, as the normal clock. However, it reduces the number of instructions needed by using a frequency-variable clock to control the other equipment by updating the instructions only if the configuration changes. This reduces the amount of data that needs to be loaded at the board, decreasing the time between sequences. We decided to use prawblaster as a pseudo-clock since it was a cheap solution already implemented at LabScript.

With the previous program, our total execution time was around 8-9 seconds, for an actual 2 s sequence, takes 6-7 s to load all the configurations in the NI board's memory. With LabScript we managed to reduce the whole sequence and programming time to 2 s. Comparing the time between sequences when running it continuously, it takes 300 ms. With this upgrade, we increase the repetition rate by a factor of almost 4!

Another important feature added was the possibility of using not only the outputs but also the inputs of NI-boards for taking measurements. We can now monitor different beam powers using photodetectors installed at various points, like blueMOT fiber power,

ODT-H and ODT-V fibers power. More details about LabScript can be found at the website https://labscriptsuite.org/en/latest/.

Although it should be simple, we couldn't include our cameras in LabScript, so we decided to keep using our previous Matlab program to communicate with them. In this way, this Matlab program prepares the cameras in some pre-defined configuration of shutter speed, gain, image depth, and other parameters, and waits for the hardware trigger produced by the NI-boards. Once we receive the trigger one image per trigger is captured and transmitted to the computer, where it is saved in the folder for the day.

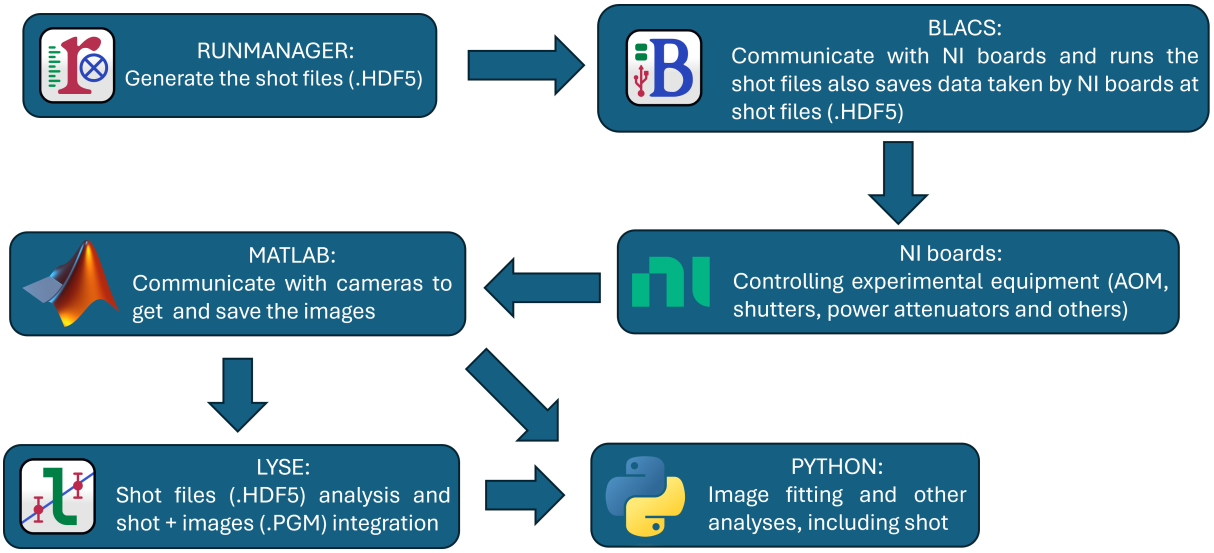

Figure 28 – Overall map for the experimental sequence: The shot files, produced by RUNMANAGER, contain all the experimental sequence information. For every experiment run a shot file is produced. These shot files are sent to BLACS which is responsible for queuing and running them through communication with NI boards. Generally, one atomic image is produced in every experimental sequence for monitoring the cloud's size, temperature, and number of atoms, for capturing this image the cameras are triggered using the NI boards, and this information is transferred to a MATLAB program that gets and saves these images. Finally, this imaging may or may not be integrated in the shot file to be later analyzed using a Python script.

3.5.3 Imaging the cloud

Overall all the imaging systems work based on the idea of using three images, which may be absorptive or dispersive imaging systems. For the absorptive we can take images on the horizontal (Y-axis in figure 25) and vertical (Z-axis in figure 25), while for the dispersive imaging system, we can only take vertical images. The idea of three images is to have information about the atoms, the beam used to interact with them, and the background, more details in the following:

- First image: This is the one that interacts with atoms and has the atomic information, for the absorptive the information is the shadow cast on the laser beam. For the dispersive system the information is in the phase of the wavefront, but this phase profile is transformed in an interference pattern. This image is usually called **atoms**.
- Second image: This is the image of the beam itself without atomic information. It is used for normalization purposes, and its called **probe**.
- Third image: This is a **dark** imaging, without the probe beam to remove the spurious information from undesired sources like other laser beams, light from room lamps, camera noises, and others.

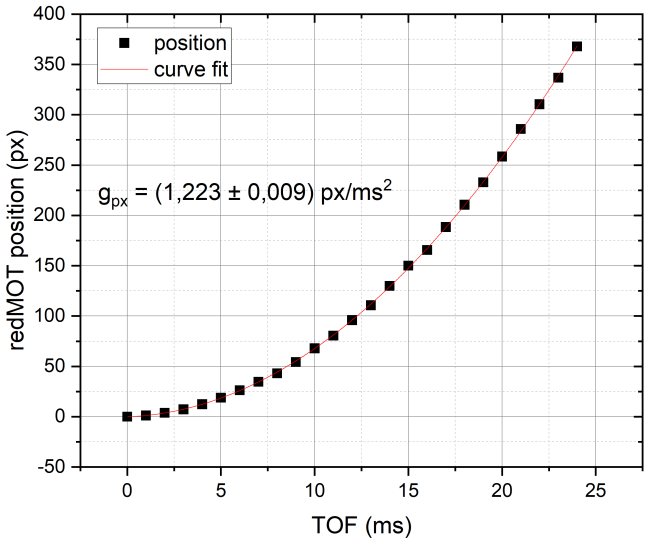

Figure 29 – redMOT vertical position, in camera pixels, as a function of the time of flight before the imaging. By fitting a quadratic behavior and comparing to the expected acelaration of gravity, we find the magnification of the horizontal imaging system.

As mentioned before, we have two imaging systems, one horizontal and one vertical. For the horizontal imaging system, the camera we used is a Chameleon2 from PointGrey model Chameleon CMLN-13S2M, with 1296×964 pixels, each with a size of 3.75 µm. For the vertical imaging system, we have a cMOS Thorlabs camera model CS2100M-USB with 1920×1080 pixels, each with 5.04 µm.

The horizontal imaging system has a (de)magnification equal to $M_{hor} = (0.472 \pm 0.003)$. Since the blueMOT is quite big with 1 mm of diameter, we decrease the imaging size for the blueMOT to fit on the camera, producing an effective pixel size at the atoms of 7.94µm. This magnification is done using a set of two lenses with focus of 150 mm and 75

mm. The way of measuring the magnification of this imaging system is quite interesting and deserves some attention: we use the free-falling atomic cloud to estimate the magnification. We release the cloud and record its position while varying the time-of-flight (TOF). After recording its position for various TOF we may plot this curve and fit with the following expression (see figure 29):

$$z(t) = z_0 + v_0 t + \frac{g_{px} t^2}{2}. \tag{3.4}$$

The obtained value for g_{px} is related to the gravity acceleration g through: $g \times M_{hor} = g_{px} \times CCD_{pixel}$, where CCD_{pixel} is the camera pixel size, and M_{hor} is the magnification we want to find.

For the Chameleon camera, the interval between images has a minimum of 250 ms, corresponding to the necessary time for data transmission of the whole image, we may decrease this time doing a region-of-interest (ROI) on camera.

The vertical imaging system has a bigger magnification of $M_{ver} = 3.57$ since this system is designed to measure the atoms at ODT, with a typical size of 10 µm. This magnification is produced using two lenses of focal length 150 mm and 500 mm. In this case, the effective pixel size is 1.41 µm.

The magnification of this vertical imaging system was measured by displacing the cloud using the compensating coils on the X-direction. Since this axis is shared on both imaging systems, it's possible to obtain the magnification of the vertical imaging system in terms of the horizontal one.

Another particularity of the vertical imaging system is the SLM at the focus of the first lens, and it can be seen in figure 30.

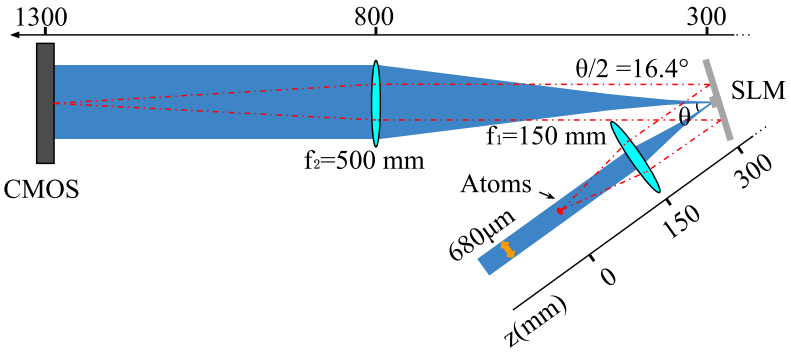

Figure 30 – Optical scheme of the vertical imaging system showing the SLM at the light path to perform phase contrast imaging of the atomic cloud.

This SLM is used as a phase mask to do Phase Contrast Imaging (PCI). This is a special imaging method, most common for people working with Bose-Einstein Condensates (BECs) since it is a non-destructive method, allowing one to probe the dynamics in an atomic cloud without perturbing it (Meppelink *et al.*, 2010), but also makes it possible to

probe high optically dense clouds, the main reason behind our implementation. It works by measuring the phase shift at the wavefront created by the atoms. However, since it's non-resonant light, it provide negligible radiation pressure on atoms.

Since the SLM allows us to change arbitrary the phase masks we use, we can use this imaging system for absorption imaging (AI), using no phase mask, and Phase-Contrast Imaging, using the phase mask as described in (Fernandez *et al.*, 2025).

3.5.4 blueMOT and redMOT

Magneto-optical traps (Raab *et al.*, 1987) are a class of non-conservative traps with constant in-flux and out-flux of atoms. Moreover, as one atom is captured by the trap, its temperature decreases until the limit given by the Doppler temperature, or other experimental limitations. Once trapped, the atoms are subjected to collisions that may expel it from the trap. In this way, the equilibrium number of atoms is given by the ratio of in-flux over the losses.

The important constants for modeling the MOT are the loading flux given by α and the loss rate given by β. While the flux of atoms is given by a combination of oven and Zeeman slower, the losses of atoms are usually proportional to the total number. The differential equation describing this process is:

$$\frac{\mathrm{d}}{\mathrm{d}t}N = \alpha - \beta N, \tag{3.5}$$

where N is the atoms number. After integrating this curve and assuming the initial number of atoms in the MOT is zero, we find:

$$N(t) = \frac{\alpha}{\beta}(1 - \exp(-\beta t)). \tag{3.6}$$

We use this equation to fit the blueMOT loading curve, and, we found the coefficients to be $\alpha = (45 \pm 2)$mi atoms/s, and $\beta = (1.6 \pm 0.1)$ 1/s. The data and the curve fit are available in figure 31.

The number of atoms at blueMOT varies over long periods (few months), as we constantly need to realign the beams or optimize other things, but on average it is between 30 mi - 50 mi of atoms.

We discussed quickly the Time-of-flight (TOF) technique for measuring the magnification of the imaging system. However, this is also how we determine the cloud temperature[1]. We turn off all the lights and the magnetic field for a time TOF and record the clouds' expansion as a function of this time.

[1] When working with atomic clouds, it is common to use the word **temperature** to describe the width of velocity distribution. Unlike the usual definition of temperature, and the concept of measuring it achieving thermal equilibrium of the probe with the bigger system, in our case we assume the cloud is "thermically" in equilibrium with the laser field. Some simulations shows that the spontaneous emission process ensures a Maxwell distribution for the velocities, making sense to define an associated temperature.

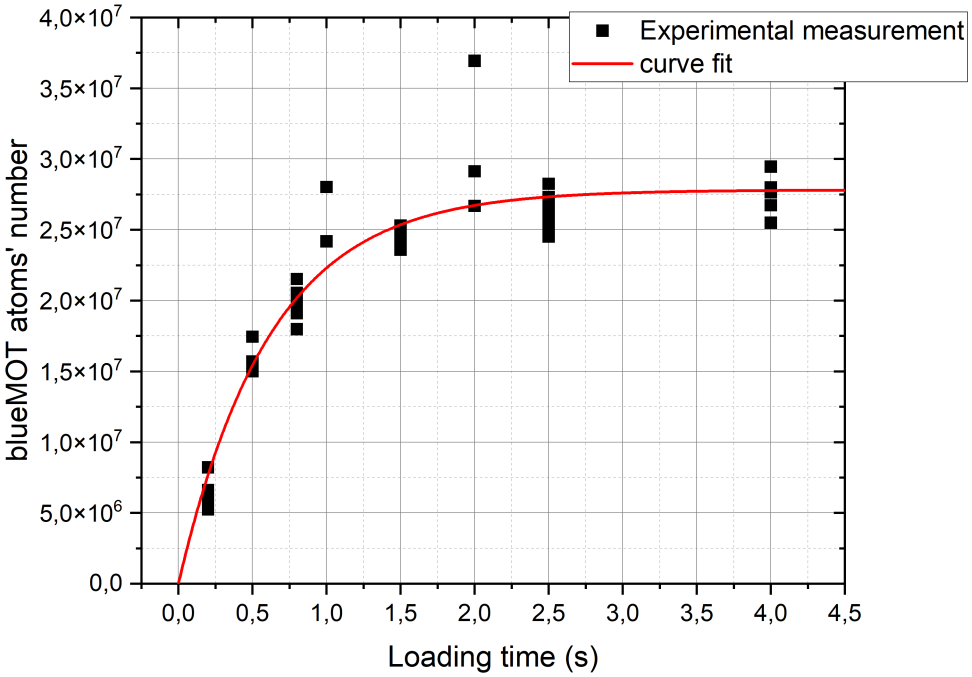

Figure 31 – Number of atoms at the BlueMOT versus loading time.

So, when we make TOF and take an image of the cloud we are probing the velocities distribution. The equation describing the cloud's size expansion in free evolution is the sum of two random variables: the initial cloud size (s_0) and the average velocity ($\bar{v}$). Using now the fact that the variance of this sum is equal to the sums of each variance since two variables are completely uncorrelated:

$$s(TOF) = \sqrt{s_0^2 + \bar{v}^2 TOF^2} = \sqrt{s_0^2 + \frac{k_B T}{m} TOF^2}, \tag{3.7}$$

where k_B is the Boltzmann's constant, $m = 87.90$ g/mol is the ^{88}Sr mass, T is the temperature and $\bar{v}$ is the Gaussian velocities width. For our blueMOT we may fit the expansion (see figure 32) and obtained $T_x = (7.8 \pm 0.5)$ mK and $T_y = (8.5 \pm 0.5)$ mK.

If TOF is long enough for $s(TOF) \gg s_0$, then one may just consider the final size of the cloud to estimate its temperature. For the blueMOT, because of its higher temperature, this is not possible. However, this works really well for the redMOT and ODT. In figure 33, we see in red points the estimated temperature of the redMOT considering only the final size, which approaches the value obtained from the fit (indicated in continuous red line).

As described in previous sections, we may characterize the MOT in terms of magnetic field, light intensity, light detuning, and others. However, our goal is to load as many atoms as possible in the ODT with the smallest temperature to increase the spatial

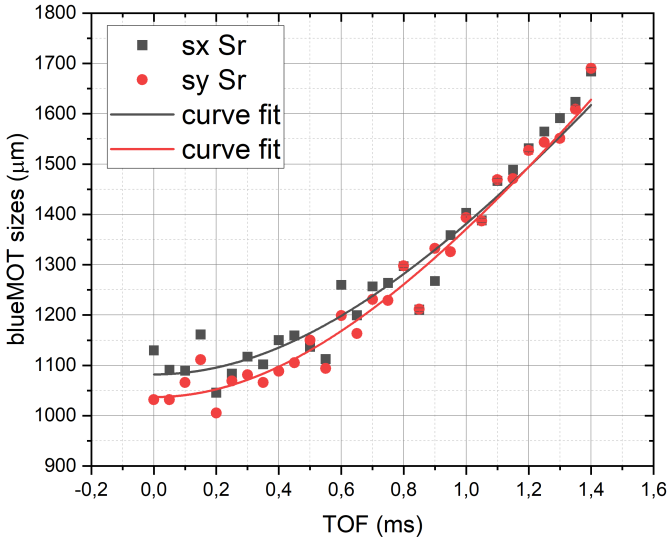

Figure 32 – Size of blueMOT as a function of the time-of-flight before the image, showing the thermal expansion of the free cloud.

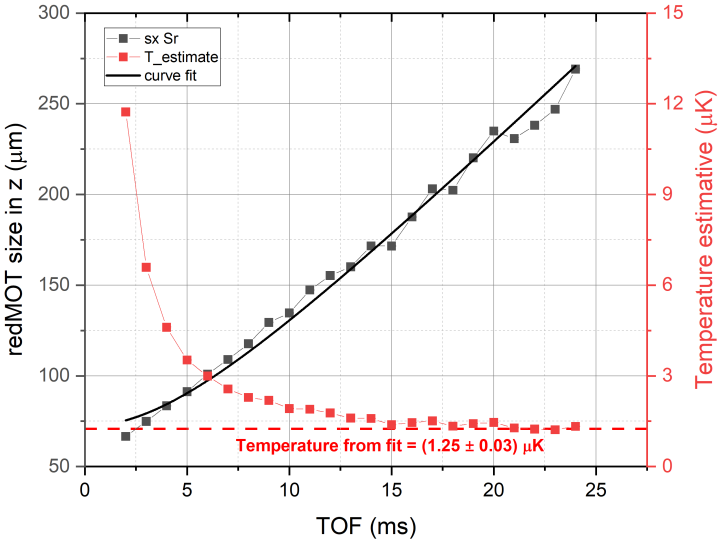

Figure 33 – Black squares, left y-axis: redMOT size as a function of its time-of-flight. Black, thick solid line: Fit of of the redMOT size with the expression 3.7. Red squares: Estimation of the temperature from the data shown in black squares, neglecting the cloud initial size, for different time-of-flight. Red dashed line: Temperature obtained from the fit shown by the black, thick solid line.

density. In this way, on the following we will present the optimum values for blueMOT and redMOT used for obtained the best ODT possible.

For the blueMOT, as mentioned before the number varies between 30 mi and 60 mi of atoms, while the temperature is between 2 mK and 6 mK. The final temperature depends on the light intensity. However, this parameter is varied in order to obtain the best transfer of atoms between blueMOT and redMOT.

The experimental sequence for the production of blueMOT is the following:

1. Load atoms from Zeeman Slower with blueMOT beams at maximum power, i.e. 1.8 I_{sat} at atoms during 1.2 s;
2. Execute a power ramp with duration 4 ms from 100% to 11% total power, for temperature reduction. The power decrease happens linearly in 4 ms and after there is 4 ms for thermalization at final power.

We may also check a characterization of the blueMOT temperature as a function of the final light intensity, available in figure 34 (please note that this graphic was done for alignment conditions different than the ones ultimately used for the blueMOT, and as such, the temperature of the blueMOT is smaller than what expected by this graphic). We note that the increase in the temperature is much bigger than expected, this may be caused by problems in alignment, as well as in the beam profile. Nonetheless, we reached the Doppler temperature for very low intensities.

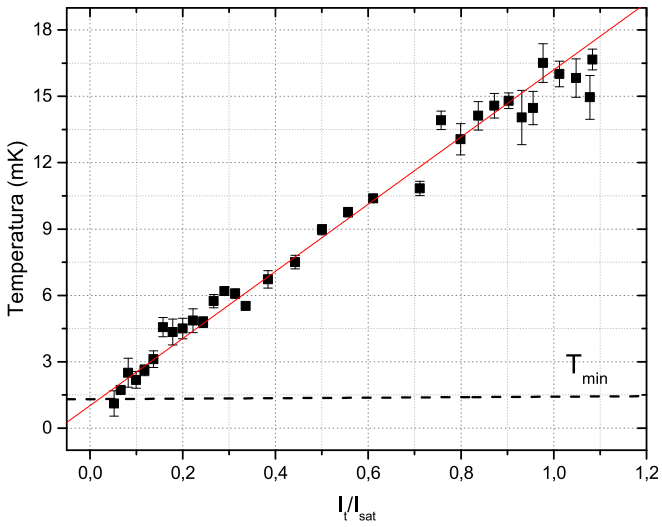

Figure 34 – BlueMOT temperature as a function of the total intensity of all 6 beams, normalized by the saturation intensity of the optical transition.

In the end, we may vary the TOF to probe the cloud, but usually we monitor the cloud with 1 ms of TOF. The obtained cloud is available in figure 35. It has 30 mi atoms with a size of 1 mm.

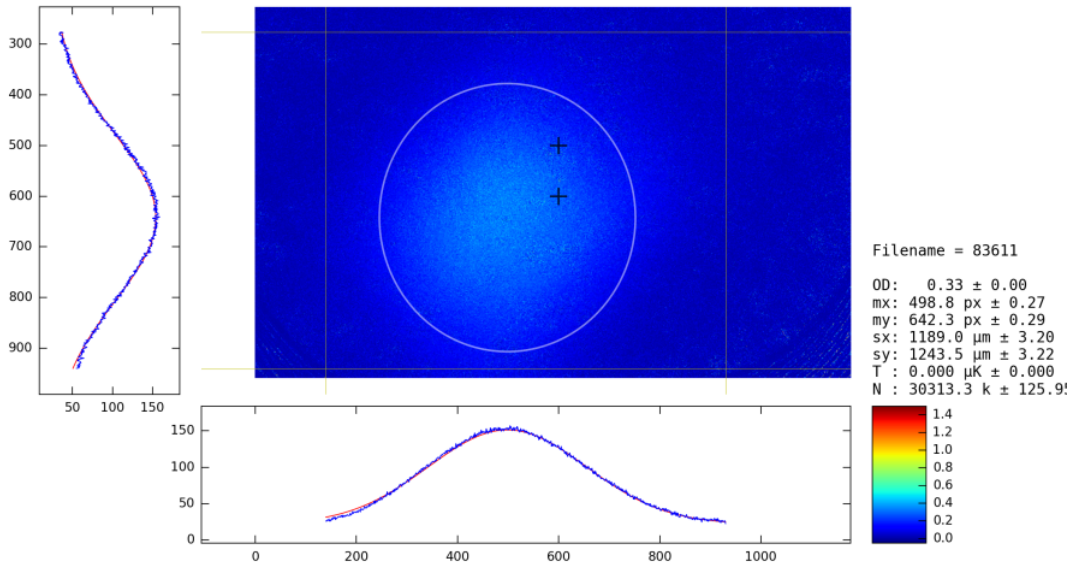

Figure 35 – Absorption image of the blueMOT after 1 ms of time-of-flight.

The blueMOT temperature also impacts the transference of atoms blueMOT → redMOT, so we select the value that maximizes the transference. In the end, the typical temperature for blueMOT is 4 mK, which means a Doppler broadening of 890 kHz for the 689 nm transition used to cool the atoms in the next cooling stage, the redMOT. Because this transition has a narrow width of 7.4 kHz, we need to artificially broaden it, to cover more velocities classes and capture more atoms.

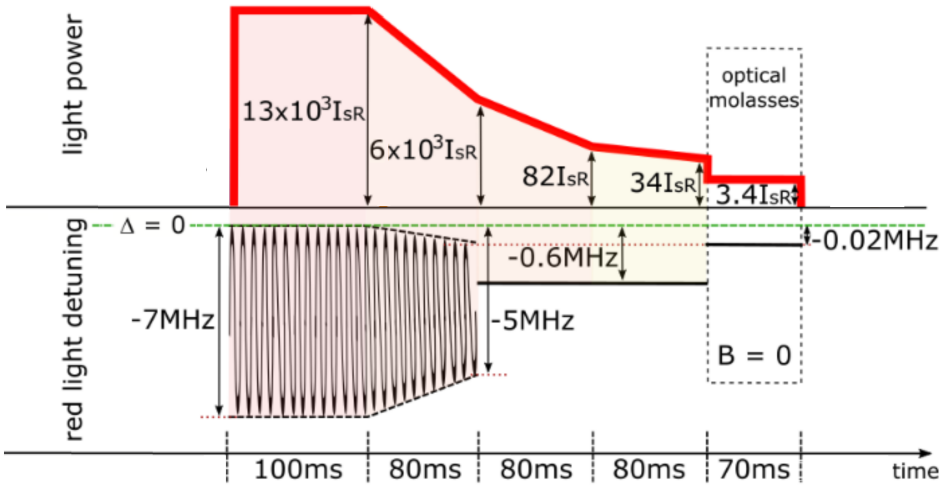

Figure 36 – Experimental sequence for producing the redMOT. We show here the total intensity in units of saturation intensity, and the detuning of the optical fields of the redMOT versus time.

The redMOT happens in three stages (figure 36). In the first one, we constantly scan the central frequency with a span of 7 MHz and the intensity is also constant at

$1.3.10^4$ I_{sR}, with $I_{sR} = 3.0$ μW/cm^2. In the second stage we continuously decrease the scan amplitude and light power amplitude from 7 MHz to 5 MHz, while the intensity decreases from $1.3.10^4$ I_{sR} to 6.10^3 I_{sR}. For both stages, we used a triangular waveform in the scan with a frequency of 35 kHz. In the third and last stage, the detuning is kept constant at -0.6 MHz, while we continuously decrease the power from 82 I_{sR} to 34 I_{sR}.

Because of the narrow transition, in the last stage the cloud is submitted to a "box" like potential, producing the characteristic pancake-shaped cloud to be loaded in the ODT. We typically have 15 mi of atoms at a temperature of 1.2 μK.

Before loading the atoms in the ODT we daily check for the magnetic field cancellation. As is going to be discussed further, one of ODT optimization steps is a molasses, during the ODT, using red transition. However, to ensure the molasses efficiency it is important for the total magnetic field to be zero.

The procedure is to make the molasses for 24 ms, with a light intensity of 3.4 I_{sR} for various frequencies. The molasses effect is bigger when it is closer to a transition, in this way we are doing an spectroscopy of the red transition. The molasses produce a dispersion like curve for the size of the atomic cloud, where the decrease of the size indicates cooling, while the increase indicates heating.

For values of magnetic field higher than a few mG, we may see three dispersive curves (see figure 37(a)). However as we adjust the magnetic field value, the curves collapse in one, as shown on Figure 37(b). For the correct values of the compensation coils, the distance between the minimum and the maximum is of 40 kHz. Also, when we have zero resulting magnetic field, the molasses effect is stronger and we see a reduction on the size of up to 43% for the Z-axis after time-of-flight, indicating a strong cooling effect.

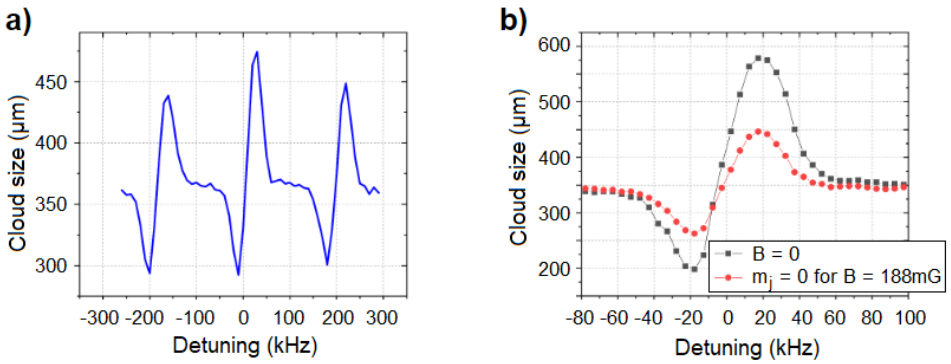

Figure 37 – Cloud size after time-of-flight, during which the atoms are exposed to the red molasses, as a function of the frequency of the molasses optical field. In (a) and for the red points in (b), there's an uniform magnetic field of 90 mG applied to the atoms, while the black points in (b) are for the magnetic field canceled to the mG level.

3.5.5 ODT – densifying the cloud

As described before, we choose the ODT beam geometry to maximize the transference from redMOT → ODT. For the current power of 2.0 W at ODT-H and 0.8 W at ODT-V, the total trap depth is 28 μK. However, because the gravity the trap depth is reduced as the gravitational potential adds another way for atoms to escape, resulting in an effective trap depth of 14 μK. This should be enough to hold redMOT cloud with a temperature of 1 μK. In the figure 38 there are two surface plots with perpendicular cuts showing the geometry of the ODT.

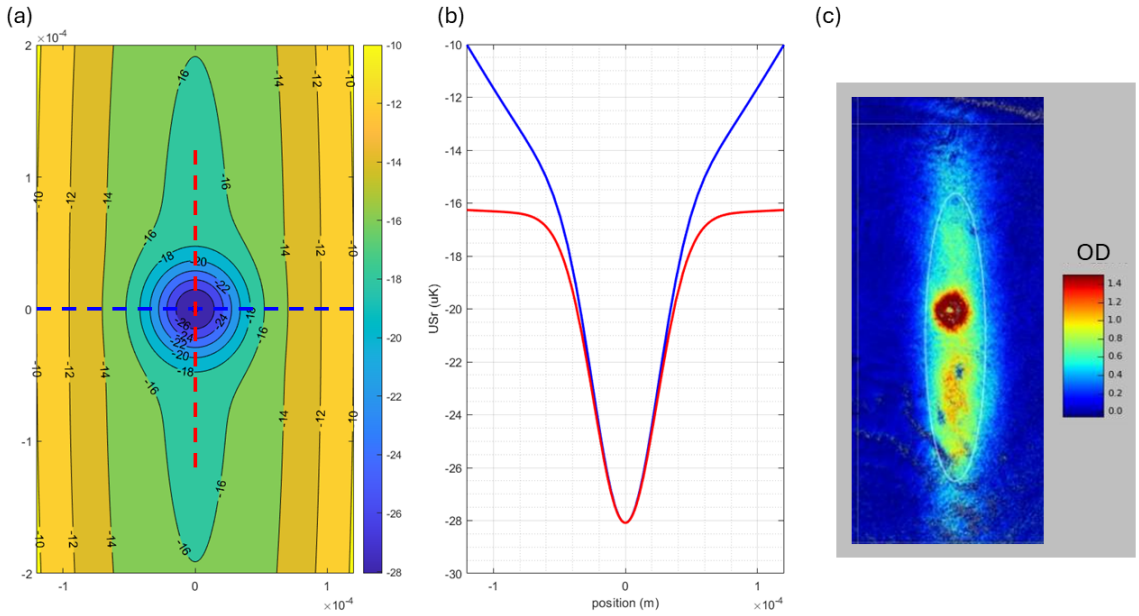

Figure 38 – (a) Potential energy 2D profile of the ODT in the horizontal plane, i.e., in the plane perpendicular to gravity. (b) Potential profile at the two directions, red and blue, indicated at figure (a). (c) Absorption imaging of the atoms trapped in the ODT, with no molasses applied. The central denser cloud is saturated, having an optical depth much higher than shown. We can also see atoms trapped in the shallower horizontal ODT beam. The small hole at the center is caused by the beam that probes the cloud transmission, that was turned on for alignment purposes.

The potential energy felt by the atoms at the ODT, plotted in figure 38, is given by the Stark shift of the ground state. For the presented calculation we include only transitions inside the singlet fold, since this will be the stronger effects.

As expected, the atoms acquire potential energy once they are loaded into an ODT, this was also reported in other experiments (Liao *et al.*, 2017) and led us to search for alternatives to increase the spatial density once the atoms are inside the ODT. The heating effect can also be seen on the high portion of atoms in the shallow part of ODT potential (see figure 38 (c)).

3.5.5.1 Compressing and cooling atoms at ODT

As discussed in (Loftus *et al.*, 2004) for MOT over narrow lines, in the limit where the detuning $\delta \gg \Gamma_{ef} = \Gamma\sqrt{1+s}$, the atomic cloud is formed dislocated to the center of the magnetic field, with the cloud radius inversely proportional to the detuning. We would like to use the cloud's size dependence with the light frequency as a tool to compress the cloud inside the ODT. The use of a compress phase is not new in the literature (Chalony *et al.*, 2011) but requires more details over the effect on a narrow transition. For example, in our experiment, this is only possible, as long as, we provide a way to keep the the center of mass at same position.

Our solution for this problem is, at the same time we scan light frequency and we scan the magnitude of a uniform magnetic field responsible for shifting the zero of the quadrupole field and keep the redMOT at same position with respect to the ODT. Using both effects we can compress the cloud with the ODT beam on to increase the loading inside the ODT as is visible in the figure 39.

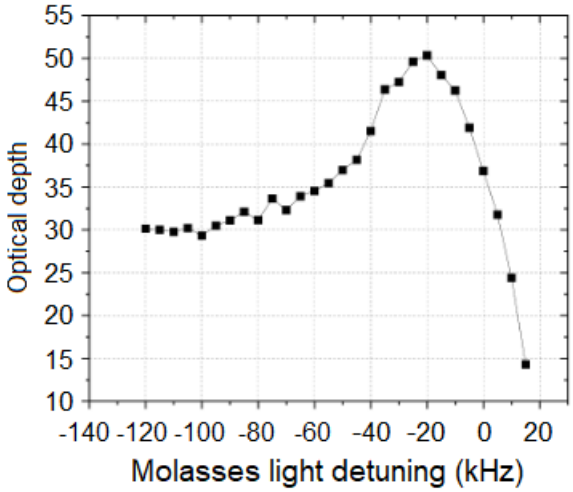

Figure 39 – Optical depth of the atomic cloud trapped in the ODT after the molasses stage, as a function of the detuning of the molasses. We see an increase of 60% in the optical depth, which is linked to a increase of nearly 60% in the atom number.

To increase even more the spatial density inside the ODT, we also produce a molasses to cool the atoms inside the optical dipole trap. For this, we apply a molasses with a detuning of -20kHz during 70 ms. The detuning was optimized experimentally, but we may understand it as the value for the detuning that cools mostly the atoms on the shallow part of the ODT.

In a similar manner, as was done for calculating the ODT potential, we may calculate the Stark effect felt by the atoms in the $^3P_1$ state. The difference of the Stark shift between the ground state ($^1S_0$) and the $^3P_1$ gives the differential Stark shift. This

value is proportional to the light intensity. We show in figure 40 the relative Stark shift for each one of the three transitions to the upper magnetic sublevels in the configuration that minimizes the overall Start shift felt by the atoms. This corresponds to the vertical ODT beam with circular polarization and the horizontal beam with linear polarization aligned with vertical beam propagation.

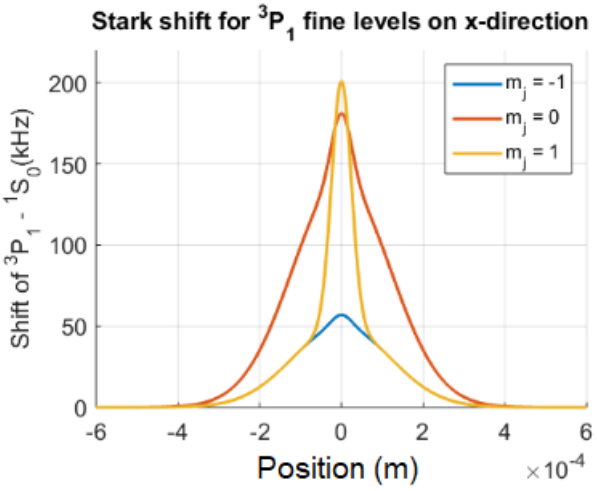

Figure 40 – Optical depth of the atomic cloud trapped in the ODT after the molasses stage, as a function of the detuning of the molasses. We see an increase of 60% in the optical depth, which is linked to a increase of nearly 60% in the atom number.

3.5.6 Imaging the atomic cloud

As mentioned before, for this images of very high OD (up to 50) absorption imaging is not possible, so we have the phase contrast imaging (PCI) system that allows very high OD images using light very far from resonance. As a general criterion, for imaging a cloud of optical depth of b_0 we need a detuning of the order of $b_0\Gamma$ (Fernandez *et al.*, 2025) and we can ignore the density effect for doing the PCI.

The interpretation of the image obtained, as well as the process for putting it in focus were not trivial. In the end we made a validation of this imaging system using the absorption imaging technique. For this we first imaging the cloud using the PCI and later made an absorption imaging for obtaining the atom number.

We show in figure 41 the optical depth measured *in-situ* with the PCI for different clouds, versus the reconstructed optical depth based on the measured number of atoms and temperature from absorption imaging of the cloud after time-of-flight, as well as from the eigenfrequencies of the ODT, measured or calculated from a numerical simulation. Nearly all images, for a detuning of the PCI imaging light of -298 MHz or higher (in absolute values), corresponds to good results; for too high optical depth, it was necessary to use detunings higher than -642 MHz (in absolute values).

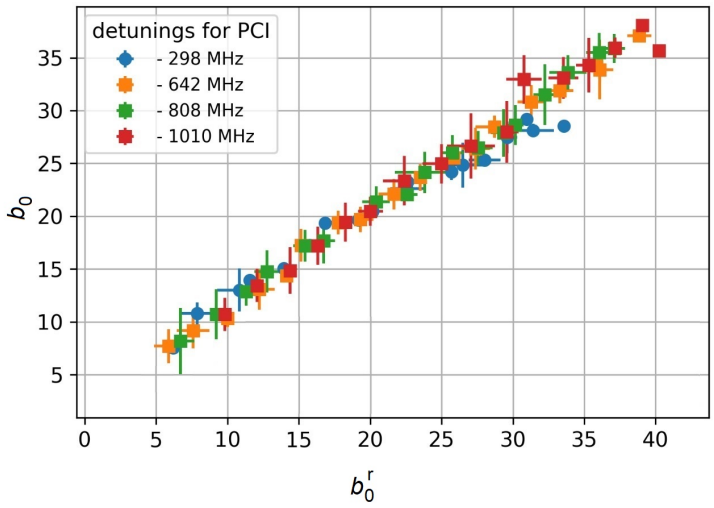

Figure 41 – Optical depth of the atomic cloud, measured *in-situ* with the PCI, as a function of the reconstructed optical depth from absorption imaging of the cloud after time-of-flight. Different detunings of the PCI imaging light were used, all giving same result (except for the higher optical depths imaged with the detuning of −298 MHz.)

By the end, we could obtain a cloud with OD going up to 50, a temperature of 1.2 µK and transverse sizes of 10.4 µm. The vertical is estimated through the measurement of the trap frequency to be 2 µ.

3.5.7 Characterizing the trapping frequencies

Close to the minimum of the trap, the ODT conservative potential can be approximated by a quadratic potential, in the form

$$U(x,y,z) = U_0 + \frac{m}{2}\left(\Omega_x^2 x^2 + \Omega_y^2 y^2 + \Omega_z^2 z^2\right) \ . \tag{3.8}$$

In this case, all we need to know are the three trapping frequencies Ω_x, Ω_y and Ω_z to relate the number of atoms and temperature of the cloud to its size, density and optical depth. Those frequencies can be measured by different techniques, such as applying a constant force to the atoms for a short time and then let them oscillate around the minimum of the trap, or modulate the trap potential to measure the parametric resonances of the atoms when the modulation has a frequency which is twice the trap frequency (Gillmann; Jäkel; Karger, 2014).

In our experiment, all attempts to measure the trapping frequencies of the horizontal (x and y) directions were not successful, or inconclusive. Those frequencies are then indirectly inferred from the measurement of the temperature of the cloud and the size of the cloud in x and y, to be around $\Omega_x \simeq \Omega_y \simeq 2\pi \times 170$ Hz. We could, nevertheless, measure the frequency in the z direction, which is $\Omega_z = 2\pi \times 570$ Hz. Those values correspond to

the situation with low power at the ODT beams, after the drop of power of the Mephisto laser.

3.6 Behind data taking

One of the major experimental challenges behind the process of acquiring data was to deal with the fluctuations of the experimental parameters. As mentioned before, during the course of this PhD the power of the ODT laser decreased by 40 %. Another main source of fluctuations was the temperature of the laboratory.

Our whole vacuum system has a size of roughly 1 m, on top of a optical table with 1.5m x 3 m, which amplifies the effect on atoms of the contraction and expansion of the metallic system. We built a system using Arduino and several thermocouples to collect in real time the temperature of several points in the room. For the thermocouple in contact with the vacuum system, we found a strong correlation of atoms number and air/metal temperature.

We continuously upgraded the system in order to uncouple internal and external variables, until we reached a point in which the only obvious update would be a more stable room temperature. We decided to continuous monitor and collect all cloud information for every measurement taken. Considering a repetition rate of 0.3 Hz and normally the data collection goes uninterruptedly for roughly a week, we are talking about acquiring, storing and analyzing hundreds of thousand of measurements, each one of them composed of different types of data, like:

- PMG - image of the cloud composed of three images;
- txt file - timestamps for 3 photodetectors;
- HDF5 file - labscript output file with experimental sequence, several photodetectors with power information

Each one of the dataset mentioned above was generated independently for different computers so it was important to ensure a proper synchronization of the data above. To ensure the correct connecting between the data mentioned above, we developed a redundant method of different flags that can be used to match the data.

4 RESULTS

Our main goal in this thesis is to measure the resonant light transmission of our atomic cloud, and to probe possible collective modifications of the transmission. On what follows, we describe all calibrations we have made, and the main experimental results of the thesis.

4.1 Probe beam characterizations

The cloud's transmission is probed using a laser beam with variable frequency around the resonance. As mentioned in the last chapter, the offset lock system of the Baby-blue with respect to the master Blue allows us to scan around 10 Γ around the atomic resonance. As important as the laser frequency, the size of the probe beam can also interfere on the scattering regime, once the cloud has a Gaussian distribution of atoms, a probe beam with a size comparable (or bigger) to the cloud will produce a higher amount of atoms in the single scattering regime, with a small beam probing only the central part of the cloud creates more multiple scattering light.

Ideally, we would like to have a beam with waist ω_0 much smaller than the cloud radius in the probe direction ρ, $\omega_0 \ll \rho$ condition. However, there are some experimental and physical limitations to this production. The cloud radius is around 20 λ (10 µm), which means we must produce a laser beam smaller than this. The physical limitation for the production of a very small beam is the diffraction limit, with the diameter of the spot size (d) as:

$$d = \frac{1.22\lambda}{NA}, \tag{4.1}$$

where NA is the numerical aperture of a lens. For lenses used in air, this typically has a top value of 0.95. The smaller spot size is ≈ 1.22 λ. Despite the diffraction limit, there are also other optical aberrations such as spherical aberrations capable of interfering with the spot size and shape. More on the side of a technical limitation, the Coherent transmission measurement requires light with low saturation s defined as:

$$s = \frac{I}{I_0} = \frac{2P}{\pi\omega_0^2}\frac{1}{I_0}, \tag{4.2}$$

where P is the beam power in mW, and I_0 is the saturation intensity (34 mW/cm^2 for blue transition). From the equation above we may conclude that a beam with very small waist also requires low power to continue in the limit of $s \ll 1$. We need to encounter a

trade-off between having a small beam to probe only the center (and more homogeneous) region of the cloud while continuing to the limit of a reasonable detection level.

4.1.1 Probe beam waist

During the experimental description, it was emphasized the versatility of the science chamber with larger windows proportioning good optical access to the cloud. However, the effective minimum distance from the atoms to the lens responsible for focusing the beam is around 75 mm. With this information, and considering the maximum lens diameter of 1/2 inches that we could install without blocking the path to other light beams, we established the minimum beam size at the focus as 3.4 μm. The focusing of the beam onto the atoms is made with a commercial achromatic doublet from Thorlabs (AC127-050-A-ML).

The next step is ensure the beam has this size, as this beam size can interfere with the expected results. For that, we have performed different characterizations outside the vacuum system. The first one was to measure directly the waist of the beam with a CCD camera. The CCD camera with the smallest pixel size in our laboratory has a pixel size of 3.45 μm, close to the beam waist itself; it is clear, then, that this measurement will have a larger uncertainty, nevertheless, we have performed the measurement, shown at the left of Figure 42. We have fitted this figure, considering that the intensity measured at each pixel is the integration of the light beam at the pixel size, and have found a waist of 3.4 μm.

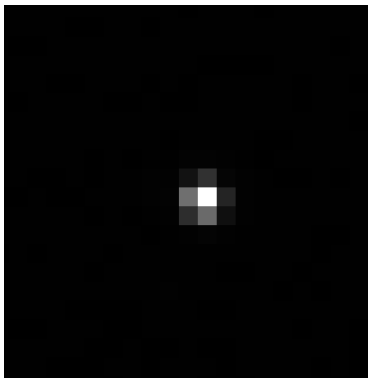

Figure 42 – Coherent transmission beam, directly measured by a CCD camera of pixel size 3.45μm.

We have also measured the beam size after a magnification telescope that made a calculated magnification of 4. In this condition, we have measured a waist of 15.2 μm, which gives a premagnified waist of 3.8 μm. It is known that the magnification can induce additional aberration in the beam, so we took this result as an upper value for the waist of the beam.

Finally, we have performed a third characterization, using a positive resolution target of model 1951 USAF from Thorlabs (part number R2L2S4P). The resolution

test target present a series of lines with different separation, and we have measured the minimum transmission of our light beam when aligned to each subgroup of lines, from the 7-1 to the 7-6 subgroup (corresponding to a inner separation between the black lines of the grating hanging from 3.9 to 2.2 μm). The line of scan of our beam on the grating is shown at the top of figure 43, and the experimental transmission are shown at the bottom, left of the same figure, as a function of the lower index of the subgroup.

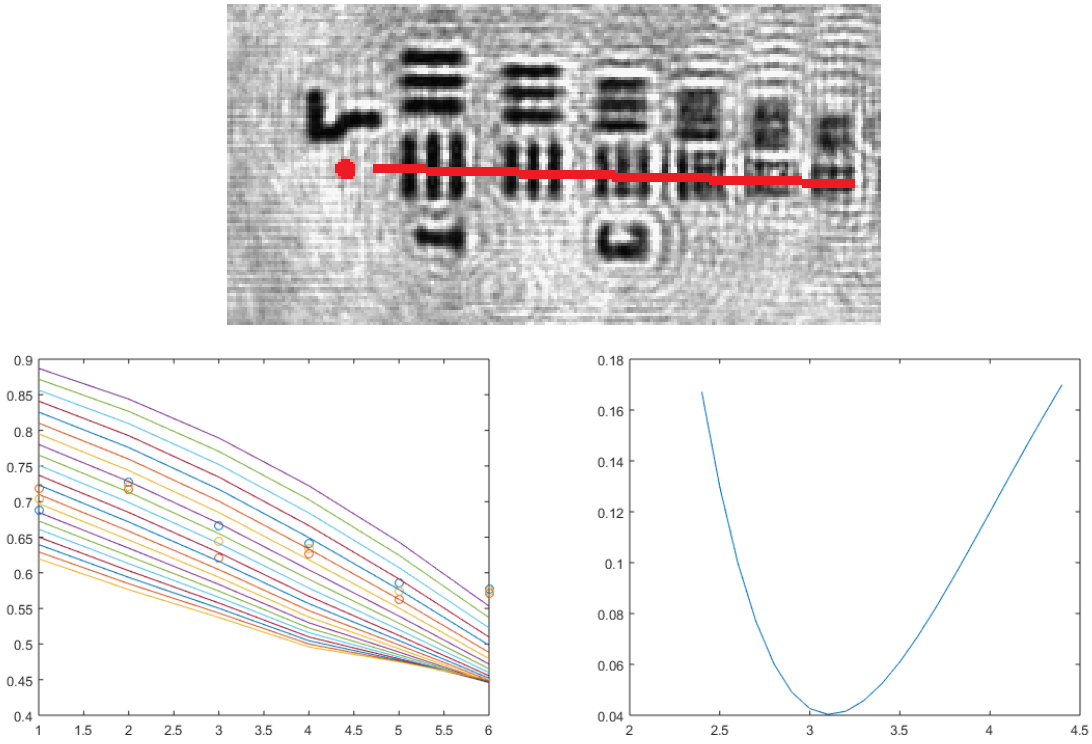

Figure 43 – Top: Zoom of the positive resolution target from Thorlabs (part number R2L2S4P), showing in red the path of the light beam for the characterization. Bottom, left: The circles represent the minimum transmission measured in each target subgroup of three vertical bars. The lines are the theoretical transmission for a beam of waist 2.4 μm (upper curve) to 4.4 μm (lower curve), separated by steps of 0.1 μm. Bottom, right: Normalized squared distance from the experimental points to the theoretical curves, as a function of the theoretical waist.

We have then computed the measured transmission at each grating to the theoretical expected value for a beam of theoretical waist ranging from 2.4 to 4.4 μm, considering a very simple model of total blocking of parts of the laser beam, with no regard to diffraction effects at the border of the grating (we have assumed that the diffraction is a small effect, only important at distances of the order of $\lambda = 461$ nm from the border); this is shown as the continuous lines at the same graphic, then we can compute the minimum squared distance from the experimental points to the theoretical curves, which is shown at the bottom right of figure 43 as a function of the waist of the theoretical curves. We deduce

from this analysis that our beam has a waist of (3.28 ± 0.42) µm.

Considering all measurements, we keep an average value of 3.4 µm as the measured waist of our beam. It is important to note here that, as far as the waist of the beam is much smaller than the radius of the cloud, we can consider that it probes an atomic density profile which is homogeneous in the transverse direction.

4.2 The measurement system

Despite its system versatility, for this thesis, the main measurement is the coherent transmission of the atomic cloud. The idea behind spatially coherent light scattering is to probe the transmission of a single mode of light using monomode fibers.

The probe light is brought from the lasers to the atoms using a monomode fiber to ensure a single spatial mode of light (see figure 44). Using the Thorlabs AC127-050-A-ML lens, the beam is focused into the atoms in a spot of 3.4 µm. The idea behind the focus is to ensure the light probes a roughly homogeneous part of atomic cloud. In comparison the radius of the atomic cloud in the transverse direction is 10.4 µm.

After interacting with the atoms the light is collected using another lens that colimates this beam to be later coupled into a fiber, to ensure the capture of a single spatial mode of light. Before coupling in the last fiber the light polarization is divided and directed to two different channels: parallel and orthogonal to incident polarization.

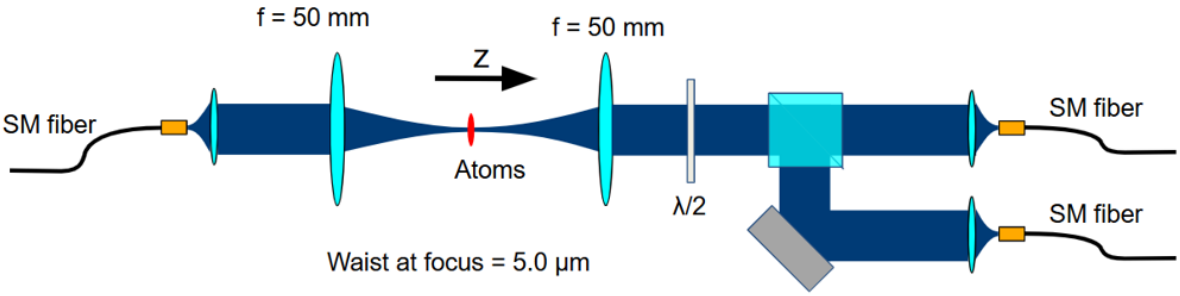

Figure 44 – Scheme of the probing of the system. An incident laser beam is focused on the atoms and the transmitted light is divided in both polarizations channels and sent to APDs using single-mode fibers.

These two polarization channels are important to differentiate between single and multi-scattered light. Since we are detecting light in the transmission, all single scattered photons must maintain the initial polarization, in this case linear, while only multi-scattering may producing light in the opposite polarization channel. This means once our measurement is also resolved in polarization, we ensure the two measurement are the orthogonal components of the single spatial mode of light.

The system described above is a simplification where the actual measurement system has more components: Initially after the fiber we have a film polarizer that ensures a a very good extinction ratio for the linear polarization of light. After this film we have a beam splitter which samples some amount of incident power for a continuous monitoring.

The detection of light is done using two avalanche photo-detector (APD) model ID100 from IDQ and a photomultiplier model PMA Hybrid from PicoQuant. The APDs worked based on the Geiger-mode, meaning a single photon can trigger an avalanche reaction leading to very strong current that can be measured. This devices are also known for their very low jitter, ensuring detection precision at picoseconds level.

The arrival time for the photons is recorded using a Time-to-Digital Converter model ID900 from IDQ. This time controller has 4 signal inputs for APDs as well as 4 outputs. It can be controlled using the internal blocks diagram, and the communication with a computer is done using Python.

4.2.1 ID100 calibration

Despite the advantage about the very good timing on these APDs, they present two drawbacks:

- Dark counts: There is a high probability that thermal fluctuations lead to fake counts, this counts are called dark counts;

- After-pulsing: These detectors normally have some probability of producing an extra pulse right after a first detector, this is called after-pulsing.

To characterize the dark-count, as well as compare it values with the manufacturer, we record arrival times during 5 minutes in a dark-room and with the APDs protected from any source of light. Since these is a Poisson process we may characterize the arrival time, which is the time difference between two consecutive detection events. The histogram of the arrival time should follow an exponential law (see figure 45):

We also see an over-counting of photons with very low waiting times, this counts represent the after-pulsing. To characterize it, we took measurement using laser light varying the intensity and consequentially the number of counts. If we plot the waiting time as a function of the arrival event, we see the clear segregation in two regimes (check the figure 46 representing the real counting and the after-pulsing.

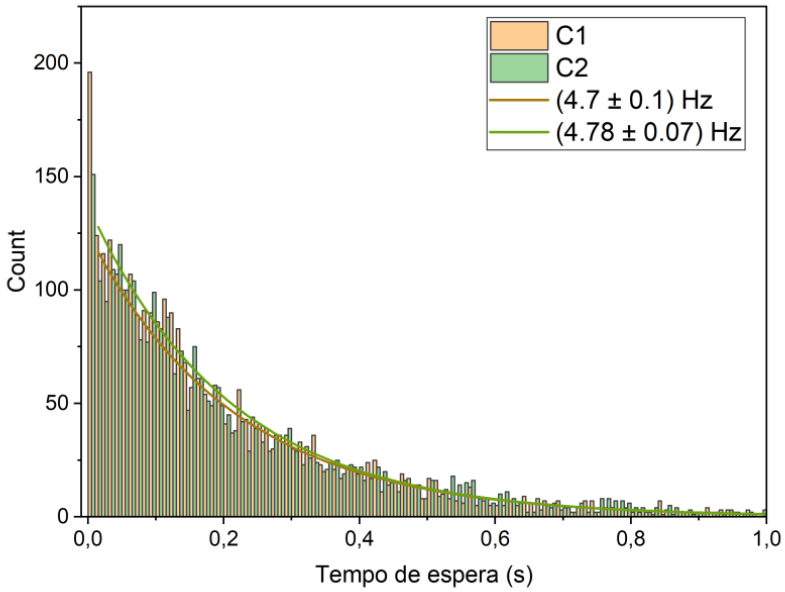

Figure 45 – Histogram of the delays between two consecutive dark counts. The fitting of a Poissonian distribution shows that the dark count events are mostly independent, as expected (but note the overrepresentation of short delays, to be explained in the next figure); the mean value of the time corresponds to a dark count rate of around 4.7 Hz in each channel.

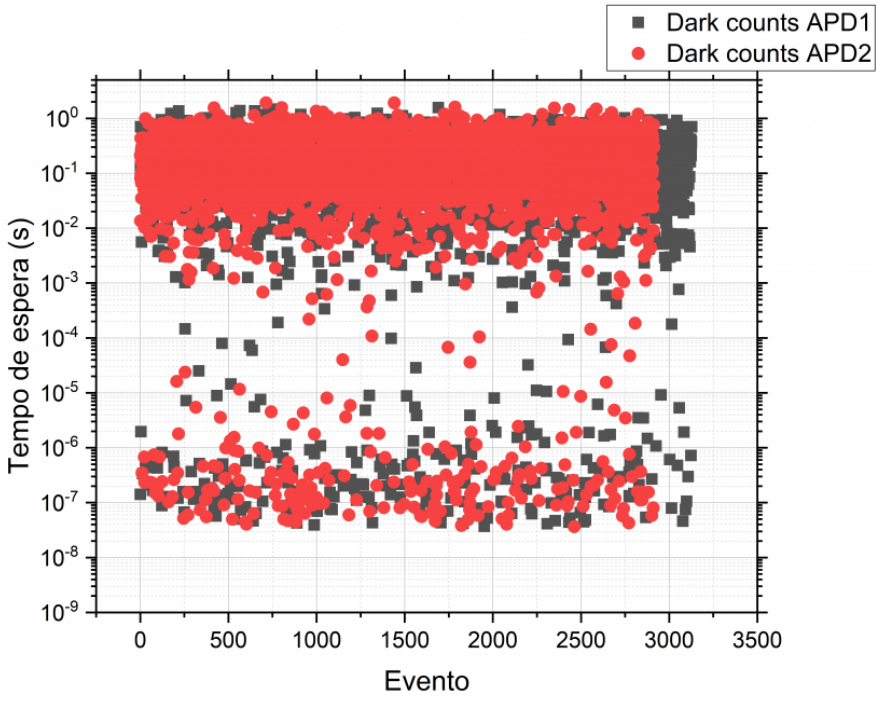

Figure 46 – The distribution of waiting times for each APD shows an unexpected presence of short delays (waiting time < 1 µs) not explained by a Poissonian probability distribution for independent events. It is the result of artificial double detections. We verified that it also happens for the real counts.

Comparing the evolution of extra counting as a function of detection frequency we see the linear evolution with a probability of 1.8% extracted from fitted curve in figure 47:

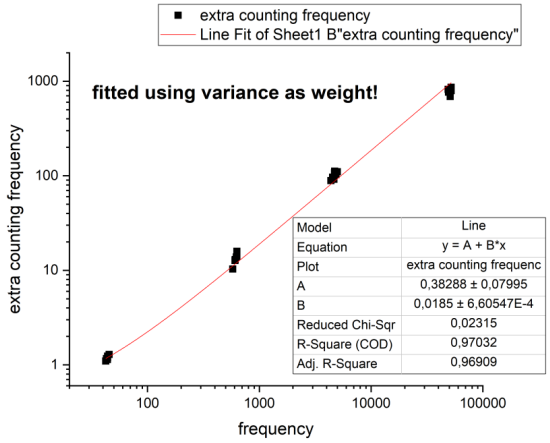

Figure 47 – Extra counting evolution with incident light increase.

4.2.2 Detection birefringence

A key point in our measurement is the possibility of differentiating between single and multiple scattering using light polarization. While the multiple scattering is expected to mix all polarization channels, the single scattering light will have its polarization equal to the projection of the incident one, in the forward direction. The incident polarization quality is ensured in two steps:

1. The optical fiber responsible for bringing the light from the optical table to the experiment is a polarization maintaining optical fiber. This means the fiber has a natural birefringence to ensure the incident light polarization if preserved. This fiber is stabilized matching the incident polarization and one of the optical fiber proper axes.

2. At the fiber output we installed a half-lambda waveplate and a polymeric polarizer. This polarization filter ensures a PER of around 10 000:1

After the science chamber and the overall detection system, we have more polarization elements, which may introduce another layer of birefringence, but more probably the more important ones are the multiple surfaces with anti-reflection coating and the multiple dielectric mirrors in the path. These surfaces use thin-film interference to maximize light transmission (typically 99% or higher). Except for a few metallic mirrors, in our experiment, all other mirrors used for directing laser light are dielectric mirrors. These optical elements, together with transmission elements, can mess up the polarization due to different phase jumps and differences in Fresnel coefficients.

It's common in these experiments to always make reflections using orthogonal angles (which may rotate but preserve the polarization quality), However, given the quality of the polarization needed for CLT measurement, we characterize all possible incident polarizations and the respective PER they generate after propagating through the transmission system. The general idea is: If the system presents birefringence there are at least two axes in which we'll experience the minimum amount of distortion in the polarization, otherwise we should see a constant PER as we rotate the incident polarization.[1]

The measurement was done by scanning the incident light polarization rotating the polarizer and maximizing the power using the half-lambda waveplate after the fiber. The very good PER of the polarizer ensures a constant quality for the incident polarization. Each polarization channel is split later with the use of a half-lambda waveplate and a polarizer beam-split cube (PBS cube). The PBS cube are known for having a very clear polarization on the transmission channel, while slightly mixing light from the transmission channel in the reflection one. That's why normally the PER is specified only for the transmission. Tor the detection this cube have a PER of at least 1000:1.

In our measurement, the multiple scattered lights represent a small fraction of the transmitted light. To maximize the capture and quality of multiple scattering light collected, we set the cube output as follows:

- Cube transmission: Orthogonal polarization channel;
- Cube reflection: Parallel polarization channel.

It's worth mentioning the opposite is also true, the light from multiple scattering may contaminate the light from single scattering, as it is composed of both polarization channels. However, in the low scattering limit this only represents a very small fraction, and as the single-scattering light decays exponentially, once the multiple scattering light starts to considerable contaminating it, the single-scattering light is already undetectable.

To conclude this section, the measurement of PER for different polarization angles is in the best case 800. This gave us a threshold at which we can only be sure the light detected from multiple scattering if counting passes 1/800 of the parallel polarization.

4.2.3 Spurious/Dark count

Beyond the description of APD dark counting, representing the minimum possible amount of detected counts, it's also important to characterize the dark count of the measurement system itself, to ensure our detected signal is not caused by some spurious

[1] We can choose the initial polarization since this measurement is done with null magnetic field. This means all three magnetic sub-levels of $^3P_1$ state are degenerated

light. To measure light in the picoWatt regime is not easy, as any source of light, like stand-by light from electronics, can make its way to the detection scheme. It's important to differentiate these spurious photons from the dark count mentioned before. The APD dark count is a side effect of using it in Geiger mode. This causes small terminal fluctuations to trigger a fake photons detection. The spurious light discussed here represents real photons arriving at the detector, but they are not the signal we are interested in. To minimize the occurrence of spurious light all measurements were done with room lights off, as well as unnecessary monitors and oscilloscopes also off.

The measurement of spurious light should reflect the real conditions of the experiment operation. During the measurements we collect, non-stop measurements for days in a row. At different moments of the day, we run the experiment in the same condition without the probe beam. Ideally, we would like to be able to detect also the photons scattered by the probe beam without the atoms. However, in forward detection, this is not possible.

Since the ODT represents a major source of photons as these beams have Watts of power, we also took measurements with the ODT beams off to investigate how much they contribute to spurious light. It's also worth mentioning the ODT wavelength is far from the detection window for the APD and we installed filters for the ODT wavelength before the collection fiber.

In the first measure we set the following probable sources of spurious light: Monitors, ODT and the shared room light:

What was on	**Spurious count (Hz)**
All monitors + ODT + shared room lights	38
All monitors + shared room light	106
Shared room light	94

Counterintuitively we observed an increase in spurious counting once we turned the ODT-off. This amount of light doesn't seem to come from any external source. In the next day, we repeated the experiments, but with the probe beam blocked:

What was on	**Spurious count (Hz)**
Only blue laser	3.5 (5.2)
blue + red lasers	3.5 (7)
blue + red + green lasers	7 (9)
blue + red + green + ODT lasers	4.7 (7)

From the result above we found the reason behind the high counting in the previous measurement was the leaking light from the probe AOM. To produce the short pulses for the measurement we use an AOM and change the power of the radio-frequency connecting the probe light. To allow the production of laser pulses as short as 100 ns we use a

radio-frequency switch from Brimrose, model TEM-85-10-461, where one of the entries is connected to a VCO and the other is grounded with the help of 50 Ω resistor. This shared output is connected to a RF amplifier.

Despite the very good isolation, the extinction ratio in this system is 35 dB, but since our detection scheme has a dynamical range of 1 mi (from Hz up to MHz) we end-up detecting this power. This also explains the increase in detected power once the ODT was turned off, this represents some portions of atoms that were absorbing these photons, stopping them from reaching the APD. To conclude we also have a mechanical shutter providing infinite extinction as it's composed of an aluminum plate, and was closed in the second set of measurements.

4.2.4 Probing time

Probing time corresponds to the useful time for taking measurements. During the measurement process we use resonant light to probe the light transmission varying the number of atoms, however, because of absorption and spontaneous emission, the resonant light promotes heating of the atomic cloud decreasing the spatial density changing the conditions from the beginning of measurement. In this case, for every measurement we have a convolution of different atomic densities during the measurement time. To decrease this possible source of error we characterize the maximum measurement time before larger changes in the cloud properties.

For characterization, using the same measurement setup but with only the parallel channel, we measured for a fixed laser beam intensity of 145 pW, corresponding to saturation parameter of $s = 0.02$. We continuous monitored the number of photons for a vary long measurement time, typically 500 µs. During the measurement, as the photons are absorbed and scattered, the momentum transferred to the atomic cloud, heats it, decreasing the spatial density and increasing light transmission. In this way probing the light transmission we can set an upper limit for the measurement time, before we heat the cloud beyond the desired optical density limit.

In figure 48 we see a strong increase in light transmission after 50 µs. For this reason we decided to establish 50 µs as the superior probing time.

Because our atomic specie has a very low scattering length in the ground state, it's not possible to probe the heating effect because the absence of thermalization, however, another effect of the probing beam related to the absorption of light is the decrease in atomic number.

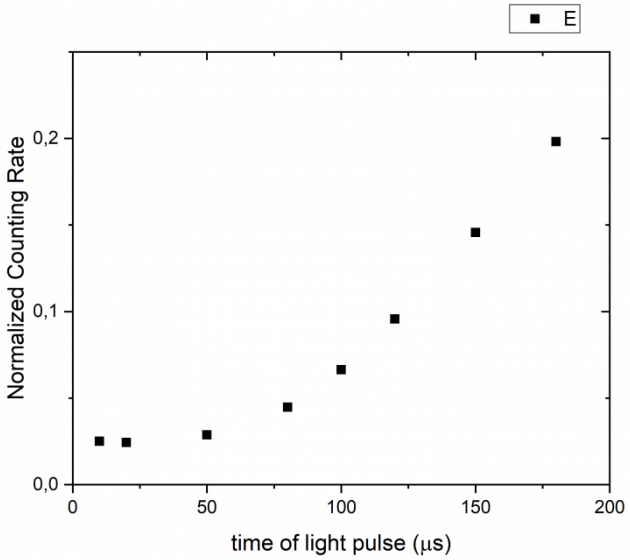

Figure 48 – Counting rate for the transmission detection versus duration of the light probe pulse.

For this measurement we fixed the probing time in 50 μs and scanned the number of atoms. With the beam intensity also fixed in 145 pW, the energy/momentum transferred to the atomic cloud is also constant. Since this measurements were done with the optical dipole trap (ODT) on, the fraction of atom's loss should decrease as the atomic numbers increase, however we probed a continue fraction of atoms' loss of roughly 14 % (check the image below), independent of the atomic number, probably representing light-assisted collision (Fuhrmanek *et al.*, 2012) to be investigated further.

4.3 Transmission in dense regime

The light transmission in the dense regime has as principal characteristic the suppression of the single atoms effect with the emergence of collective effect together with the multiple scattering regime.

The single atomic scattering is well understood since the scattered light in proportional to the excited population, and the excitation regimes can be easily calculated from the average values of electric field operator, or even considering the coupling of a single atoms with the vacuum modes (Cohen-Tannoudji; Dupont-Roc; Grynberg, 1998).

As described in chapter 2, this problem of light scattering is normally treated dividing the scattered light in two components: The mean scattering field and the fluctuations from the mean value. The interesting result from the approach is the directly derivation of the light scattered light spectrum, where the mean value results in a spectrum equal to the exiting field. As the driven forces increases the fluctuations become stronger and the spectrum is well characterized by the Mollow triplets.

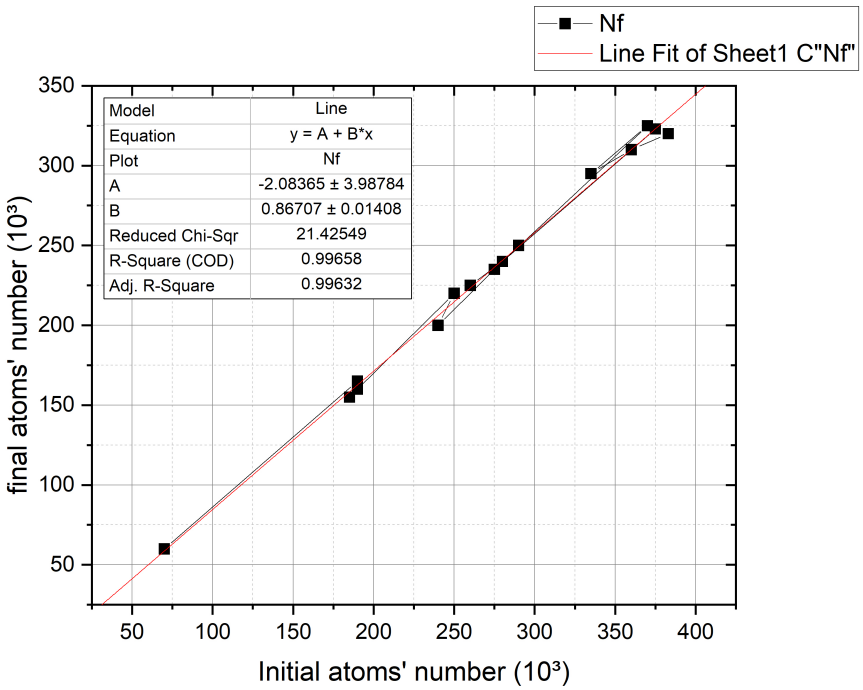

Figure 49 – Atomic number evolution before and after we applied the probe beam.

If instead of light scattering we consider the light transmission of a laser beam through the atomic cloud, the simple case is to treat each atoms as a homogeneous disk with radius given by the scattering cross section (b_0) which constantly remove light from the incident laser beam. This results in the so called Beer-Lambert law as discussed in the theory chapter. The photons removed from the initial incident beam are normally seem as "lost", however in the case of multiple scattering clouds and considering the so called Independent-Scattering-Approximation (ISA) the transmission of light by the cloud have another component known as Ohm's law (Wiersma *et al.*, 1997), in analogy with the Drude's model from electronic transmission in a disordered metal (Jackson, 2021).

The underlining of the two possible approaches briefly mentioned is the difference on considering the light-scattering, or even light-interaction problem from the atomic point of view or from the photonic point of view. Both approaches lead two different paths of interpretation the limit of atomic scattering: From the atomic point-of-view as more atoms are involved in the process of light scattering and as the become closer to each other, the photon exchange between neighbor atoms results in an effective interaction between them resulting in the Couple-Dipole model described in chapter 2. The key consideration of this approach is the interaction of atoms with the electromagnetic field become collective, through the Collective modes. Several experiments show the validate of this model for low atomic excitation and low spatial density.

From the atomic point of view, beyond the ISA we enter in a regime where the scattering probability is not homogeneous anymore as the spatial density increases, these

effects were observed in other experiments from macroscopic particles and resulting in a modification of the Ohm's law. Another intrinsic manifestation of these multiple interaction effect are explained using a mesoscopic approach on the scattering of light (Akkermans; Montambaux, 2007).

The central results to be discussed in the following seek to explore the limit discussed above on both approaches, this results in two main results covering two of the many possible attacks fronts:

- Transmission resolved in polarization: For this measurement we use a low intensity atomic beam with s = 0.02 and probed the cloud transmission in two polarization channels - one parallel and one perpendicular do the incident polarization. Scanning the atomic number/spatial density we start in a predominant single to multiple scattering regime.

- Transmission for different saturation parameters: For this measurement we keep only the parallel transmission channel however we scan the laser beam intensity beyond the linear regime.

4.3.1 Transmission resolved in polarization

Using the system and the characterizations described before we probed the transmission of the atomic cloud solving in the two different polarization channels. In total this measurement correspond to over 20000 realizations of the experiment where we collect the light transmission and the number of atoms for every single realization.

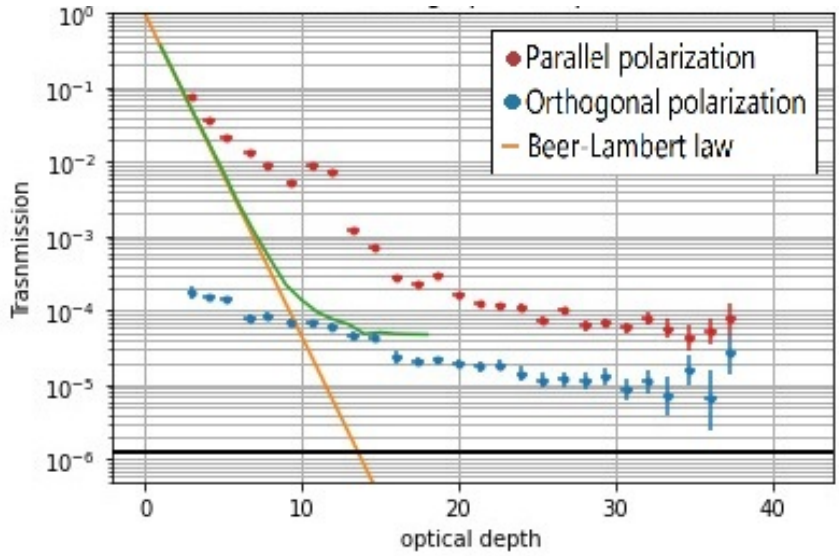

Figure 50 – Transmission resolved in polarization for various optical densities. In orange we have the Beer-Lambert law, while in green we have theoretical simulations of coupled dipole model.

Because of the small size of our atomic cloud we cannot probe very low optical densities, meaning for the first measurement point we are already enter in the multiple scattering regime. From the red points in the figure 50 we see a concordance with Beer-Lambert law that very fast deviates from the expected behavior.

Given for an OD of 10 our spatial density is around 1.8 $\rho\lambda^3$, while is expected for the densities effect to be strong at 1-10 $\rho\lambda^3$, the slower decrease of the transmission is already evidence of the possible manifestation of densities effects, however our simulations for the CDD couldn't capture this behavior.

In blue we have the measurement responsible for the orthogonal channel. The multiple scattering transmission, in the ISA, corresponds to the Ohm's law representing a slower decay with the optical depth normally characterized by $C \times 1/b_0$ curve. The constant C is a geometrical factor depending on several physical parameters of the sample.

Both curves present a very strong reduction and saturation in the transmission after an optical depth of 25. Because of the absence of a theory to simulate this behavior its hard to point out the exactly causes of this saturation, but some key results on other experiments can help us to point a direction towards this effect.

The limitation towards the CDD where seen in another Coherent transmission experiment (Jennewein *et al.*, 2018). In this experiment few consideration where pointed out as the source of mismatch between theory and experiment: the complex magnetic structure of Rubidium could introduce different transition, like non-radiative ones, between atoms resulting in changes on the expected transmission. The CD model was also modified to include a better description of the electromagnetic-field, as well as, better description of its evolution.

A renormalization approach done by (Andreoli *et al.*, 2021) could be the source of the saturation effects seem on the index of refraction of several materials, although in this experiment we are below the expect limit where this saturation could occur, this shows how strong interaction among atoms can complete modify their response towards EM fields.

To conclude a very similar experiment to this one [cite paper of transmission for spherical beads], probed the changes in the ISA approach caused by the near-field effects, creating extra transmission channels resulting in a effective higher mean-free-path.

4.3.2 Transmission for different saturation parameters

Back to the discussion regarding the CDD, the collective modes present different coupling with a electromagnetic fields when compared to the single atom case. This effective coupling could be higher, if we are talking about the *supperradiant* modes or smaller if we are talking about the *subradiant* modes. The intersting part of this is the considerations

towards being or not in the "linear" regime can also depends on the manifestation of these modes.

The linear regime, where the CDM is valid, represent a very low excitation level, meaning no-atoms in the cloud is saturated and their response is linear with the driven field applied. As expansion of the CDD beyond the linear regime is difficult and topic of actual research. So altogh we use an small intensity of light to driven our atomic cloud, its possible even for this very low light we could already experience effect of saturation on the atoms, caused mainly by the *subradiant* modes, since they low-coupling to the laser light also represent a very small saturation intensity.

But is important to keep in mind other experimental limitations were also involved on the choice for the probe intensity. As mentioned during the probe beam characterizations, the smaller intensity the better to ensure we are in the linear regime, however we have some technical limitations towards the minimum intensity we can measure and also the dynamical range of the measurement system as a whole.

For this measurement we used only the parallel transmission channel as this one have higher transmission. We observe is a dependence of the light transmission as a function of the saturation parameters, however the overall shape of the curve remains the same and with transmission higher tran both Beer-Lambert Law and CDM simulations.

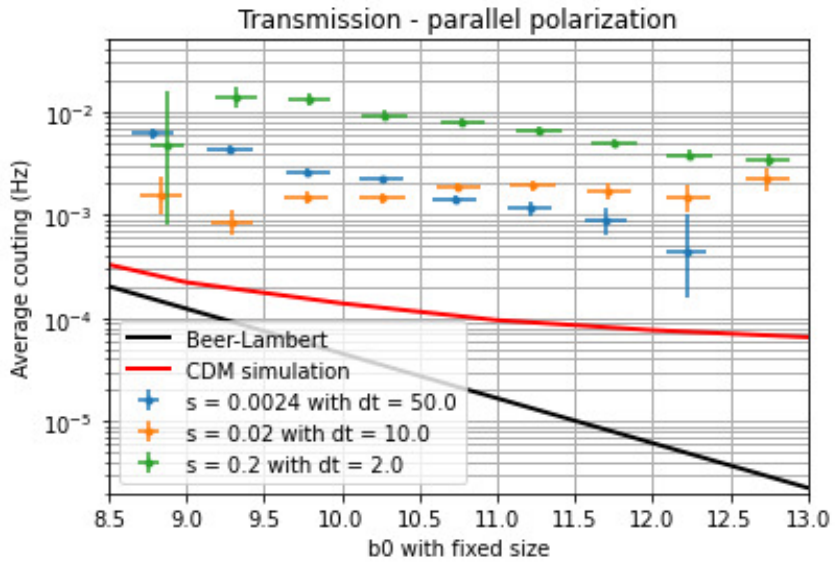

Figure 51 – Cloud transmission for different beam intensities

Despite the error bar the proximity of the transmission curves for s = 0.0024 and s = 0.02 makes us consider the previous measurement results are correct about the overall behavior of the transmission, although some offset could be caused the saturation effects.

5 CONCLUSION

This thesis focused on collecting experimental evidences on changes in light scattering in the dense regime. Considerable amount of time was dedicated to obtaining the desired sample with enough optical depth/spatial density. The main achievements on the experimental part are: The us/e of molasses together with ODT for further cooling after transfer atoms, the imaging system allowing the measurement of very dense optical samples, the improvement on experiment repetition rate and the overall measurement system together with the data analyses allowing for a continuous operation even in the presence of strong fluctuations.

In the dense regime, we observed a transition from single-atom effects to collective effects and multiple scattering, however with strong discordance from theoretical simulations. The transmission measurements ,resolved in polarization, showed, for parallel transmission deviations from the Beer-Lambert law at intermediate optical depths, and a saturation of transmission for higher optical depths, indicating the possible presence of density effects. The orthogonal channel measurements showed the initial decay expected for Ohm's law, but the same saturation in higher optical depths. These findings underscore the complexity of light transmission in dense atomic clouds and the need to consider both individual and collective atomic behaviors, although an appropriate theoretical description is still missing.

We also explored the transmission for different saturation parameters, finding that the overall shape of the transmission curve remained consistent, with higher transmission than predicted by both the Beer-Lambert law and coupled dipole model (CDM) simulations. This suggests that even at low light intensities, saturation effects may be present due to the manifestation of subradiant modes. These results highlight the interplay between light scattering in dense atomic clouds and the importance of considering various factors, such as saturation and collective modes, in understanding light transmission.

Overall, our study provides valuable insights into the behavior of light transmission in dense atomic clouds and highlights the importance of considering both atomic and photonic perspectives in understanding light scattering and transmission phenomena.

REFERENCES

AKKERMANS, E.; MONTAMBAUX, G. **Mesoscopic physics of electrons and photons**. [*S.l.: s.n.*]: Cambridge university press, 2007.

ANDERSSON-ENGELS, S. *et al.* In vivo fluorescence imaging for tissue diagnostics. **Physics in Medicine & Biology**, IOP Publishing, v. 42, n. 5, p. 815, 1997.

ANDREOLI, F. *et al.* Maximum refractive index of an atomic medium. **Physical Review X**, APS, v. 11, n. 1, p. 011026, 2021.

ARAÚJO, M. O. *et al.* Superradiance in a large and dilute cloud of cold atoms in the linear-optics regime. **Physical review letters**, APS, v. 117, n. 7, p. 073002, 2016.

ASANO, M.; KUBO, K. Vapor pressure of strontium below 660 k. **Journal of Nuclear Science and Technology**, Atomic Energy Society of Japan, v. 15, n. 10, p. 765–767, 1978.

BALL, P. Precise atomic clock may redefine time. **Nature**, v. 4, 2013.

BARTHELEMY, P.; BERTOLOTTI, J.; WIERSMA, D. S. A lévy flight for light. **Nature**, Nature Publishing Group UK London, v. 453, n. 7194, p. 495–498, 2008.

BLACK, E. D. An introduction to pound–drever–hall laser frequency stabilization. **American journal of physics**, American Association of Physics Teachers, v. 69, n. 1, p. 79–87, 2001.

CHABÉ, J. *et al.* Coherent and incoherent multiple scattering. **Physical Review A**, APS, v. 89, n. 4, p. 043833, 2014.

CHALONY, M. *et al.* Doppler cooling to the quantum limit. **Physical Review Letters**, American Physical Society, v. 107, n. 24, p. 243002, 2011. Disponível em: https://journals.aps.org/prl/abstract/10.1103/PhysRevLett.107.243002.

CIPRIS, A. *et al.* Van der waals dephasing for dicke subradiance in cold atomic clouds. **Physical Review A**, APS, v. 103, n. 3, p. 033714, 2021.

CIPRIS, A. *et al.* Subradiance with saturated atoms: population enhancement of the long-lived states. **Physical Review Letters**, APS, v. 126, n. 10, p. 103604, 2021.

COHEN-TANNOUDJI, C.; DUPONT-ROC, J.; GRYNBERG, G. **Atom-photon interactions: basic processes and applications**. [*S.l.: s.n.*]: John Wiley & Sons, 1998.

COURTEILLE, P. W. *et al.* Modification of radiation pressure due to cooperative scattering of light. **The European Physical Journal D**, Springer, v. 58, p. 69–73, 2010.

DIAS, P. G. S. Coerência espectral da luz espalhada por átomos frios saturados. Universidade Federal de São Carlos, 2020.

DIAS, P. G. S. *et al.* Characterization of the collimation of an atomic beam with a monochromatic quasi-resonant laser. **Brazilian Journal of Physics**, Springer, v. 51, p. 329–338, 2021. Disponível em: https://link.springer.com/article/10.1007/s13538-020-00837-9.

DONLEY, E. A. *et al.* Double-pass acousto-optic modulator system. **Review of Scientific Instruments**, AIP Publishing, v. 76, n. 6, 2005.

FERNANDEZ, M. F. *et al.* Phase-contrast imaging of a dense atomic cloud. **arXiv preprint arXiv:2501.03158**, 2025. Disponível em: https://arxiv.org/abs/2501.03158.

FIORETTI, A. *et al.* Observation of radiation trapping in a dense cs magneto-optical trap. **Optics communications**, Elsevier, v. 149, n. 4-6, p. 415–422, 1998.

FUHRMANEK, A. *et al.* Light-assisted collisions between a few cold atoms in a microscopic dipole trap. **Physical Review A—Atomic, Molecular, and Optical Physics**, APS, v. 85, n. 6, p. 062708, 2012.

GANDJBAKHCHE, A. H.; WEISS, G. H. V: Random walk and diffusion-like models of photon migration in turbid media. **Progress in optics**, Elsevier, v. 34, p. 333–402, 1995.

GARCIA, T. *et al.* Control and automation of an ultracold atoms apparatus via the labscript suite. **Bulletin of the American Physical Society**, APS, v. 64, 2019.

GILLMANN, C.; JäKEL, O.; KARGER, C. P. Dose response curves for late temporal lobe reactions in patients after carbon ion irradiation based on two versions of the local effect model (lem). **Physics Letters A**, Elsevier, v. 378, n. 47, p. 3406–3410, 2014. Disponível em: https://www.sciencedirect.com/science/article/abs/pii/S0375960114012055.

GROSS, M.; HAROCHE, S. Superradiance: An essay on the theory of collective spontaneous emission. **Physics reports**, Elsevier, v. 93, n. 5, p. 301–396, 1982.

GRYNBERG, G.; ASPECT, A.; FABRE, C. **Introduction to quantum optics: from the semi-classical approach to quantized light**. [*S.l.: s.n.*]: Cambridge university press, 2010.

GUERIN, W.; ARAÚJO, M. O.; KAISER, R. Subradiance in a large cloud of cold atoms. **Physical review letters**, APS, v. 116, n. 8, p. 083601, 2016.

GÜNTER, K. J. Design and implementation of a zeeman slower for 87rb. **Report, Ecole Normale Supérieure, Paris**, 2004.

HOLSTEIN, T. Imprisonment of resonance radiation in gases. **Physical Review**, APS, v. 72, n. 12, p. 1212, 1947.

JACKSON, J. D. **Classical electrodynamics**. [*S.l.: s.n.*]: John Wiley & Sons, 2021.

JAVANAINEN, J. *et al.* Exact electrodynamics versus standard optics for a slab of cold dense gas. **Physical Review A**, APS, v. 96, n. 3, p. 033835, 2017.

JENKINS, S. *et al.* Collective resonance fluorescence in small and dense atom clouds: Comparison between theory and experiment. **Physical Review A**, APS, v. 94, n. 2, p. 023842, 2016.

JENNEWEIN, S. *et al.* Coherent scattering of near-resonant light by a dense, microscopic cloud of cold two-level atoms: Experiment versus theory. **Physical Review A**, APS, v. 97, n. 5, p. 053816, 2018.

KOGELNIK, H.; LI, T. Laser beams and resonators. **Applied optics**, Optica Publishing Group, v. 5, n. 10, p. 1550–1567, 1966.

KOLOKOLOVA, L.; KIMURA, H. Effects of electromagnetic interaction in the polarization of light scattered by cometary and other types of cosmic dust. **Astronomy & Astrophysics**, EDP Sciences, v. 513, p. A40, 2010.

KRSTAJIĆ, M. *et al.* Characterization of three-body loss in er 166 and optimized production of large bose-einstein condensates. **Physical Review A**, APS, v. 108, n. 6, p. 063301, 2023.

LABEYRIE, G. *et al.* Coherent backscattering of light by cold atoms. **Physical Review Letters**, APS, v. 83, n. 25, p. 5266, 1999.

LACHAUD, L. *et al.* Slowing down a coherent superposition of circular rydberg states of strontium. **Physical Review Letters**, APS, v. 133, n. 12, p. 123202, 2024.

LEHMBERG, R. Radiation from an n-atom system. i. general formalism. **Physical Review A**, APS, v. 2, n. 3, p. 883, 1970.

LIANG, Q. *et al.* Improvements on type-ii zeeman slowing of molecules through polarization selectivity. **Physical Review A**, APS, v. 100, n. 5, p. 053402, 2019.

LIAO, G.-B. *et al.* Optimization of a crossed optical dipole trap for loading and confining laser-cooled atoms. **Journal of the Optical Society of America B**, Optica Publishing Group, v. 34, n. 4, p. 869–876, 2017. Disponível em: https://opg.optica.org/josab/abstract.cfm?URI=josab-34-4-869.

LOFTUS, T. H. *et al.* Narrow line cooling and momentum-space crystals. **Physical Review A**, American Physical Society, v. 70, n. 6, p. 063413, 2004. Disponível em: https://doi.org/10.1103/PhysRevA.70.063413.

MAHMOODIAN, S. *et al.* Strongly correlated photon transport in waveguide quantum electrodynamics with weakly coupled emitters. **Physical review letters**, APS, v. 121, n. 14, p. 143601, 2018.

MANASSAH, J. T. Cooperative radiation from atoms in different geometries: decay rate and frequency shift. **Advances in Optics and Photonics**, Optical Society of America, v. 4, n. 2, p. 108–156, 2012.

MARIA, G. D.; PIACENTE, V. Vapor pressures of calcium and strontium by transpiration method. **The Journal of Chemical Thermodynamics**, Elsevier, v. 6, n. 1, p. 1–7, 1974.

MEPPELINK, R. *et al.* Thermodynamics of bose-einstein-condensed clouds using phase-contrast imaging. **Physical Review A**, American Physical Society, v. 81, n. 5, p. 053632, 2010. Disponível em: https://journals.aps.org/pra/abstract/10.1103/PhysRevA.81.053632.

MERCADIER, N. *et al.* Lévy flights of photons in hot atomic vapours. **Nature physics**, Nature Publishing Group UK London, v. 5, n. 8, p. 602–605, 2009.

MOLLOW, B. Power spectrum of light scattered by two-level systems. **Physical Review**, APS, v. 188, n. 5, 1969.

MUNI, A. *et al.* Optical coherent manipulation of alkaline-earth circular rydberg states. **Nature Physics**, Nature Publishing Group UK London, v. 18, n. 5, p. 502–505, 2022.

OHLSSON, T.; ZHOU, S. Density-matrix formalism for pt-symmetric non-hermitian hamiltonians with the lindblad equation. **Physical Review A**, APS, v. 103, n. 2, p. 022218, 2021.

OLIVEIRA, R. A. de *et al.* Single-photon superradiance in cold atoms. **Physical Review A**, APS, v. 90, n. 2, p. 023848, 2014.

PAVOLINI, D. *et al.* Experimental evidence for subradiance. **Physical review letters**, APS, v. 54, n. 17, p. 1917, 1985.

RAAB, E. L. *et al.* Trapping of neutral sodium atoms with radiation pressure. **Physical review letters**, APS, v. 59, n. 23, p. 2631, 1987.

RAVEN, W. Saturated absorption spectroscopy. *In*: **Atomic Physics for Everyone: An Introduction to Atomic Physics, Quantum Mechanics, and Precision Spectroscopy with No College-Level Prerequisites**. [*S.l.: s.n.*]: Springer, 2024. p. 85–109.

ROSSUM, M. v. van; NIEUWENHUIZEN, T. M. Multiple scattering of classical waves: microscopy, mesoscopy, and diffusion. **Reviews of Modern Physics**, APS, v. 71, n. 1, p. 313, 1999.

SCULLY, M. O. Collective lamb shift in single photon dicke superradiance. **Physical review letters**, APS, v. 102, n. 14, p. 143601, 2009.

SEGEV, M.; SILBERBERG, Y.; CHRISTODOULIDES, D. N. Anderson localization of light. **Nature Photonics**, Nature Publishing Group UK London, v. 7, n. 3, p. 197–204, 2013.

SHIGA, N. *et al.* Buffer-gas-induced collision shift for the sr 88 s 1 0-p 3 1 clock transition. **Physical Review A—Atomic, Molecular, and Optical Physics**, APS, v. 80, n. 3, p. 030501, 2009.

SKIPETROV, S. E.; SOKOLOV, I. Ioffe-regel criterion for anderson localization in the model of resonant point scatterers. **Physical Review B**, APS, v. 98, n. 6, p. 064207, 2018.

SKIPETROV, S. E.; SOKOLOV, I. Search for anderson localization of light by cold atoms in a static electric field. **Physical Review B**, APS, v. 99, n. 13, p. 134201, 2019.

SKIPETROV, S. E.; SOKOLOV, I. M. Absence of anderson localization of light in a random ensemble of point scatterers. **Physical review letters**, APS, v. 112, n. 2, p. 023905, 2014.

STELLMER, S.; GRIMM, R.; SCHRECK, F. Production of quantum-degenerate strontium gases. **Physical Review A—Atomic, Molecular, and Optical Physics**, APS, v. 87, n. 1, p. 013611, 2013.

STOVER, H.; STEIER, W. Locking of laser oscillators by light injection. **applied physics letters**, AIP Publishing, v. 8, n. 4, p. 91–93, 1966.

TOPTICA-PHOTONICS. **TA-SHG pro**. https://www.toptica.com/products/tunable-diode-lasers/frequency-converted-lasers/ta-shg-pro. Accessed: 2025-02-04.

WEEL, M.; KUMARAKRISHNAN, A. Laser-frequency stabilization using a lock-in amplifier. **Canadian journal of physics**, NRC Research Press Ottawa, Canada, v. 80, n. 12, p. 1449–1458, 2002.

WEISS, P. *et al.* Subradiance and radiation trapping in cold atoms. **New Journal of Physics**, IOP Publishing, v. 20, n. 6, p. 063024, 2018.

WIERSMA, D. S. *et al.* Localization of light in a disordered medium. **Nature**, Nature Publishing Group UK London, v. 390, n. 6661, p. 671–673, 1997.

WOLF, P.-E.; MARET, G. Weak localization and coherent backscattering of photons in disordered media. **Physical review letters**, APS, v. 55, n. 24, p. 2696, 1985.

WU, F.; GROVE, R.; EZEKIEL, S. Investigation of the spectrum of resonance fluorescence induced by a monochromatic field. **Physical Review Letters**, APS, v. 35, n. 21, p. 1426, 1975.